Durham E-Theses

Preparation and Coherent Control of a Rydberg Qutrit in an Ultra-Cold Atomic Ensemble

HUGHES, OLIVER,DAVID,WRONSKI

How to cite:

HUGHES, OLIVER,DAVID,WRONSKI (2025) *Preparation and Coherent Control of a Rydberg Qutrit in an Ultra-Cold Atomic Ensemble*, Durham theses, Durham University. Available at Durham E-Theses Online: http://etheses.dur.ac.uk/16338/

Use policy

This work is licensed under a Creative Commons Attribution 3.0 (CC BY)

Academic Support Office, The Palatine Centre, Durham University, Stockton Road, Durham, DH1 3LE
e-mail: e-theses.admin@durham.ac.uk Tel: +44 0191 334 6107
http://etheses.dur.ac.uk

Preparation and Coherent Control of a Rydberg Qutrit in an Ultra-Cold Atomic Ensemble

Oliver David Wronski Hughes

A thesis presented for the degree of

Doctor of Philosophy

Quantum Light and Matter

The University of Durham

United Kingdom

12th November 2025

Preparation and Coherent Control of a Rydberg Qutrit in an Ultra-Cold Atomic Ensemble

Oliver David Wronski Hughes

Abstract

This thesis presents the preparation, coherent control and interferometric readout of a single qutrit encoded in a cold Rydberg ensemble. A single photon is stored as a collective Rydberg excitation and subsequently manipulated by applying microwave fields coupling different Rydberg levels, before being retrieved after a programmable delay. A time-resolved sequential readout protocol is developed to determine the qutrit state populations. Coherence of the qutrit is investigated using a Ramsey interferometer implemented between Rydberg states, with the resulting fringe pattern demonstrating phase control and multilevel coherence.

Following a vacuum failure, the system was fully dismantled, cleaned and reassembled with a new 2D MOT cell. A programme of optimisation and characterisation was carried out using time-of-flight thermometry, spatially resolved absorption imaging and temperature based magnetic field compensation. Sub-Doppler cooling yields a minimum ensemble temperature of $T = 12.8 \pm 0.5$ μK, and the highest measured optical depth is $\mathrm{OD} = 4.3 \pm 0.1$.

This work establishes a robust and flexible platform for investigating high-dimensional quantum information protocols using collective Rydberg states and demonstrates the feasibility of fast, coherent control of single qutrits encoded in an atomic ensemble.

Supervisors: C. Stuart Adams and Kevin J. Weatherill

To my family, present and future.

"Let us run with perseverance the race marked out for us,
fixing our eyes on Jesus, the author and perfecter of faith."
— Hebrews 12:1–2

Acknowledgements

This project has seen its share of difficulties, from vacuum breaks to global events that made lab access something of a luxury. The writing also took longer than intended and I remain deeply grateful to those who helped me see it through.

First, I would like to thank my supervisory team, Stuart Adams and Kevin Weatherill. Stuart's depth of knowledge and passion for the subject were a constant source of inspiration. I'm especially grateful for the opportunity to join the project and for the balance of guidance and independence he offered. In particular after the vacuum break, when his trust allowed us to persist with the path we believed was best. Kev's practical help in the lab and broader perspective on what a PhD can be, beyond it's immediate goals, were equally valuable. His advice was always grounded and generously given. Thanks are also due to Robert Potvliege and Simon Cornish, whose thoughtful feedback during annual reviews helped set a high standard for the written work that followed.

I owe a lot to those with whom I shared the lab. Teodora Ilieva and Nick Spong were welcoming and patient in the early days, showing me around and passing on a wealth of practical knowledge. Yuechun Jiao was a steady and dedicated collaborator during the long stretch of alternating lab days (under conditions best described as "historically specific"). That period would have been very different without his patience over video calls and technical insight. Both Nick and Yuechun generously continued to answer questions even after moving on from Durham.

Later on, it was a pleasure to work with Lucy Downes, whose encouragement was much appreciated during my final months in the lab. Karen Wadenpfuhl, first as a Master's student and later as a PhD student, brought energy and purpose to the project. Although our time working together was brief, collaborating with Aaron Reinhard on his sabbatical year was a breath of fresh air that helped to renew motivation to finish writing.

And to my closest collaborator, Max Festenstein: working together was a genuine pleasure, even through setbacks, rebuilds and speculative schemes. From the practical to the gloriously implausible, Max's ideas were always brilliant. Between us, we could probably fill another thesis with experimental side quests involving

carjacks, oscilloscopes and a Rasberry Pi. Its conclusions might be questionable, but its appendices would be wildly entertaining.

The camaraderie of QLM, in the labs, over lunch, or in the pub, made life in the department a real pleasure. Thanks also to the support staff who kept things running behind the scenes, from the staff in the mechanical and electronics workshops, to those working in the Bransden room. I'm also grateful to everyone who read over drafts, or offered to. It meant a great deal that so many were willing to give up their time to help.

Beyond the department, I was lucky to find a good humoured and supportive circle of friends in Durham. The company of St Nic's Church and bell ringing communities offered a welcome distraction and helped keep things in perspective when work wasn't going to plan. Like much of Durham life, these communities were shaped by people coming and going and I am grateful for the time we shared. Thanks also to friends in the south of England, whose support reached all this way north.

A few earlier influences deserve mention. Matt Himsworth, who supervised my Master's project at Southampton, offered a formative introduction to research. Robin Hughes, an inspiring school physics teacher, helped nurture my curiosity. And although our meetings were infrequent, my great uncle Chris Wronski gave, in every meeting, a nudge in this direction.

I owe the greatest thanks to my parents, whose love and support have been constant. There is far too much to be thankful for, but I would not be at this point without them. I'm especially grateful for the calm, generous environment they provided while I was writing in London; a time more productive (and better fed) than I could have hoped for. Thanks also to my sister Kasia, whose optimism and encouragement never seemed to waver. I'd also like to thank my grandparents for their enduring love. I think especially of Dziadzio, who has long been an academic inspiration and, I suspect, understood more about what I was researching than he let on, despite claiming it was beyond him.

Finally, to Meg. Although she joined only for the long final chapter, her love, patience and perspective meant a great deal (rivalled only by her "kind, pretty and of course personable" nature). In saying it was perfectly fine not to finish, she somehow gave me the space I needed to do exactly that.

Contents

Declaration

The work in this thesis is based on research carried out at Quantum Light and Matter, Department of Physics, University of Durham, England. No part of this thesis has been submitted elsewhere for any other degree or qualification, and it is the sole work of the author unless referenced to the contrary in the text.

Some of the work presented in this thesis has been published in journals and conference proceedings - the relevant publications are listed below.

Publications

Yuechun Jiao, Nicholas L. R. Spong, Oliver D. W. Hughes, Chloe So, Teodora Ilieva, Kevin J. Weatherill, and Charles S. Adams. Single-photon stored-light Ramsey interferometry using Rydberg polaritons. *Opt. Lett.*, 45(20):5888–5891, Oct 2020. doi: 10.1364/OL.405143. URL `https://opg.optica.org/ol/abstract.cfm?URI=ol-45-20-5888`

Nicholas L. R. Spong, Yuechun Jiao, Oliver D. W. Hughes, Kevin J. Weatherill, Igor Lesanovsky, and Charles S. Adams. Collectively Encoded Rydberg Qubit. *Phys. Rev. Lett.*, 127:063604, Aug 2021. doi: 10.1103/PhysRevLett.127.063604. URL `https://link.aps.org/doi/10.1103/PhysRevLett.127.063604`

Yuechun Jiao, Oliver D. W. Hughes, Max Z. Festenstein, Zhengyang Bai, Jianming Zhao, Weibin Li, Kevin J. Weatherill, and C. Stuart Adams. Single photonic qutrit in a collective Rydberg polariton, Sep 2025. URL `https://link.aps.org/doi/10.1103/3xnw-cpj2`

Copyright © 2025 by Oliver David Wronski Hughes.

"*The copyright of this thesis rests with the author. No quotation from it should be published without the author's prior written consent and information derived from it should be acknowledged*".

List of Figures

List of Tables

Nomenclature

AOM Acousto-Optic Modulator

AR Anti-Reflection

CAD Computer Aided Design

CCD Charge Coupled Device

CMOT Compressed Magneto-Optical Trap

DAQ Data Acquisition

DExTer Durham Experimental Terminal

ECDL External Cavity Diode Laser

EIT Electromagnetically Induced Transparency

EMCCD Electron Multiplying Charge Coupled Device

EOM Electro-Optic Modulator

FORT Far Off-Resonant Trap

FPGA Field Programmable Gate Array

FSR Free Spectral Range

FWHM Full Width Half Maximum

HBT Hanbury Brown-Twiss

HOM Hong-Ou-Mandel

HWP Half-Waveplate

ITO Indium Tin Oxide

LIAD Light-Induced Atomic Desorption

MOT Magneto-Optical Trap

MTS Modulation Transfer Spectroscopy

NA Numerical Aperture

NEG Non-Evaporable Getter

OD Optical Depth

PBSC Polarising Beam Splitter Cube

PDH Pound–Drever–Hall

PGC Polarisation Gradient Cooling

QIP Quantum Information Processing

QWP Quarter-Waveplate

RGA Residual Gas Analyser

RMS Root Mean Squared

RWA Rotating Wave Approximation

SHG Second Harmonic Generation

SPAD Single-Photon Avalanche Detector

TA Tapered Amplifier

TOF Time-of-Flight

ULE Ultra Low Expansion

UHV Ultra-High Vacuum

ZMTS Zeeman Shifted Modulation Transfer Spectroscopy

Chapter 1

Introduction

The idea that matter interacts with light at discrete frequencies emerged in the early 20^{th} century as classical physics failed to explain a growing body of spectroscopic evidence. Quantum mechanics provided the necessary framework, developed through the foundational work of Planck, Einstein, Bohr and Schrödinger, among others [4, 5, 6]. Bohr's model of the hydrogen atom [7] formalised the notion of quantised energy levels. This was later refined by Schrödinger's wave mechanics and Heisenberg's matrix formulation [8, 9]. Einstein's 1905 explanation of the photoelectric effect introduced the concept that light itself is quantised, laying the foundation for quantum optics [5]. These developments culminated in a coherent picture of atomic structure and light–matter interaction, in which the exchange of photons drives transitions between discrete quantum states. This theoretical foundation successfully explained many of the phenomena that had first been observed experimentally. The focus of research then shifted from explaining natural effects to engineering quantum systems in the laboratory. [10].

This foundation led to the prediction and eventual observation of phenomena such as the photoelectric effect, spontaneous emission and resonance fluorescence [11, 12]. However, many of the more subtle features of light–matter interactions only became experimentally accessible following the invention of the laser in the 1960s [13, 14]. With the availability of stable, narrow linewidth, high intensity light

sources, it became possible to drive and control transitions between quantum states with precision impossible beforehand.

The development of laser cooling and trapping techniques in the 1980s marked a major turning point. In particular, the invention of the Magneto-Optical Trap (MOT) enabled atomic samples to be cooled to microkelvin temperatures, where thermal motion is greatly reduced and long interaction times are possible. [15, 16]. Subsequent advances including optical molasses, sub-Doppler cooling, magnetic and optical traps, have allowed atoms to be prepared in tightly confined, ultra cold ensembles with high phase-space density [17, 18, 19]. These techniques set the stage for precise control of atomic systems and paved the way for modern quantum optics experiments, including those pertinent to this work involving Rydberg atoms and single photons [20, 21, 22, 23, 24].

1.1 Rydberg Physics

A Rydberg atom is one in which a single valence electron has been excited to a high principal quantum number, n. As n increases, the electron's average distance from the nucleus grows, leading to a dramatic enhancement in properties such as electric dipole moment, polarisability and lifetime [25]. Rydberg states are therefore extremely sensitive to external fields and can interact strongly with each other over long distances [25, 26].

One of the most important consequences of these strong interactions is the *Rydberg blockade*. When an atom in a cloud is excited to a Rydberg state, the presence of its dipole moment shifts the energy levels of nearby atoms, preventing them from being resonantly excited [24, 27, 28, 29].As a result, only one Rydberg excitation can occur within a characteristic *blockade radius*, typically a few microns under typical experimental conditions. This allows for the deterministic preparation of a single excitation shared collectively across many atoms within the blockade volume, typically a few microns in radius for Rydberg states around $n \approx 60$ [20, 30].

The Rydberg blockade can be integrated with Electromagnetically Induced Transparency (EIT), in which a probe laser and a coupling laser drive a three-level system to create a *dark-state polariton*, a quasiparticle formed from a coherent superposition of the optical field and the collective atomic excitation, that prevents absorption and renders the atomic medium transparent [22, 31]. In a Rydberg EIT configuration, the intermediate state is coupled to a Rydberg level and the resulting dark state polariton acquires a Rydberg character. This means that two such polaritons can have the characteristic strong Rydberg interactions and be supressed by the Rydberg blockade, enabling nonlinear optical behaviour at the single photon level [32, 33, 34]. This mechanism has been used to demonstrate effects such as photon anti-bunching [34].

In this thesis, the Rydberg blockade plays a central role in suppressing multi photon absorption and enabling coherent dynamics within the Rydberg manifold. By combining Rydberg interactions with tightly focused dipole traps and microwave driving fields, we demonstrate a versatile platform for studying quantum systems and light–matter interactions at the few and single photon level [1, 2].

1.2 Quantum Information Processing

The field of Quantum Information Processing (QIP) seeks to use quantum mechanical systems to store, process and transmit information. Unlike classical bits, which are binary in nature, quantum bits, or qubits, can exist in superpositions of states, and when combined through entanglement can explore an exponentially larger computational space, enabling operations beyond the capabilities of classical computers [35, 36, 37, 38]. Photons have properties that make them excellent carriers of quantum information, but their lack of interactions makes them difficult to use for gates. On the other hand, Rydberg atoms offer strong interactions but are difficult to transmit. Hybrid systems that combine the two offer a promising route forward [20, 21, 39, 40, 41].

In this thesis, we focus on a regime in which photons are stored in atomic ensembles as Rydberg excitations, manipulated using microwave fields and then retrieved [42, 43]. This allows for a flexible and reconfigurable system in which single photon quantum states can be created, transformed and detected. In particular, we expand on previous work conducted on this apparatus [1, 2] and explore the encoding of qutrit states in the Rydberg manifold, where each of the three basis modes correspond to a different retrieval window [3]. These multi-level systems have potential in advanced quantum communication protocols, quantum key distribution and entanglement based networking schemes [37, 38, 44].

We also demonstrate coherent population transfer between Rydberg states and use interferometric techniques to probe the coherence and stability of these manipulations. The ability to perform Ramsey interferometry experiments, control phase shifts and suppress unwanted transitions is crucial for scaling up to more complex systems.

1.3 Single Photon Physics

Single photons are among the most robust and controllable carriers of quantum information. They can travel long distances without dephasing, can be easily generated and detected, and offer a natural interface between remote systems [39, 45]. However, photons do not interact with each other in free space, which presents a major challenge for implementing quantum logic gates, a key element of quantum information processing [46, 47].

This issue can be addressed by mapping photonic states onto atomic degrees of freedom, where interactions can be mediated by internal structure or external fields. In particular, by using a cold, Rydberg blockaded atomic ensemble, it is possible to store a single photon as a collective excitation across the whole ensemble, one can allow that excitation to interact with subsequent photons and fields [32, 33, 48, 49].

The experimental system described in this thesis builds on this idea. Single photons are generated via storage and retrieval processes using Rydberg polaritons [30, 50]. Once stored, the Rydberg excitation can be coherently manipulated using microwave fields, enabling the creation of arbitrary superpositions [1, 49, 51]. These processes are characterised using time-resolved photon counting and correlation measurements. This allows for the demonstration of quantum memory, interferometry and state control [1, 43, 52, 53].

1.4 Thesis Structure

This thesis is structured as follows:

- **Chapter 2: Theory** outlines the theoretical background required to understand the experiments presented in this work. This includes models of atom–light interactions, the three level system underlying EIT, the physics of Rydberg atoms and an introduction to photon counting statistics.
- **Chapter 3: The Experiment** describes the experimental setup in detail. It covers the laser systems, Ultra-High Vacuum (UHV) chamber design, optical layout, cooling and trapping methods, and detection scheme used to perform time resolved single photon measurements. As a mature experiment there was a pre-existing apparatus originally developed within the research group.
- **Chapter 4: Results** presents the main experimental results. We demonstrate single photon storage and retrieval, coherent microwave driven Rydberg dynamics and Ramsey interferometry in the qutrit basis state. The data presented was taken collaboratively with Yuechun Jiao.
- **Chapter 5: Vacuum Break and Experimental Changes** details the vacuum system rebuild following an equipment failure. This includes cleaning, reassembly, bake-out, pump activation and upgrades to optical access

and diagnostics. The hardware upgrades and reassembly described in this chapter were carried out primarily by the author and Max Festenstein.

- **Chapter 6: Characterisation of the New System** presents the characterisation of the rebuilt apparatus. This includes measurements of MOT loading efficiency, compensation field optimisation, beam alignment and temperature measurements. The data presented was taken collaboratively with Aaron Reinhard.

- **Chapter 7: Conclusion and Outlook** summarises the key findings of the thesis and outlines possible future directions for Rydberg based quantum optics and hybrid photon–atom systems.

Chapter 2

Theory

This chapter presents the theoretical framework underlying the experimental work, including the atomic structure of ^{87}Rb, atom-light interactions, the behaviour of Rydberg atoms, laser cooling and trapping, and photon correlation measurements.

2.1 Atomic Physics

2.1.1 Rubidium Atomic Structure

Rubidium is a monovalent alkali metal atom with a single valence electron outside four full shells. Its simple electronic metal structure makes it appropriate for laser cooling, coherent control and precision spectroscopy [15, 20, 54, 55, 56].

The ^{87}Rb isotope has a nuclear spin $I = \frac{3}{2}$, leading to hyperfine splitting in both the ground and excited states due to coupling between the total electronic angular momentum **J** and the nuclear spin **I** [12, 54].

In the ground state, the hyperfine interaction splits the $|5S_{1/2}\rangle$ level into two hyperfine levels with angular momentum $F = 1$ and $F = 2$. The excited $|5P_{3/2}\rangle$ state further splits into four hyperfine levels with $F' = 0, 1, 2, 3$ [54]. This hyperfine structure allows for the implementation of closed cycling transitions using appropriate combinations of cooling and repump lasers, as illustrated in Figure

2.1 [17, 55]. The transition most commonly used in laser cooling is the D_2 line, corresponding to the $|5S_{1/2}\rangle \rightarrow |5P_{3/2}\rangle$ transition [16, 55, 57, 58, 59].

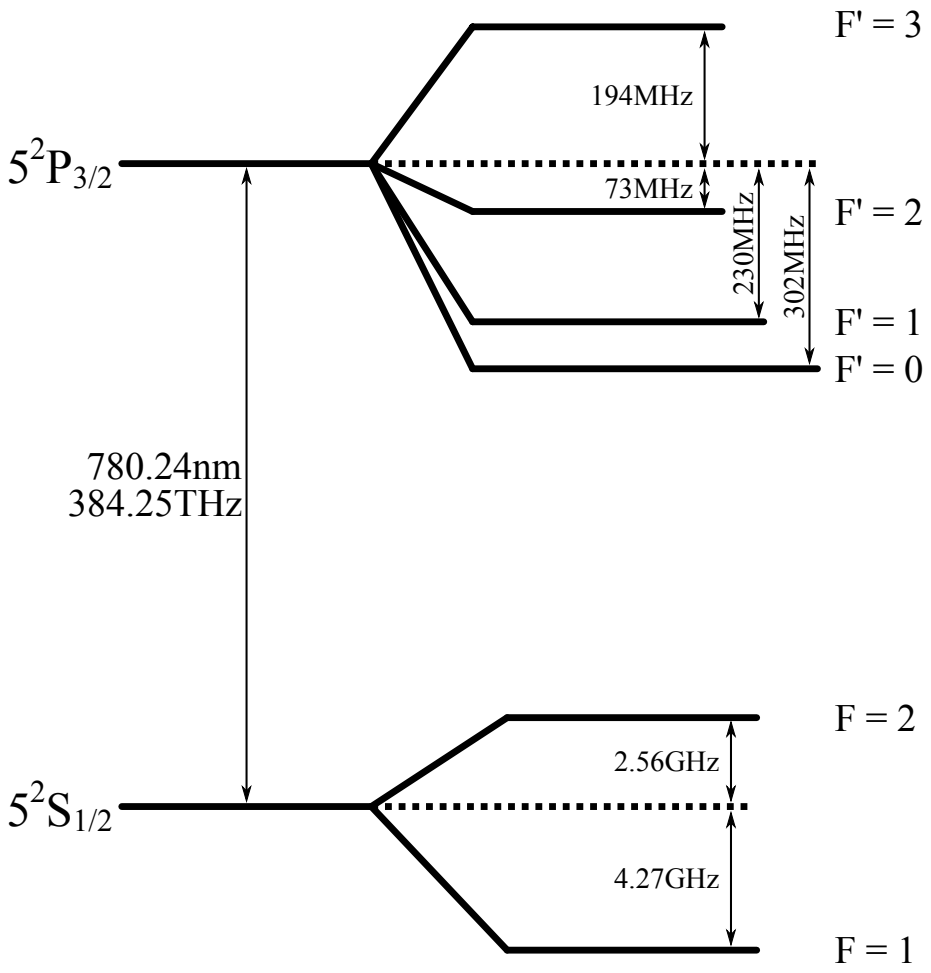

Figure 2.1: Energy level diagram of the ^{87}Rb D_2 transition at 780 nm, showing the ground state hyperfine splitting between $F = 1$ and $F = 2$ and the excited state splitting into $F' = 0, 1, 2, 3$. Values from Daniel Steck's *Rubidium 87 D Line Data* [54]

2.1.2 Atom-Light Interactions

2.1.2.1 Two Level System

The two level atom is the simplest and most instructive model for understanding the interaction between light and matter [12, 60]. It consists of a ground state $|g\rangle$ and an excited state $|e\rangle$, separated by an energy $\hbar\omega_0$. This simple model captures the dynamics of resonant optical transitions and forms the basis for describing atom-light interactions [11, 61]. These configurations are illustrated in Figure 2.2 (Left).

The interaction of the atom with a classical oscillating electric field $\vec{E}(t) = E_0 \cos(\omega t)$ is described by the time-dependent Hamiltonian:

$$\hat{H}(t) = \hat{H}_0 - \hat{d} \cdot \vec{E}(t), \tag{2.1}$$

where $\hat{H}_0 = \hbar\omega_0 |e\rangle \langle e|$ is the atomic Hamiltonian and $\hat{d}$ is the dipole operator. The second term describes the interaction between the atom and the driving electric field.

To simplify the dynamics, we move to the interaction picture and apply the Rotating Wave Approximation (RWA) [12, 60], which removes rapidly oscillating terms that average to zero over time. This approximation focuses on the slowly varying resonant terms that dominate the dynamics when the driving frequency ω is close to the atomic resonance ω_0. This give us the time dependent RWA Hamiltonian:

$$\hat{H}_{\mathrm{RWA}}(t) = \hbar \frac{\Omega}{2} \left(|e\rangle \langle g| \, e^{i\Delta t} + |g\rangle \langle e| \, e^{-i\Delta t} \right), \tag{2.2}$$

where Ω is the Rabi frequency, characterising the rate of coherent population oscillation, and $\Delta = \omega - \omega_0$ is the detuning between the driving field and the atomic resonance. When $\Delta = 0$, the system undergoes resonant Rabi oscillations at frequency Ω. For non-zero detuning, $\Delta \neq 0$, the population oscillates at the effective Rabi frequency $\Omega_{\mathrm{eff}} = \sqrt{\Omega^2 + \Delta^2}$.

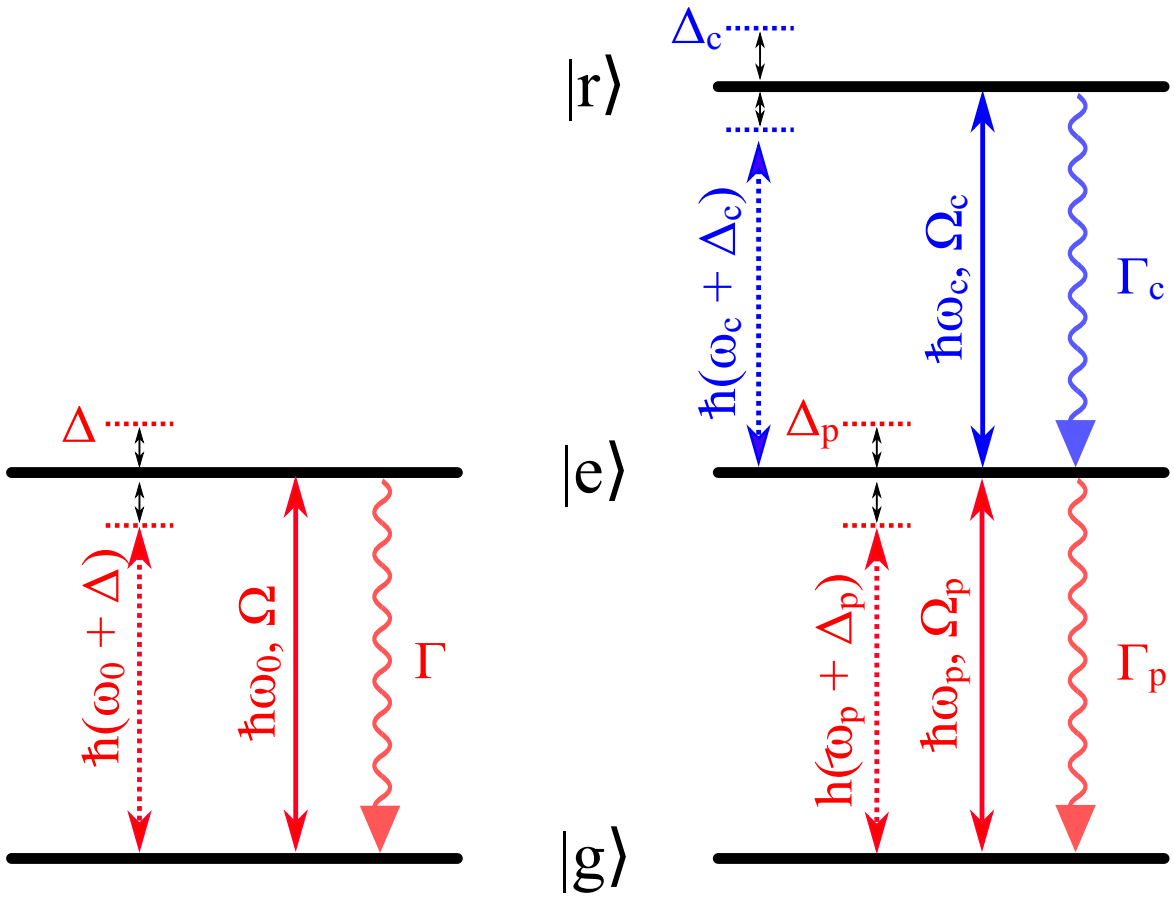

Figure 2.2: Comparison of atomic energy level structures. **Left:** A two level atom with ground state $|g\rangle$ and excited state $|e\rangle$, driven by a near resonant oscillating electric field at frequency ω with detuning $\Delta = \omega - \omega_0$. The field induces Rabi oscillations at frequency Ω and spontaneous decay from $|e\rangle$ occurs at rate Γ. **Right:** A ladder type three level atom (Section 2.1.2.2) with states $|g\rangle$, $|e\rangle$ and $|r\rangle$. A probe field of frequency ω_p couples $|g\rangle \leftrightarrow |e\rangle$ with detuning Δ_p and Rabi frequency Ω_p. A coupling field of frequency ω_c drives $|e\rangle \leftrightarrow |r\rangle$ with detuning Δ_c and Rabi frequency Ω_c. Spontaneous decay from $|e\rangle$ and $|r\rangle$ occurs at rates Γ_p and Γ_c respectively.

In the basis $\{|g\rangle, |e\rangle\}$, the this Hamiltonian takes the matrix form:

$$\hat{H}_{\mathrm{RWA}}(t) = \frac{\hbar}{2}\begin{pmatrix} 0 & \Omega e^{-i\Delta t} \\ \Omega e^{i\Delta t} & 0 \end{pmatrix}. \tag{2.3}$$

The dynamics of the system can be described using the density matrix form-

alism, which provides a convenient framework for representing both pure and mixed quantum states through a single operator. Taking the time-dependent RWA Hamiltonian in Equation 2.2 and neglecting any dissipative processes, the evolution of the system is governed by the von Neumann equation for the density matrix ρ:

$$\frac{d\rho}{dt} = -\frac{i}{\hbar}[\hat{H}_{\mathrm{RWA}}(t), \rho]. \tag{2.4}$$

This equation shows the time evolution driven solely by the Hamiltonian, but does not account for processes such as spontaneous emission. These effects lead to the loss of $|e\rangle$ population and the loss of coherence.

To account for spontaneous emission from $|e\rangle$ to $|g\rangle$ at rate Γ, we model it as an open system governed by the Lindblad master equation [62]:

$$\frac{d\rho}{dt} = -\frac{i}{\hbar}[\hat{H}_{\mathrm{RWA}}(t), \rho] + L[\rho]. \tag{2.5}$$

The term $L[\rho]$ is a Lindblad operator that captures incoherent decay from the excited state $|e\rangle$ to the ground state $|g\rangle$, typically at a rate Γ. This open system framework is essential for modelling realistic atom-light interactions. In the $\{|g\rangle, |e\rangle\}$ basis, the Lindblad term takes the matrix form:

$$L[\rho] = \Gamma \begin{pmatrix} \rho_{ee} & -\frac{1}{2}\rho_{ge} \\ -\frac{1}{2}\rho_{eg} & -\rho_{ee} \end{pmatrix}. \tag{2.6}$$

Combining the matrix forms of $\hat{H}_{\mathrm{RWA}}(t)$ and $L[\rho]$, we obtain the full master equation in matrix form:

$$\frac{d\rho}{dt} = \begin{pmatrix} \dot{\rho}_{gg} & \dot{\rho}_{ge} \\ \dot{\rho}_{eg} & \dot{\rho}_{ee} \end{pmatrix} = -\frac{i}{\hbar}\left[\begin{pmatrix} 0 & \frac{\hbar\Omega}{2}e^{-i\Delta t} \\ \frac{\hbar\Omega}{2}e^{i\Delta t} & 0 \end{pmatrix}, \begin{pmatrix} \rho_{gg} & \rho_{ge} \\ \rho_{eg} & \rho_{ee} \end{pmatrix}\right] + \Gamma \begin{pmatrix} \rho_{ee} & -\frac{1}{2}\rho_{ge} \\ -\frac{1}{2}\rho_{eg} & -\rho_{ee} \end{pmatrix}. \tag{2.7}$$

This matrix representation of the master equation provides a foundation for deriving the optical Bloch equations. By evaluating the matrix equation element by element, we derive the optical Bloch equations, which describe the time evolution of the population and coherence terms:

$$\begin{aligned}
\frac{d\rho_{gg}}{dt} &= \Gamma\rho_{ee} + \frac{i\Omega}{2}(\rho_{eg} - \rho_{ge}) \\
\frac{d\rho_{ee}}{dt} &= -\Gamma\rho_{ee} - \frac{i\Omega}{2}(\rho_{eg} - \rho_{ge}) \\
\frac{d\rho_{ge}}{dt} &= \left(i\Delta - \frac{\Gamma}{2}\right)\rho_{ge} + \frac{i\Omega}{2}(\rho_{ee} - \rho_{gg})
\end{aligned} \tag{2.8}$$

These equations form the basis for modelling dynamics in a wide range of driven atomic systems [11, 12, 60, 61]. When the atom is resonantly driven, they predict the emergence of Rabi oscillations: periodic population transfer between the ground and excited states. The amplitude and damping are dependent on the driving strength and spontaneous emission rate.

The same formalism can also describe Ramsey interferometry, a technique for probing quantum coherence and energy level shifts [63]. In this protocol, two $\pi/2$ pulses are applied, each corresponding to a rotation of the Bloch vector by $\pi/2$ and therefore creating a 50:50 superposition of states, with a period of free evolution in between. During this interval, a relative phase accumulates between the energy eigenstates, leading to interference fringes in the final population when the detuning of the driving pulse is scanned. A subsequent π pulse would instead complete a full inversion between $|g\rangle$ and $|e\rangle$. Both Rabi and Ramsey dynamics are captured by the optical Bloch equations, as illustrated in Figure 2.3.

Ramsey interferometry can be used to quantify the coherence properties of an atom–light system [63, 64]. The coherence time T_2 characterises the timescale over which phase coherence between the ground and excited states is preserved in a driven two level system. It is defined as the time after which the off-diagonal element of the density matrix (ρ_{ge} and ρ_{eg} in Equations 2.7 and 2.8) decays to $1/e$ of its initial value due to dephasing processes. These include spontaneous emission,

laser frequency noise, field fluctuations and Doppler broadening [64, 65].

In a Ramsey sequence (see Figure 3.8) this decay manifests as a reduction in the contrast of the interference fringes (see Figure 2.3). The overall envelope of the fringe pattern is determined by the duration of the $\pi/2$ pulses, which sets the Fourier limited spectral width of the excitation. The width of the central fringe is determined by the free evolution time, but the visibility envelope decays with increasing evolution time according to the coherence time T_2. A longer T_2 produces sharp, high contrast fringes, while a shorter T_2 leads to broader fringes, limiting the precision of the interferometer and its ability to resolve small energy splittings [61, 63, 64, 65].

The two level atom serves as a fundamental model for understanding a wide range of light–matter interactions, from Rabi oscillations to optical pumping and fluorescence. When coupled to an oscillating electric field and modelled using the Lindblad master equation, it provides a simple but powerful description of both coherent dynamics and dissipative effects. In many of the dynamics studied within the Rydberg manifold, the system effectively couples to a lower energy level state, but with a decay rate that is much less than those associated with transitions between Rydberg states [25, 26, 66, 67]. In these cases the dynamics can be accurately captured by a two level model. This framework lays the foundation for more complex schemes including multi-level systems and nonlinear optical effects [11, 12, 20, 21, 22, 26, 31, 48, 68, 69].

2.1.2.2 Three Level System

In a three level ladder system, the atom comprises a ground state $|g\rangle$, an intermediate excited state $|e\rangle$ and a high energy state $|r\rangle$, typically a Rydberg state, separated by an energy $\hbar\omega_p$ and $\hbar\omega_c$ respectively. The system is driven by two oscillating electric fields: one coupling the $|g\rangle \leftrightarrow |e\rangle$ transition and the other coupling the $|e\rangle \leftrightarrow |r\rangle$ transition. These fields are characterised by their Rabi frequencies

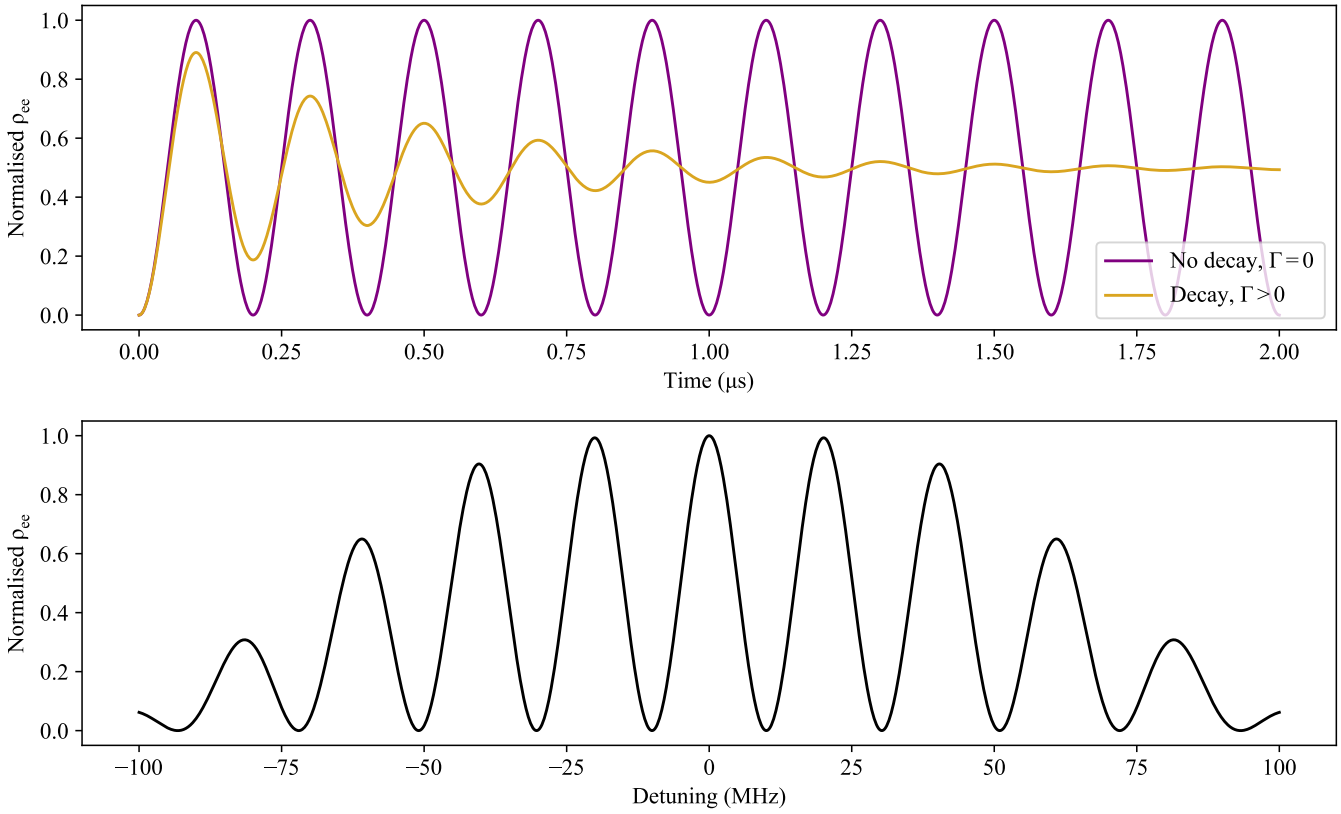

Figure 2.3: Simulated two level atom dynamics using the optical Bloch equations. **Top:** Time evolution of the excited state population ρ_{ee} under resonant driving with Rabi frequency $\Omega = 5 \times 2\pi$ MHz, showing Rabi oscillations. The purple trace corresponds to the ideal case with no decay ($\Gamma = 0$), while the yellow trace includes spontaneous emission at rate $\Gamma = 0.5 \times 2\pi$ MHz, leading to damping. **Bottom:** Ramsey interference fringes in the final ρ_{ee} following a $\pi/2$ – free evolution – $\pi/2$ pulse sequence with pulse duration $t_{\pi/2} = 50$ ns and free evolution time $t_{\text{evo}} = 250$ ns, plotted as a function of detuning Δ across a ± 100 MHz range. The fringe envelope reflects the spectral width of the finite duration $\pi/2$ pulses.

Ω_p and Ω_c and detunings from resonance Δ_p and Δ_c. The three level ladder system described here is illustrated in Figure 2.2 (right). Such configurations form the basis for a range of control techniques, including population transfer, state dressing and interference effects [20, 21, 22, 31].

In a three level ladder system, the atom comprises a ground state $|g\rangle$, an intermediate excited state $|e\rangle$, and a high energy Rydberg state $|r\rangle$, separated by energies $\hbar\omega_{\text{p}}$ and $\hbar\omega_{\text{c}}$, respectively. The system is driven by two oscillating electric fields: one coupling the $|g\rangle \leftrightarrow |e\rangle$ transition and the other coupling the $|e\rangle \leftrightarrow |r\rangle$ trans-

ition. These fields are characterised by their Rabi frequencies Ω_{p} and Ω_{c} and detunings from resonance Δ_{p} and Δ_{c}. In the experiment described in this thesis direct $|g\rangle \leftrightarrow |r\rangle$ optical transition is dipole forbidden and is therefore not driven in this scheme. The specific ladder configuration considered here is illustrated in Figure 2.2(right) and forms the basis for a range of control techniques, including population transfer, state dressing, and interference effects [20, 21, 22, 31].

The total Hamiltonian of the system includes the energies of the states and their interactions with the probe and coupling fields. For an atom interacting with two oscillating electric fields,

$$\vec{E}(t) = \vec{E}_p \cos(\omega_p t) + \vec{E}_c \cos(\omega_c t), \tag{2.9}$$

In general, each field can have a phase, but for simplicity a common reference phase can be chosen so that these phases are set to zero. This choice does not affect the population dynamics described here, as only the relative phase between the fields becomes physically significant in interference-based processes. The atom–field interaction Hamiltonian takes the following form:

$$\hat{H}(t) = \hat{H}_0 - \hat{d} \cdot \vec{E}(t), \tag{2.10}$$

where $\hat{d}$ is the dipole operator. Moving to the interaction picture and applying the RWA, we neglect the fast oscillating terms and obtain a simplified time independent Hamiltonian [12, 60].

The Hamiltonian for the three level ladder system under the rotating wave approximation is:

$$\hat{H} = -\hbar\Delta_p |e\rangle\langle e| - \hbar(\Delta_p + \Delta_c) |r\rangle\langle r| + \frac{\hbar\Omega_p}{2}(|e\rangle\langle g| + |g\rangle\langle e|) + \frac{\hbar\Omega_c}{2}(|r\rangle\langle e| + |e\rangle\langle r|). \tag{2.11}$$

The Hamiltonian in Equation 2.11 captures the coupling of the probe and coupling fields to the intermediate and Rydberg states. When the two-photon detuning is zero and the system reaches a steady state, destructive interference between the excitation pathways via $|e\rangle$ leads to the formation of a dark state with negligible population in the intermediate level. This behaviour will be shown explicitly in Equation 2.16.

In the basis $\{|g\rangle, |e\rangle, |r\rangle\}$, this can be expressed as a 3×3 matrix:

$$\hat{H} = \frac{\hbar}{2} \begin{pmatrix} 0 & \Omega_p & 0 \\ \Omega_p & -2\Delta_p & \Omega_c \\ 0 & \Omega_c & -2(\Delta_p + \Delta_c). \end{pmatrix} \tag{2.12}$$

The diagonal elements give us the detunings from resonance, while the off-diagonal elements describe coupling between the levels via the probe and coupling fields.

To describe the open system dynamics of the three level atom, we can use a density matrix. The state of the system is represented by a 3×3 density operator ρ [11, 35, 68], with elements $\rho_{ij} = \langle i|\rho|j\rangle$ in the basis $\{|g\rangle, |e\rangle, |r\rangle\}$. The time evolution of ρ is governed by the Lindblad master equation (Equation 2.5)

In the three level case, the Lindblad term $L[\rho]$ accounts for population decay and decoherence. It is expressed as a 3×3 matrix in the basis $\{|g\rangle, |e\rangle, |r\rangle\}$:

$$L[\rho] = \begin{pmatrix} \Gamma_e \rho_{ee} & -\gamma_{ge}\rho_{ge} & -\gamma_{gr}\rho_{gr} \\ -\gamma_{ge}\rho_{eg} & \Gamma_r \rho_{rr} - \Gamma_e \rho_{ee} & -\gamma_{er}\rho_{er} \\ -\gamma_{gr}\rho_{rg} & -\gamma_{er}\rho_{re} & -\Gamma_r \rho_{rr} \end{pmatrix}. \tag{2.13}$$

We include population decay from the intermediate state $|e\rangle$ at a rate Γ_e and from the Rydberg state $|r\rangle$ at a rate Γ_r. In addition, we account for decoherence of the off-diagonal elements via phenomenological dephasing rates γ_{ij} for each coherence ρ_{ij}, with $i \neq j$. These rates γ_{ij} include both population decay and dephasing effects, such as laser linewidth or Doppler broadening.

By evaluating the master equation element by element, we obtain the following set of differential equations for the populations:

$$\begin{aligned}
\frac{d\rho_{gg}}{dt} &= \Gamma_e\rho_{ee} + \frac{i\Omega_p}{2}(\rho_{eg} - \rho_{ge}) \\
\frac{d\rho_{ee}}{dt} &= -\Gamma_e\rho_{ee} + \Gamma_r\rho_{rr} + \frac{i\Omega_p}{2}(\rho_{ge} - \rho_{eg}) + \frac{i\Omega_c}{2}(\rho_{re} - \rho_{er}) \\
\frac{d\rho_{rr}}{dt} &= -\Gamma_r\rho_{rr} + \frac{i\Omega_c}{2}(\rho_{er} - \rho_{re})
\end{aligned} \tag{2.14}$$

and coherences:

$$\begin{aligned}
\frac{d\rho_{ge}}{dt} &= (i\Delta_p - \gamma_{ge})\,\rho_{ge} + \frac{i\Omega_p}{2}(\rho_{ee} - \rho_{gg}) - \frac{i\Omega_c}{2}\rho_{gr} \\
\frac{d\rho_{er}}{dt} &= (i\Delta_c - \gamma_{er})\,\rho_{er} + \frac{i\Omega_c}{2}(\rho_{rr} - \rho_{ee}) + \frac{i\Omega_p}{2}\rho_{gr} \\
\frac{d\rho_{gr}}{dt} &= (i(\Delta_p + \Delta_c) - \gamma_{gr})\,\rho_{gr} + \frac{i\Omega_p}{2}\rho_{er} - \frac{i\Omega_c}{2}\rho_{ge}
\end{aligned} \tag{2.15}$$

The equations for ρ_{eg}, ρ_{re} and ρ_{rg} follow as the conjugates of ρ_{ge}, ρ_{er} and ρ_{gr} respectively.

These coupled equations in Equations 2.14 and 2.15 describe the full dynamics of the three level ladder system. Of particular interest is the coherence ρ_{ge}, which determines the absorption and dispersion experienced by the probe field. In the presence of the coupling field Ω_c, quantum interference between excitation pathways can affect the probe response dramatically. This effect gives rise to the phenomenon of EIT, which is examined in more detail below [21, 22, 31, 48].

2.1.2.3 Electromagnetically Induced Transparency

EIT is a quantum interference effect that presents in three level atomic systems driven by two coherent fields. In the ladder configuration, a probe field couples the $|g\rangle \leftrightarrow |e\rangle$ transition, while a coupling field drives the $|e\rangle \leftrightarrow |r\rangle$ transition. When both fields are applied, destructive interference between excitation pathways ($|g\rangle \rightarrow |e\rangle$ and $|g\rangle \rightarrow |e\rangle \rightarrow |r\rangle \rightarrow |e\rangle$) suppresses the population in the intermediate state

$|e\rangle$, opening a transparency window on an otherwise absorbing probe transition [22, 70, 71].

EIT is most clearly revealed by analysing the steady-state behaviour of the coherence ρ_{ge}, which governs both the absorption (via $\mathrm{Im}[\rho_{ge}]$) and dispersion (via $\mathrm{Re}[\rho_{ge}]$) experienced by the probe. In the weak probe regime ($\Omega_p \ll \Omega_c$), the system remains predominantly in the ground state and an analytic expression for ρ_{ge} can be obtained [22]:

$$\rho_{ge} = -\frac{i\Omega_p/2}{\gamma_{ge} - i\Delta_p + \frac{|\Omega_c|^2}{4(\gamma_{gr} - i(\Delta_p + \Delta_c))}} \tag{2.16}$$

This expression reveals a narrow spectral feature centred on two photon resonance, where the combined detuning $\Delta_p + \Delta_c = 0$.

At two photon resonance ($\Delta_p + \Delta_c = 0$), Equation 2.16 reduces to

$$\rho_{ge} = -\frac{i\Omega_p/2}{\gamma_{ge} - i\Delta_p + \frac{|\Omega_c|^2}{4\gamma_{gr}}}.$$

Writing the denominator as $A - i\Delta_p$, with $A = \gamma_{ge} + |\Omega_c|^2/(4\gamma_{gr})$, gives

$$\mathrm{Im}\left[\rho_{ge}\right] = -\frac{\Omega_p}{2}\,\frac{A}{A^2 + \Delta_p^2}.$$

Since the excited-state population $\rho_{ee} \propto \mathrm{Im}\,\rho_{ge}$ in the weak-probe limit, on resonance ($\Delta_p = 0$)

$$\rho_{ee} \propto \frac{1}{A} \approx \frac{4\gamma_{gr}}{|\Omega_c|^2} \ll 1 \quad \text{for} \quad \gamma_{gr} \ll \gamma_{ge}.$$

Thus, at the EIT condition the large real term $|\Omega_c|^2/(4\gamma_{gr})$ suppresses $\mathrm{Im}\,\rho_{ge}$, and therefore the intermediate-state population vanishes.

At this condition, the system evolves into a dark state; a coherent superposition of $|g\rangle$ and $|r\rangle$ that avoids population in the intermediate state. The resulting suppression of absorption on the $|g\rangle \leftrightarrow |e\rangle$ transition is a signature of EIT and can be observed as a peak in the probe transmission spectrum (Figure 2.4) [72].

Since the absorption experienced by the probe is proportional to $\mathrm{Im}[\rho_{ge}]$, the transmitted intensity follows the Beer–Lambert law $T = \exp(-\alpha L)$, where the absorption coefficient $\alpha \propto \mathrm{Im}[\rho_{ge}]$ and L is the medium length. The narrow transparency window therefore corresponds to a local minimum in $\mathrm{Im}[\rho_{ge}]$, producing a peak in the measured transmission.

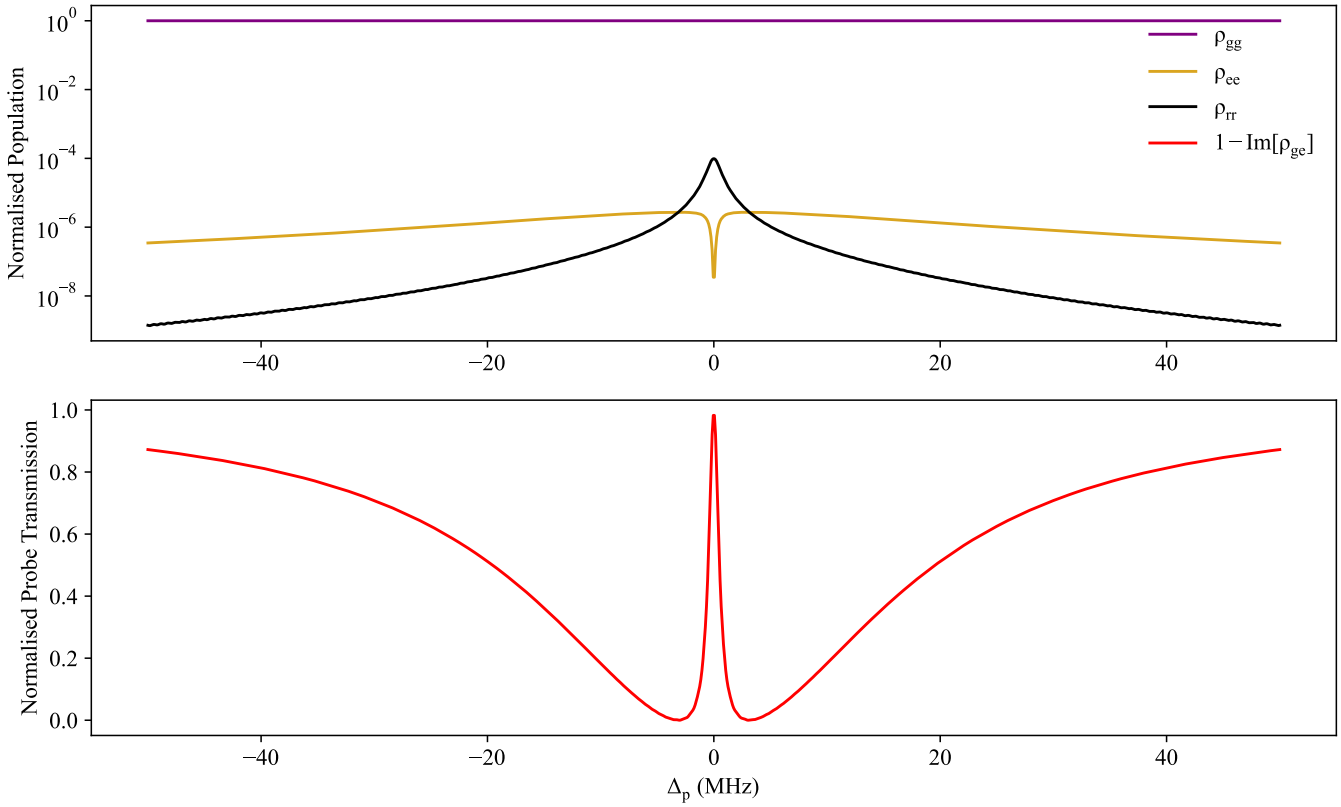

Figure 2.4: Simulated steady-state behaviour of a three-level ladder system under EIT conditions in the weak probe regime ($\Omega_p \ll \Omega_c$). For this simulation, $\Omega_p = 10 \times 2\pi$ kHz and $\Omega_c = 10 \times 2\pi$ MHz **Top:** Populations of the ground state (purple, ρ_{gg}), intermediate state (yellow, ρ_{ee}) and Rydberg state (black, ρ_{rr}) as a function of probe detuning, Δ_p. At two-photon resonance ($\Delta_p + \Delta_c = 0$), destructive interference suppresses population in the state $|e\rangle$, indicating formation of a dark state. **Bottom:** Simulated probe transmission spectrum derived from ρ_{ge}, with absorption proportional to $\mathrm{Im}[\rho_{ge}]$. The plotted quantity corresponds to its inverse. The transmission peak at $\Delta_p = 0$ signals the opening of the EIT window.

The transparency window associated with EIT has a linewidth that depends on the strength of the coupling field and the decoherence rate of the two photon coherence between $|g\rangle$ and $|r\rangle$. This can be estimated by expanding the denominator of

Equation 2.16 at two-photon resonance ($\Delta_p + \Delta_c = 0$), giving us:

$$\Delta\omega_{\mathrm{EIT}} \approx \frac{|\Omega_c|^2}{\gamma_{gr}}. \tag{2.17}$$

This result reflects the fact that stronger coupling broadens the transparency window, shown in the top panel of Figure 2.5.

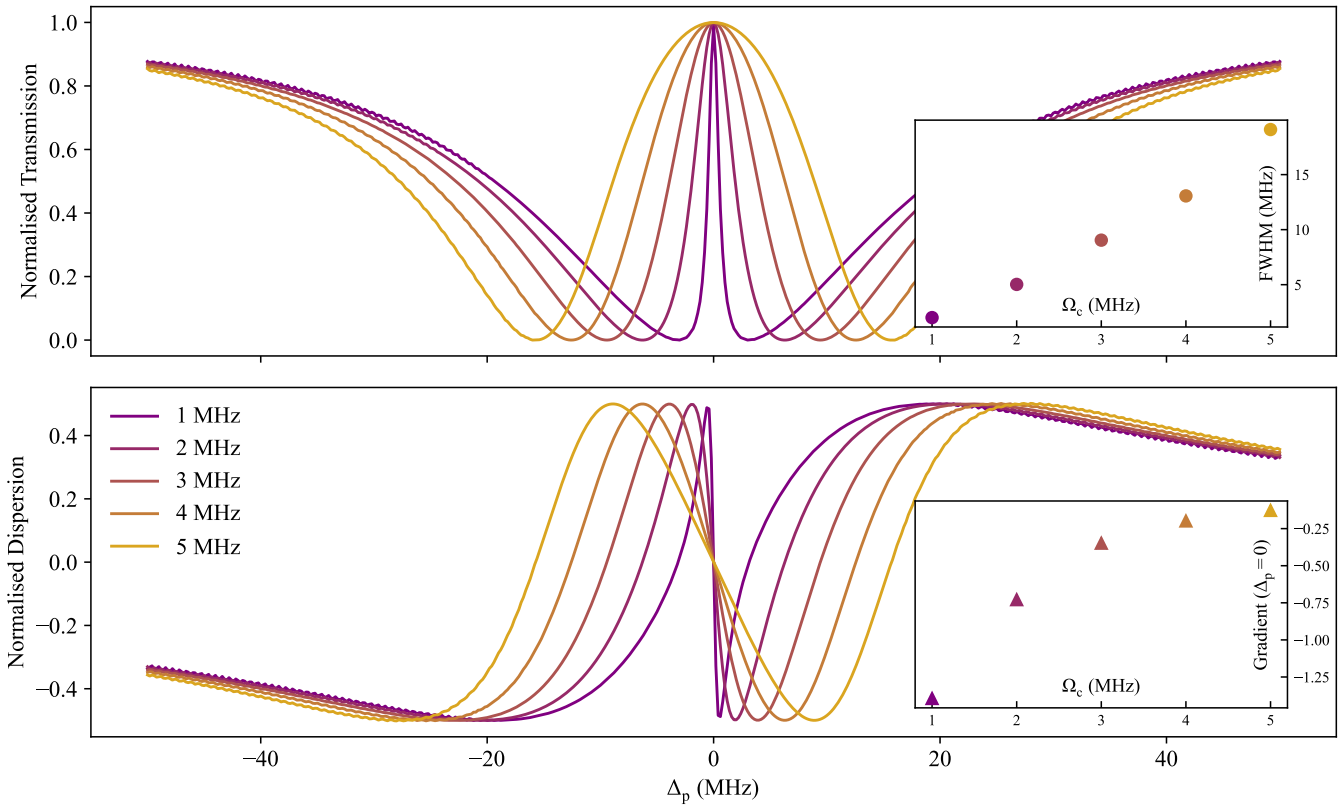

Figure 2.5: Effect of coupling Rabi frequency Ω_c on the transmission and dispersion characteristics of a three-level ladder system under EIT conditions. **Top:** Probe transmission spectra as a function of probe detuning Δ_p for different Ω_c. As the coupling strength increases, the EIT window broadens due to stronger coupling–induced quantum interference between the two excitation pathways ($|g\rangle \to |e\rangle$ and $|g\rangle \to |e\rangle \to |r\rangle \to |e\rangle$). This destructive interference suppresses population in the lossy intermediate state $|e\rangle$, enhancing EIT. Transmission is normalised to the off-resonant probe level, assuming a fixed optical depth corresponding to the linear absorption regime. The inset shows the Full Width Half Maximum (FWHM) of the transparency window as a function of Ω_c. **Bottom:** Real part of the coherence ρ_{ge}, which determines the dispersion experienced by the probe. The slope at resonance steepens with decreasing Ω_c, corresponding to an increased group refractive index and slower group velocity. The inset displays the slope at $\Delta_p = 0$ extracted from each trace. Marker colours in the insets match those in the main panels.

In addition to suppressing absorption, EIT induces steep dispersion near resonance, which strongly modifies the refractive index of the medium. This leads to a dramatic reduction in the group velocity of a probe pulse [73, 74, 75]. Assuming a weak probe and negligible absorption, the group velocity is given by:

$$v_g = \frac{c}{n_g}, \quad n_g = 1 + \frac{\omega}{2}\frac{d}{d\omega}\mathrm{Re}[\chi(\omega)], \tag{2.18}$$

where n_g is the group refractive index, which depends on the frequency derivative of the real part of the susceptibility and $\chi(\omega)$ is the susceptibility of the medium. $\chi(\omega)$ is proportional to the coherence ρ_{ge} via the polarisation $P \propto N d_{ge}\rho_{ge}$, where d_{ge} is the dipole matrix element and N is the atomic density. The steep negative slope $\mathrm{Re}[\rho_{ge}]$ near the EIT resonance (see bottom panel of Figure 2.5) gives rise to group indices $n_g \gg 1$, enabling optical delay, storage and the formation of dark state Rydberg polaritons that are explored in more detail in Sectino 2.2.3 [1, 2, 3, 31, 76, 77].

2.2 Rydberg Atoms

2.2.1 Properties

Rydberg atoms are highly excited atomic states with principal quantum number $n \gg 1$, typically above 30. These states exhibit exaggerated atomic properties, including large spatial extent, long radiative lifetimes, high polarisability and large dipole moments. Such features make Rydberg atoms particularly suitable for exploring strongly interacting systems and enabling nonlinear optical effects at the low and single photon level [25, 67, 78, 79, 80].

The binding energy of a Rydberg state deviates from the hydrogenic model by the quantum defect $\delta_{n\ell j}$. The energy levels are given by:

$$E_n = -\frac{R}{(n - \delta_{n\ell j})^2}, \tag{2.19}$$

where R is the Rydberg constant. The quantum defect depends on the principal quantum number n, orbital angular momentum ℓ and total angular momentum j of the state. These dependencies lead to significant deviations from the hydrogenic scaling.

Several key physical properties of Rydberg states scale strongly with principal quantum number n [25, 67, 78, 79, 80, 81] :

$$\text{Binding energy} \propto n^{-2} \tag{2.20}$$

$$\text{Orbital radius} \propto n^{2} \tag{2.21}$$

$$\text{Radiative lifetime} \propto n^{3} \tag{2.22}$$

$$\text{Polarisability} \propto n^{7} \tag{2.23}$$

$$\text{Dipole moment} \propto n^{2} \tag{2.24}$$

$$\text{Dipole-Dipole Interaction } (C_3) \propto n^{4} \tag{2.25}$$

$$\text{Van der Waals Interaction } (C_6) \propto n^{11} \tag{2.26}$$

Because of their large polarisability, Rydberg states are extremely sensitive to external electric fields. In the limit of small fields, the energy shift is given by the quadratic Stark effect:

$$\Delta E_{\text{Stark}} = \alpha |E|^2, \tag{2.27}$$

where α is the static polarisability of the Rydberg state, which depends on the quantum numbers n, ℓ and j of the state. In general, α increases rapidly with n, scaling approximately as n^7 for low ℓ states. For stronger fields, or when states with different n or ℓ become nearly degenerate, the energy level structure becomes more complex due to state mixing [82, 83, 84].

The extreme polarisability of Rydberg atoms makes them highly sensitive to external electric fields and to the presence of other nearby Rydberg excitations. These

long range dipole–dipole interactions shift the energy levels of neighbouring atoms and form the physical basis of the Rydberg blockade effect discussed in the next section.

2.2.2 Blockade

When atoms are excited to Rydberg states, they experience strong, long range interactions that can significantly perturb the energy levels of nearby atoms. These energy level shifts can prevent the simultaneous excitation of more than one atom within a characteristic volume; a phenomenon known as the *Rydberg blockade mechanism* [24, 26, 27, 28, 85]. This blockade mechanism is illustrated in Figure 2.6.

The form of the interaction between two Rydberg atoms depends on the structure of their pair states and their energy separation. For interatomic separations r, where the pair state $|r, r\rangle$ is far detuned from any dipole coupled states such as $|r, r'\rangle$, the interaction is dominated by second order dipole coupling and takes the van der Waals form

$$V_{\mathrm{vdW}}(r) = \frac{C_6}{r^6}, \tag{2.28}$$

where C_6 is the van der Waals coefficient and r denotes the distance between the two atoms. This regime, characterised by detunings much larger than the resonant dipole–dipole coupling strength, typically corresponds to interatomic separations of several microns for the principal quantum numbers used here. Under these conditions, the interaction strength scales strongly with n, following $C_6 \propto n^{11}$ [29, 79, 81]. This van der Waals regime forms the basis of the Rydberg blockade discussed in the following section.

Alternatively, when a pair state such as $|r, r\rangle$ becomes nearly degenerate with a pair state like $|r, r'\rangle$, the interaction enters the resonant dipole–dipole regime:

$$V_{\mathrm{dd}}(r) = \frac{C_3}{r^3}, \tag{2.29}$$

with $C_3 \propto n^4$. This can occur naturally for specific choices of Rydberg states, or can be engineered using external electric fields to shift energy levels into resonance. For example, the pair state $|nP, nP\rangle$ can be brought into resonance with $|nS, (n+1)S\rangle$ using a small applied field, enabling strong and tunable dipole–dipole interactions [86, 87, 88].

In both cases, the presence of one Rydberg atom shifts the energy levels of surrounding atoms. When the resulting interaction shift exceeds the excitation linewidth or Rabi frequency of the driving field, further excitations are suppressed; the defining feature of the Rydberg blockade.

2.2.2.1 Blockade Radius and Collective Excitation

The strength of the Rydberg interaction determines a characteristic distance where excitation of multiple atoms is suppressed. This distance is known as the *blockade radius* r_b. It is defined as the distance from the Rydberg atom where the interaction shift equals the linewidth or Rabi frequency of the driving transition, whichever is larger:

$$r_b = \left(\frac{C_\kappa}{\hbar\Omega}\right)^{1/\kappa}, \tag{2.30}$$

where C_κ is the interaction coefficient (C_6 or C_3 depending on the regime, $\kappa = 6$ for van der Waals interactions or $\kappa = 3$ for resonant dipole–dipole interactions). At separations smaller than r_b, the energy level shift is larger than the excitation bandwidth, therefore further excitations are blocked.

Within a volume of radius r_b, only a single Rydberg excitation is allowed. If N atoms reside within this volume, they collectively share the excitation. The resulting state is a superposition of all possible single atom excitations:

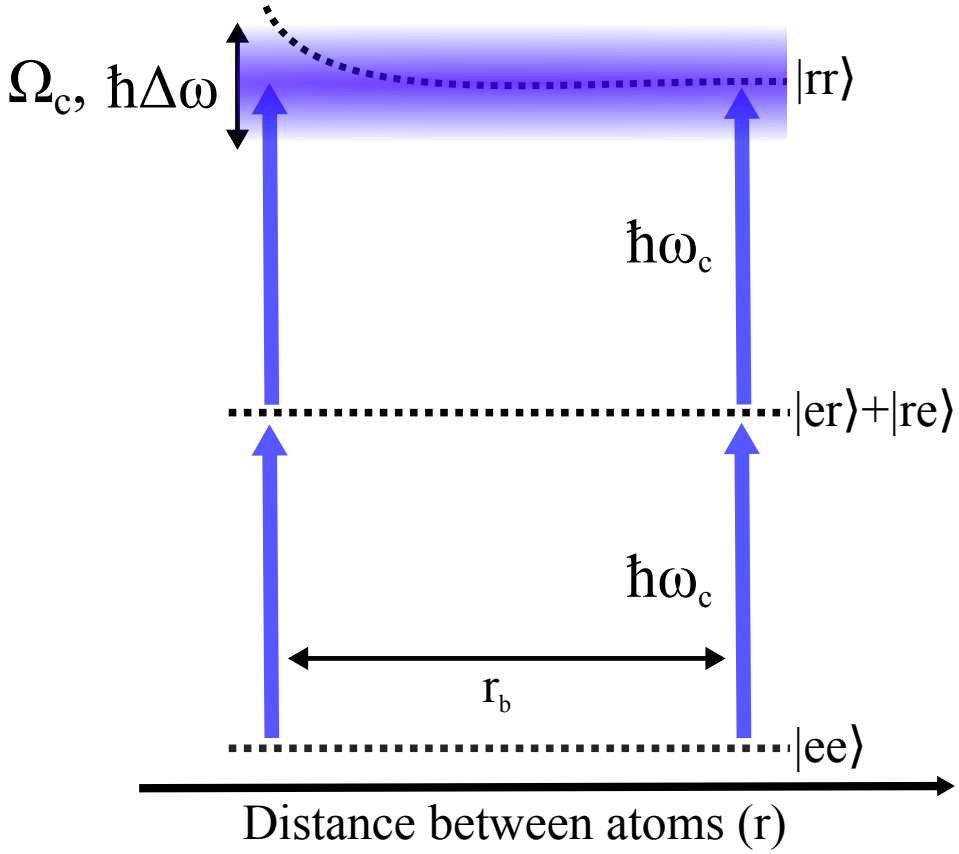

Figure 2.6: Energy level diagram illustrating the Rydberg blockade mechanism in a two atom system. The horizontal axis represents the distance r between two atoms. When both atoms are in the excited Rydberg state $|r\rangle$, their interaction shifts the energy of the doubly excited state $|rr\rangle$. This shift depends on the interatomic distance . If the interaction shift exceeds the excitation linewidth or the Rabi frequency of the driving laser, represented here by $\Delta\omega$ and Ω_c, the doubly excited state becomes off-resonant and inaccessible, preventing simultaneous excitation. The blockade radius r_b is defined as the distance at which the interaction shift equals the excitation bandwidth. At $r < r_b$, only a single excitation is allowed.

$$|\Phi\rangle = \frac{1}{\sqrt{N}} \sum_{i=1}^{N} |g_1 \dots r_i \dots g_N\rangle \,, \tag{2.31}$$

where $|r_i\rangle$ indicates that the i-th atom is in the Rydberg state and all others are in the ground state.

In this state, the excitation is delocalised across the entire ensemble rather than being associated with any particular atom. This collective superposition behaves

as a single effective two level system, often referred to as a *superatom*. Because each atom contributes coherently to the light–matter coupling, the ensemble responds more strongly to the driving field, with measurable consequences for the Rabi frequency and the optical nonlinearity of the medium [24, 48, 89]. The entangled nature of this state also reduces sensitivity to local decoherence processes, since no single atom carries the full excitation [2, 30, 32, 90].

The transition between $|G\rangle$ (all atoms in the ground state) and $|\Phi\rangle$ is driven collectively by the same external field that would drive individual atoms [2, 30, 89, 90]. Since the dipole operator acts identically on all atoms, the coupling amplitudes from each atom in the ensemble sum, resulting in an effective Rabi frequency that scales with the number of atoms as:

$$\Omega_{\text{eff}} = \sqrt{N}\Omega, \tag{2.32}$$

where Ω is the Rabi frequency of the driving field on a single atom.

This *superatom* model captures the essential nonlinear character of Rydberg blockade. Once the ensemble shares a single excitation, further excitation is suppressed.

Blockade also plays a key role in quantum logic gate protocols, where the presence of a single Rydberg excitation in one atom prevents excitation of another, forming the basis of a conditional gate [2, 20, 91, 92, 93, 94]. The same mechanism underpins the suppression of transmission in Rydberg EIT, where photons interact via their shared coupling to the Rydberg state.

2.2.3 Polariton

When a weak probe field propagates through an atomic ensemble under conditions of EIT and the upper state is a Rydberg level, the system supports the formation of *Rydberg dark state polaritons*; quasiparticles that are coherent mixtures of light and collective atomic excitations [23, 33, 77].

In the ladder type EIT scheme relevant here (Figure 2.2), the three participating states are the ground state $|g\rangle$, an intermediate excited state $|e\rangle$ and a Rydberg state $|r\rangle$. The probe field couples the $|g\rangle \leftrightarrow |e\rangle$ transition with Rabi frequency Ω_p and a coupling field drives the $|e\rangle \leftrightarrow |r\rangle$ transition with Rabi frequency Ω_c. When the two-photon resonance condition $\Delta_p + \Delta_c = 0$ is satisfied and in the limit of $\Omega_p \ll \Omega_c$, the system evolves into a collective dark state that avoids population in $|e\rangle$.

The dark state polariton operator takes the form [23]:

$$\hat{\Psi}(z,t) = \cos\theta \hat{E}(z,t) - \sin\theta \hat{\sigma}_{gr}(z,t), \tag{2.33}$$

where $\hat{E}(z,t)$ is the slowly varying envelope of the probe field, $\hat{\sigma}_{gr}(z,t)$ is the coherence between $|g\rangle$ and $|r\rangle$, and θ is the mixing angle. The mixing angle θ determines the relative contributions of the photonic and atomic components of the polariton. Specifically, $\cos^2\theta$ gives the probability that the polariton is in the photonic mode, while $\sin^2\theta$ gives the probability that it resides in the collective atomic excitation. The mixing angle θ is defined by:

$$\tan\theta = \frac{g\sqrt{n}}{\Omega_c}, \tag{2.34}$$

where g is the single atom coupling strength between the probe field and the $|g\rangle \leftrightarrow |e\rangle$ transition, and n is the atomic density. The coupling constant g is related to the dipole matrix element of the transition by

$$g = \frac{\vec{d}_{ge} \cdot \vec{\varepsilon}}{\hbar} \sqrt{\frac{\omega_p}{2\epsilon_0 V}}, \tag{2.35}$$

where $\vec{d}_{ge}$ is the dipole moment of the transition, $\vec{\varepsilon}$ is the probe-field polarisation vector, ω_p is the probe angular frequency, ϵ_0 is the vacuum permittivity, and V is the quantisation volume of the probe mode [12, 23, 95]. This definition connects

g to the same dipole coupling coefficients introduced earlier when discussing the atom field interaction Hamiltonian (Equations 2.1 and 2.10).

As the coupling Rabi frequency Ω_c increases, θ decreases and the polariton becomes more light like. Conversely, as $\Omega_c \to 0$, the polariton becomes increasingly matter like, with most of its character residing in the atomic coherence $\hat{\sigma}_{gr}$. This transition is accompanied by a sharp reduction in group velocity. In the linear regime, the polariton propagates through the medium at [23, 33]:

$$v_g = \frac{c}{1 + \frac{g^2 n}{|\Omega_c|^2}}, \tag{2.36}$$

allowing for substantial optical delay or storage.

The spatial extent of a polariton is set by the Rydberg blockade radius. Within this radius, only a single excitation can be supported, enforcing strong correlations in the transmitted light field.

The use of a Rydberg state as the upper level introduces strong, long range interactions between polaritons due to Rydberg–Rydberg coupling. When two polaritons approach within the blockade radius r_b, the excitation of a second polariton is energetically suppressed. This results in a nonlinear interaction between polaritons mediated by the atomic ensemble. This leads to phenomena such as photon antibunching, two photon suppression and photon–photon interactions [3, 23, 33, 34, 77].

2.3 Atom Trapping and Cooling

The preparation of ultracold atomic ensembles requires a combination of dissipative and conservative trapping techniques. Laser cooling provides a mechanism for reducing the kinetic energy of atoms via momentum exchange with photons, while conservative optical potentials allow spatial confinement of the cold ensemble. In this section, we review the three primary tools used in this experiment: the Magneto-Optical Trap (MOT), optical molasses and the Far Off-Resonant Trap (FORT).

2.3.1 Magneto-Optical Trap

The MOT is a widely used technique for trapping and cooling atoms. It combines spatially varying magnetic fields with position dependent optical forces to confine atoms near the intersection of three orthogonal pairs of counter propagating laser beams [15, 55].

The cooling mechanism relies on the Doppler effect. When an atom moves towards a red detuned beam, it experiences increased scattering from that beam due to the Doppler shift, resulting in a force opposing its motion. This produces a damping force proportional to velocity, slowing, therefore cooling, the atoms.

To achieve spatial confinement, the MOT exploits the Zeeman effect. A quadrupole magnetic field introduces a position dependent energy splitting of the atomic states. With circularly polarised beams, this results in an imbalance in scattering rates depending on the atom's position. Atoms displaced from the trap centre are closer to resonance and therefore preferentially excited by the beam that pushes them back toward equilibrium.

The net force on an atom in the MOT can be approximated for small displacements and velocities as [55]:

$$\vec{F}(\vec{r},\vec{v}) = -\alpha\vec{v} - \kappa\vec{r}, \tag{2.37}$$

where α is the damping coefficient and κ is the spring constant characterising the restoring force. This expression is valid in the low intensity, low velocity regime where the optical force can be linearised.

The resulting atomic distribution in the MOT is determined by the balance between cooling forces and heating due to spontaneous emission. Under typical conditions, the MOT cools atoms to temperatures on the order of hundreds of microkelvin, although the exact value depends on the atomic species and transition linewidth. This cooling is fundamentally limited by the Doppler temperature:

$$T_{\mathrm{D}} = \frac{\hbar\Gamma}{2k_{\mathrm{B}}}, \tag{2.38}$$

where Γ is the natural linewidth of the cooling transition and k_B is the Boltzmann constant. For the D_2 transition in ^{87}Rb ($\Gamma/2\pi \approx 6.07$ MHz), the Doppler limit in ^{87}Rb is approximately $T_{\mathrm{D}} \approx 146$ μK.

2.3.2 Optical Molasses

Optical molasses is a laser cooling technique that provides viscous damping of atomic motion without spatial confinement. Like the MOT, It consists of three orthogonal pairs of counter propagating oscillating electric fields, but with a uniform magnetic field of $B = 0$ [17, 18, 55, 96].

In the absence of magnetic fields, atoms experience no spatially varying Zeeman shifts, but still undergo Doppler cooling. An atom moving toward a beam sees it Doppler shifted closer to resonance, increasing its scattering rate and resulting in a net opposing force. This produces a velocity-dependent damping force:

$$\vec{F} = -\alpha\vec{v}, \tag{2.39}$$

where α is a damping coefficient dependent on detuning, intensity and linewidth.

However, at certain polarisation configurations, such as orthogonal linear polarisations (Sisyphus cooling [17, 97]) or circular counter-propagating beams ($\sigma^+ - \sigma^-$, as used in this work), a spatial variation in light polarisation arises. This enables Polarisation Gradient Cooling (PGC), a sub-Doppler mechanism that allows temperatures well below the Doppler limit.

In a $\sigma^+ - \sigma^-$ PGC scheme, the two counter propagating beams create local light polarisation that varies continuously from circular to linear and back as a function of position. Atoms moving through such a field experience a rotation of the polarisation in their rest frame. Due to finite response time of the atomic dipole, the

induced polarisation lags behind the local field, resulting in a velocity dependent imbalance in the light force. This imbalance leads to a force opposing the atom's motion, thereby reducing its kinetic energy.

This process can cool atoms to temperatures well below the Doppler limit, approaching the fundamental lower bound set by the recoil temperature:

$$T_{\text{recoil}} = \frac{\hbar^2 k^2}{2mk_B}, \tag{2.40}$$

where k is the wavenumber of the cooling light, m is the atomic mass and k_B is Boltzmann's constant. The recoil temperature represents the kinetic energy imparted to an atom from the absorption or emission of a single photon. For the ^{87}Rb D_2 transition at 780 nm, this corresponds to $T_{\text{rec}} \approx 1$ μK [55, 96]. PGC and Raman sideband cooling techniques can approach, but not surpass, this fundamental limit [98, 99].

The reason this is not possible in the presence of magnetic field gradients, as in a MOT, is the spatially varying Zeeman shifts disrupt the energy level structure required for polarisation gradient cooling to operate efficiently. These shifts lift the degeneracy of the ground state Zeeman sublevels and close the optical pumping pathways that underlie this cooling mechanism.

The effectiveness of optical molasses depends sensitively on the intensity balance between beams, detuning, and polarisation. Optimal conditions typically involve large detunings and low powers ($I/I_{\text{sat}} \ll 1$), where I_{sat} is the saturation intensity of the cooling transition [17, 18].

In the system described in this thesis, optical molasses is applied after MOT loading by extinguishing the magnetic field and optimising the cooling beam parameters. The $\sigma^+ - \sigma^-$ configuration used here creates a rotating polarisation field that supports efficient polarisation gradient cooling. This stage reduces the temperature of the ensemble to tens of microkelvin, significantly increasing the phase-space density and improving the efficiency of loading into the dipole trap.

2.3.3 Dipole Trap

For long trapping times and state coherence, atoms are transferred into an optical dipole trap formed by far-detuned oscillating electric fields, a Far Off-Resonant Trap (FORT). The AC Stark effect causes a shift in the energy of the atomic ground state $|g\rangle$ proportional to the local field intensity:

$$U_{\text{dip}}(\vec{r}) = -\frac{1}{2}\alpha(\omega)\langle|\vec{E}(\vec{r})|^2\rangle, \tag{2.41}$$

where $\alpha(\omega)$ is the polarisability of the atomic state at the optical frequency ω and $\vec{E}(\vec{r})$ is the electric field amplitude [100, 101, 102].

To model the polarisability $\alpha(\omega)$ of ^{87}Rb, we consider the dominant contributions from the D_1 ($5S_{1/2} \rightarrow 5P_{1/2}$) and D_2 ($|5S_{1/2}\rangle \rightarrow |5P_{3/2}\rangle$) transitions. In the far-detuned regime, where $\omega \ll \omega_{D1}, \omega_{D2}$, the scalar polarisability can be approximated by:

$$\alpha(\omega) = \frac{|\langle 5P_{1/2}||r||5S_{1/2}\rangle|^2}{\omega_{D1}^2 - \omega^2} + \frac{|\langle 5P_{3/2}||r||5S_{1/2}\rangle|^2}{\omega_{D2}^2 - \omega^2}, \tag{2.42}$$

where ω_{D1} and ω_{D2} are the angular frequencies of the D_1 and D_2 transitions. The reduced dipole matrix elements are given by [54]:

$$|\langle 5P_{3/2}||r||5S_{1/2}\rangle| = 4.227(5)ea_0, \tag{2.43}$$

$$|\langle 5P_{1/2}||r||5S_{1/2}\rangle| = 2.992(3)ea_0, \tag{2.44}$$

with ea_0 the atomic unit of electric dipole moment.

In practice, the trap is formed by a tightly focused Gaussian beam. The trap depth U_0 scales with laser power P and beam waist w_0 as $U_0 \propto P/w_0^2$. The corresponding radial and axial trap frequencies for an atom of mass m are:

$$\omega_r = \sqrt{\frac{2U_0}{mw_0^2}}, \quad \omega_z = \sqrt{\frac{U_0}{mz_R^2}}, \tag{2.45}$$

where $z_\mathrm{R} = \pi w_0^2/\lambda$ is the Rayleigh range of the trapping beam. These trapping frequencies correspond to the oscillation rates of an atom in the harmonic potential near the trap centre. They determine the degree of confinement and the characteristic timescales for atomic motion. Higher trap frequencies result in tighter confinement, increased atomic density and greater phase-space density assuming temperature is constant.

Although the FORT is nominally conservative, atoms still scatter photons due to residual off-resonant coupling to excited states. This leads to heating and decoherence. The photon scattering rate scales as [100]:

$$\Gamma_\mathrm{sc} \propto \frac{\Gamma}{\Delta^2}\frac{I}{I_\mathrm{sat}}, \tag{2.46}$$

where Γ is the natural linewidth of the relevant transition, Δ is the detuning and I_sat is the saturation intensity. To minimise this heating, trapping light is chosen to be far red detuned, for this work at $\lambda = 852$ nm.

The choice of trapping wavelength strongly affects the trap depth and scattering rate. The scalar polarisability of ^{87}Rb increases as the trapping wavelength approaches the D_2 resonance at 780 nm, as shown in Figure 2.7. At 852 nm, used in this experiment, the polarisability is substantially larger than at 1064 nm, a common wavelength in optical trapping. This gives a deeper trap at a lower optical power (Figure 2.8), which is beneficial for improving loading efficiency and maintaining tight confinement. Although the increased photon scattering rate at 852 nm can reduce trap lifetime, this is not a limiting factor in this work, since atoms are held for short durations during fast experimental cycles.

In this system, the FORT plays a central role in preparing a cold, localised atomic ensemble for Rydberg excitation and single photon detection. The use of tightly

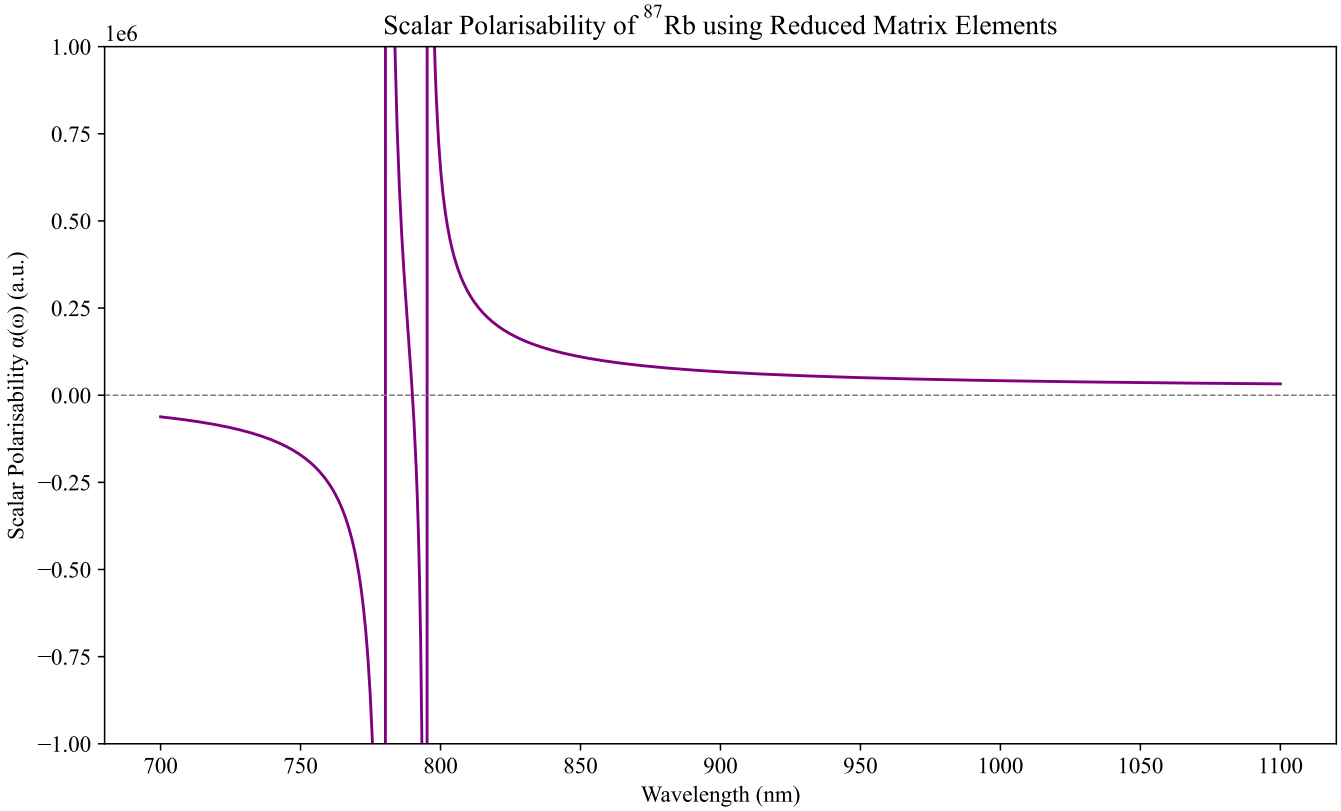

Figure 2.7: Scalar polarisability of ^{87}Rb as a function of trapping wavelength. At shorter wavelengths such as 852nm, the increased polarisability yields stronger optical dipole forces compared to more common infrared trapping wavelengths like 1064nm. The calculation includes only contributions from the dominant D_1 and D_2 transitions, which provide the dominant terms in the far-off-resonant polarisability.

focused, high power light at 852 nm enables strong confinement while maintaining sufficiently low scattering rates for coherent manipulation.

2.4 Photon Counting Statistics

Measurements of photon correlations provide key insights into the quantum nature of light and its interaction with atomic media. In the context of this work; these correlations serve as powerful diagnostics for photon–photon interactions, Rydberg blockade and the emergence of non-classical states of light [34, 42, 77].

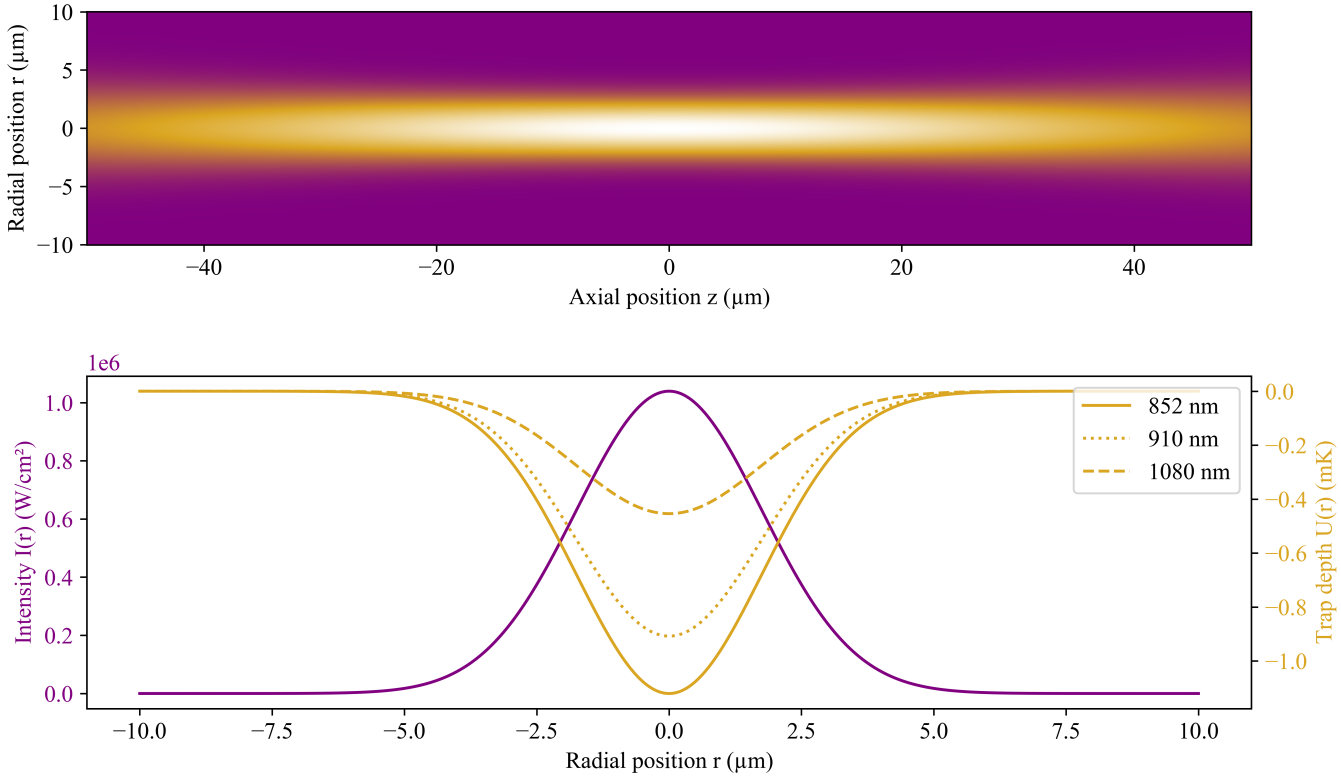

Figure 2.8: Optical dipole trap intensity and potential profile for three trapping wavelengths. The beam is assumed to be Gaussian with waist $w_0 = 3.5\mu$m and optical power $P = 200$ mW. The lower panel shows the resulting potentials in millikelvin. The trap becomes shallower with increasing wavelength due to the reduced polarisability.

2.4.1 Second-Order Correlation Function $g^{(2)}$

The second-order correlation function is defined as:

$$g^{(2)}(\tau) = \frac{\langle \hat{E}^\dagger(t)\hat{E}^\dagger(t+\tau)\hat{E}(t+\tau)\hat{E}(t)\rangle}{\langle \hat{E}^\dagger(t)\hat{E}(t)\rangle^2}, \tag{2.47}$$

where $\hat{E}(t)$ is the electric field operator. Physically, $g^{(2)}(\tau)$ quantifies the conditional probability of detecting a second photon at time $t+\tau$ given that one was detected at time t [61, 103].

In classical optics, intensity fluctuations lead to $g^{(2)}(0) \geq 1$. A value of $g^{(2)}(0) = 2$ is characteristic of thermal or chaotic light, indicating strong bunching behaviour; the detection of one photon increases the likelihood of detecting another shortly after.

For coherent light, such as that emitted by a laser, $g^{(2)}(0) = 1$, meaning the detection of one photon gives no information about the timing of the next. In contrast, non-classical light fields can exhibit $g^{(2)}(0) < 1$, a signature of photon antibunching [104, 105]. In this regime, the detection of one photon *reduces* the probability of detecting another immediately afterward, reflecting the discrete nature of photon emission .The limiting case $g^{(2)}(0) = 0$ corresponds to a Fock state [11], a purely single photon source, containing exactly one photon, where detection of a photon precludes the immediate detection of another.

For multi-mode fields or spatially separated regions, the cross-correlation function is used:

$$g_{ij}^{(2)}(\tau) = \frac{\langle \hat{E}_i^\dagger(t)\hat{E}_j^\dagger(t+\tau)\hat{E}_j(t+\tau)\hat{E}_i(t)\rangle}{\langle \hat{E}_i^\dagger(t)\hat{E}_i(t)\rangle\langle \hat{E}_j^\dagger(t+\tau)\hat{E}_j(t+\tau)\rangle}. \tag{2.48}$$

This is relevant for correlating light from different spatial modes, such as distinct photonic channels. In the case of two spatially separated channels, $g_{ij}^{(2)}(\tau)$ quantifies correlations between photons emerging from each region. A value of $g_{ij}^{(2)}(0) > 1$ indicates correlated emission across the channels, while $g_{ij}^{(2)}(0) < 1$ reveals inter channel antibunching: evidence that the presence of a Rydberg excitation in one channel suppresses transmission in the other due to the blockade mechanism.

2.4.2 Hanbury Brown–Twiss Interferometry

Second-order correlations are typically measured using a Hanbury Brown-Twiss (HBT) setup, in which the light is split by a 50:50 beamsplitter and directed to two independent single-photon detectors. Detection events are time tagged, and a histogram of detection delays τ is constructed to obtain $g^{(2)}(\tau)$, which quantifies the normalised coincidence rate between the two detectors [61, 106, 107, 108]. The practical implementation of this measurement, including the time-tagging electronics and data normalisation procedure, is described in Section 3.7 and 4.2.1.

Second-order correlations are typically measured using a HBT setup, in which the light is split by a 50:50 beamsplitter and directed to two independent single photon detectors. Detection events are time tagged and a histogram of detection delays τ is constructed to obtain $g^{(2)}(\tau)$ [61, 106, 107, 108].

In a Rydberg blockaded system, strong interactions between polaritons lead to the suppression of simultaneous excitations within a blockade volume. When one polariton is present, nearby atoms are shifted out of resonance, preventing the transmission of another polariton. This leads to suppressed coincidence counts, ($g^{(2)}(0) < 1$) [30, 34, 42]. The depth of the $g^{(2)}(0)$ dip indicates how close the source is to ideal single photon behaviour and thus indicates how effectively the Rydberg blockade is suppressing multiple excitations.

Photon correlation measurements provide a sensitive and non-destructive probe of the quantum dynamics within strongly interacting atomic ensembles. They reveal both the statistical character of the light and the underlying mechanisms of atomic nonlinearity and coherence [33, 34, 77, 109].

Chapter 3

The Experiment

3.1 Overview

This chapter describes the experimental apparatus used to cool and trap ^{87}Rb atoms for the preparation, manipulation and measurement of collective Rydberg excitations. The system comprises a suite of laser systems, vacuum chambers and electronic control hardware, all designed to support high repetition rate experiments, single photon detection and coherent state control. The following sections outline each subsystem and their integration into the complete experimental platform.

The experimental apparatus has three main parts. First, the various lasers systems, which allow us to do the required cooling, trapping and atomic excitation processes. Second, the UHV chambers, which allow us to maintain the conditions required for these processes to work. Lastly, the detection and control systems.

The chamber is split into two parts, the upper 2D MOT cell and the lower 3D MOT and science chamber. This dual chamber configuration allows for precooling of the atoms before they enter the science chamber, enabling fast repetition rates ($\mathcal{O}(10\ kHz)$) of the experimental cycle [1, 2, 110, 111]. The setup that will be described in this chapter was initially designed and built by Hannes Busche, Paul Huillery and Simon Ball [112, 113]. Changes to this design will be outlined in

Chapter 5, along with the reconstruction process due to an unscheduled vacuum break.

We derive all the MOT cooling beams for both MOTs, the pusher beam and the experimental probe beam from the same laser with 780 nm, since they address the same transition, although with different detunings, allowing for fewer points of failure in the experiment. However, the repump transition, despite also requiring a laser 780 nm wavelength, is far enough detuned that it is not feasible to derive from the same laser as the cooling transitions. For the FORT and Rydberg excitation, we use lasers with 852 nm and 480 nm wavelengths respectively.

3.2 Laser Systems

Before describing each subsystem in detail, we summarise the primary laser systems used in the experiment. Each system is defined by its wavelength, configuration and role in addressing specific atomic transitions. A brief overview is provided in Table 3.1.

Table 3.1: Summary of laser systems used in the experiment. Each system is identified by manufacturer, model and operating wavelength.

Laser (Model and Wavelength)	**Transition Addressed**	**Main Function(s)**
Toptica TA Pro (780 nm)	$\|5S_{1/2}, F = 2\rangle \rightarrow \|5P_{3/2}, F = 3\rangle$	MOT cooling beams, absorption imaging, probe beams, pushing beam
Toptica DL Pro (780 nm)	$\|5S_{1/2}, F = 1\rangle \rightarrow \|5P_{3/2}, F = 2\rangle$	MOT repump beams
Toptica TA Pro (852 nm)	Off-resonant (to both D_1 and D_2 lines)	Dipole trapping beam
Toptica TA-SHG (Pro and 110) (480 nm)	$\|5P_{3/2}\rangle \rightarrow \|nS_{1/2}\rangle$	Excitation to a Rydberg state

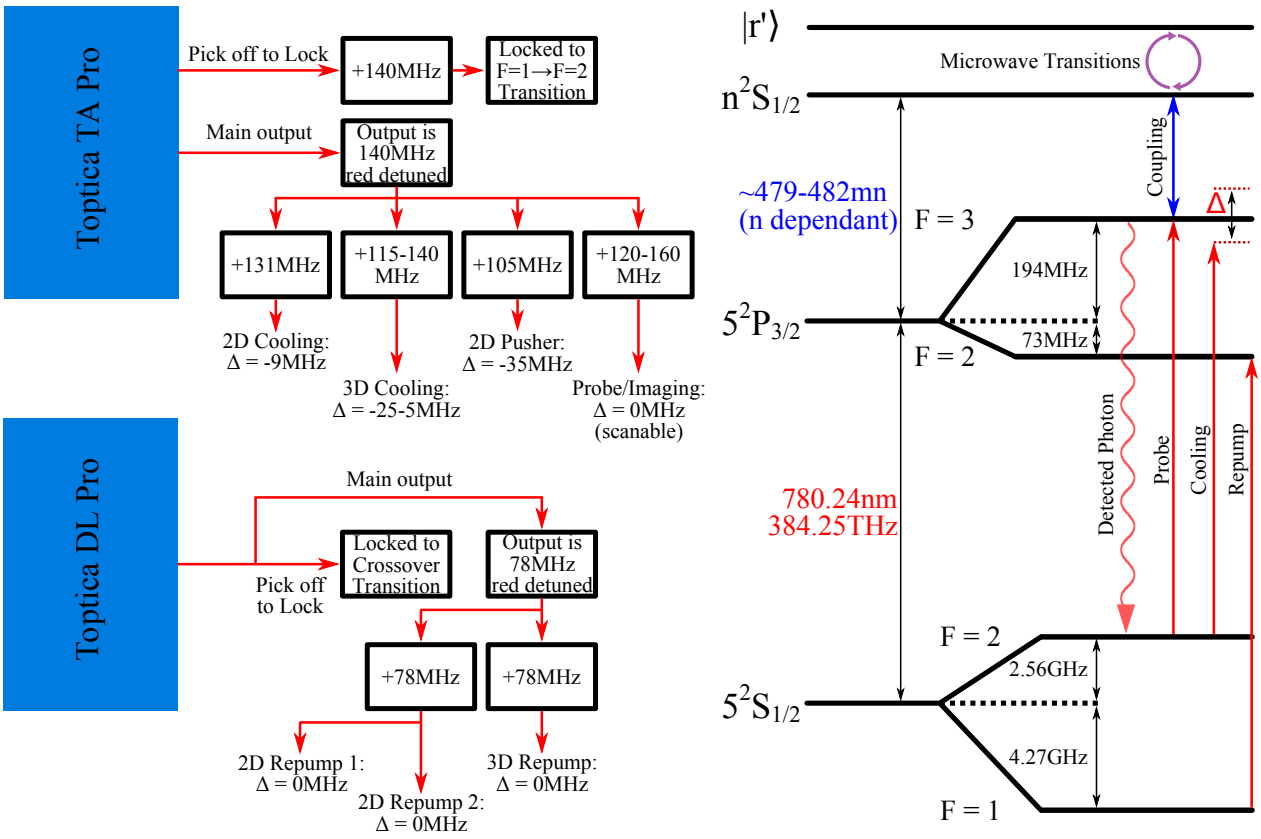

Figure 3.1: Laser frequency configuration and energy level diagram for ^{87}Rb. **Left:** Schematic showing the frequency detunings of laser beams used in the experiment. The cooling and probe beams are derived from a Toptica TA Pro laser locked 140 MHz below the $F = 2 \rightarrow F' = 3$ transition, with detuning and switching controlled via AOMs. The repump laser (Toptica DL Pro) is locked at the crossover resonance between the $F = 1 \rightarrow F' = 1$ and $F = 1 \rightarrow F' = 2$ transitions using a ZMTS scheme (see Section 3.2.2.1). AOMs are used to bring the light to resonance. Detunings for typical beam configurations are indicated in the schematic. **Right:** Energy level diagram showing the hyperfine structure of the ground and excited states used in the experiment, along with the two photon excitation path to a Rydberg state $|nS_{1/2}\rangle$ via a 480 nm coupling beam. Microwave transitions between Rydberg states are also indicated.

3.2.1 Cooling Laser - 780 nm

The laser used for the cooling beams in both 2D and 3D MOTs, the experimental probe beams and absorption imaging beam, addressing the $|5S_{1/2}, F = 2\rangle \rightarrow |5P_{3/2}, F = 3\rangle$ transition, is a Toptica TA Pro consisting of a commercial External

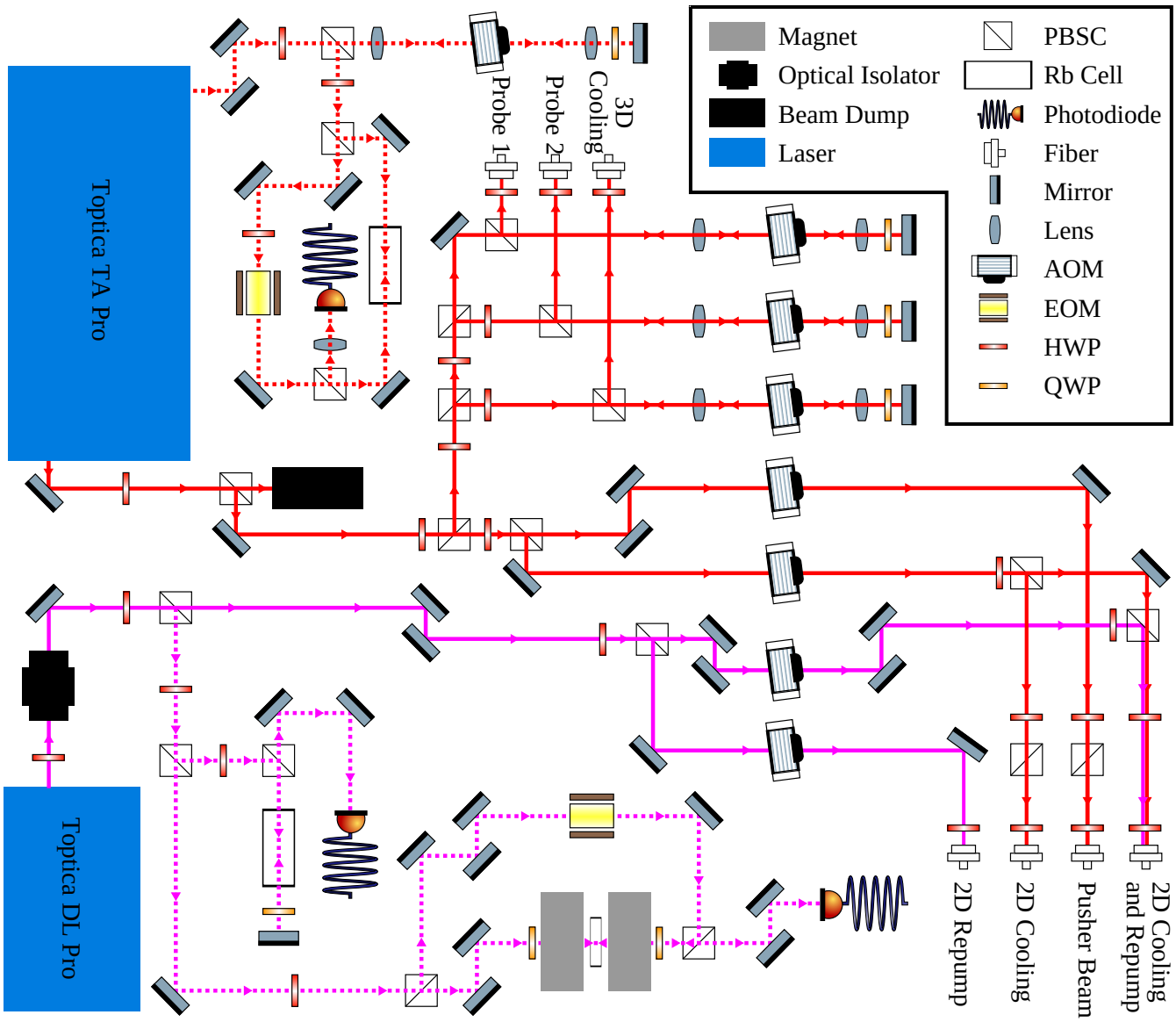

Figure 3.2: Beam path diagram for the 780 nm cooling/probe/imaging laser (Toptica TA Pro, red lines) and the 780 nm repump laser (Toptica DL Pro, magenta lines). The setup distributes light for the 2D and 3D MOTs, pushing beam, imaging and probe beams. Solid lines represent main paths, while dashed lines of matching colour denote paths used for frequency stabilisation. Frequency locks are implemented via modulation transfer spectroscopy using Rubidium vapour cells and photodiodes. Key AOMs, EOMs, fibre couplers, beam dumps, PBSCs, HWPs and QWPs are labelled. Paths are arranged to allow independent frequency and power control of each beam using AOMs and the output beams are fibre coupled for delivery to the experiment. This layout forms the core of the optical table used for delivering stabilised 780 nm light.

Cavity Diode Laser (ECDL) with a Tapered Amplifier (TA), controlled and locked by a Toptica DLC Pro. The internal ECDL seed laser produces 80μW of power increased to a maximum of ≈2.5W after the TA. The system includes two internal optical isolators to prevent back reflections into the ECDL and TA. The laser has a small pick off output channel (P ≈20 mW) which is used for locking the ECDL.

The main output light is split into multiple channels using Half-Waveplate (HWP)s and Polarising Beam Splitter Cube (PBSC)s. The cooling laser system is responsible for the following in the experimental setup:

- **Probe Beams**: Two probe beams are derived from the cooling laser and used for imaging and probing the atomic ensemble. These beams are passed through Acousto-Optic Modulator (AOM)s for precise frequency and intensity control. This channel is also used for absorption imaging of the MOT.
- **2D MOT Cooling**: The cooling light for the 2D MOT passed through an AOM, then split into separate paths for each of the two axes. One of these axes is combined with repump light, using a PBSC and delivered to the experiment in the same fibre.
- **3D MOT Cooling**: The cooling light for the 3D MOT passed though an AOM for precise frequency and intensity control. It is combined with repump light using a custom Evanescent Optics fibre combiner/splitter. This combiner/splitter then splits the combined light into three beams, one for each axis of the 3D MOT.
- **Pushing Beam**: The pushing beam is detuned such that it interacts with the atoms in the atomic beam released by the dispensers which have upwards momentum away from the science chamber and "pushes" them towards it.

The AOMs also allow us to precisely and stably set the detuning of each beam path and vary the power and act as shutters. Each beam path includes its own AOM, allowing the detuning for every function of this laser to be controlled independently.

Since we need to change the frequency of the probe and 3D cooling light during an experimental run we pass them through a separate double pass AOM setup. This allows us to change the frequency whilst limiting the deviation of the beam going into the fibre, thus maintaining a nearly consistent coupling efficiency.

3.2.1.1 Frequency Stabilisation - Modulation Transfer Spectroscopy

Frequency stabilisation of the cooling laser is achieved using Modulation Transfer Spectroscopy (MTS), a highly stable locking technique, on the pick off beam [114, 115]. The MTS setup involves modulating the pump beam at 10 MHz using an Electro-Optic Modulator (EOM) and counter propagating it with an unmodulated probe beam in a Rubidium vapour cell. The resulting error signal, generated via a four wave mixing process, is used to lock the ECDL to the $|5S_{1/2}, F = 2\rangle$ to $|5P_{3/2}, F = 3\rangle$ transition. The MTS technique produces a high signal to noise ratio error signal, ensuring long term stability of the cooling laser. Since MTS only works on closed transitions where population cycling is maintained and the lock cannot jump to the nearby open transitions present in ^{87}Rb

The cooling laser is locked 140 MHz below resonance by passing the pick off light through a double pass AOM setup. This detuning is necessary to ensure that the cooling light can be precisely tuned to the required frequency for magneto-optical trapping and other experimental processes. Since the AOMs we use to shift the frequency of the 3D MOT cooling and probe light cannot shift the few MHz from resonance which we desire, instead, we lock below resonance and then shift back close to resonance such that the final output has the desired detuning (see Figure 3.1).

3.2.2 Repump Laser – 780 nm

The repump laser addresses the $|5S_{1/2}, F = 1\rangle \rightarrow |5P_{3/2}, F = 2\rangle$ cycling transition in ^{87}Rb, ensuring efficient optical pumping of atoms into the $|5P_{3/2}, F = 2\rangle$ state

and that none are trapped in the $|5S_{1/2}, F = 1\rangle$ dark state. For this, a Toptica DL Pro ECDL laser is used, with an output of 90 mW, more than sufficient to supply repump light for both the 2D and 3D MOTs.

The main output light is split into three channels using a series of HWPs and PBSCs pairs; 2D MOT, 3D MOT and the locking system. The outputs are coupled to fibres and sent to the vacuum chamber. The 2D repump light is coupled into the same fibre as one of the 2D cooling axes, overlapping the two beams (with orthogonal polarisation) using a PBSC. The 3D repump light is combined with the cooling light in the same combiner/splitter as described above (Section 3.2.1).

3.2.2.1 Frequency Stabilisation - Zeeman Shifted Modulation Transfer Spectroscopy

To ensure that the repump light remains on resonance, the system employs a tunable Zeeman Shifted Modulation Transfer Spectroscopy (ZMTS) locking scheme [116] (magenta dashed line in Figure 3.2). This technique is a modified version of conventional MTS, adapted to lock the laser to an open transition. The ZMTS setup involves applying a large magnetic field to a small rubidium vapour cell, shifting the atomic energy levels into the hyperfine Paschen–Back regime. By fine adjustment of the magnet position, a controllable frequency offset within the accessible Zeeman shift range of a closed transition can be achieved. Historically, this laser was locked to the *crossover resonance* between the $F = 1 \rightarrow F' = 1$ and $F = 1 \rightarrow F' = 2$ transitions, where overlapping Doppler-broadened absorption profiles of the two lines provide a convenient reference point. During implementation of the ZMTS scheme, the target transition ($F = 2 \rightarrow F' = 3$) was shifted magnetically to coincide with this crossover frequency to minimise disruption to the optical setup, and the final detuning to the required resonance was applied using an AOM. The magnets provide a field strength of approximately 0.6 T, allowing the Zeeman-shifted modulation transfer signal to be tuned continuously over more than 15 GHz across the D_2 spectrum, sufficient to translate the $F = 2 \rightarrow F' = 3$ transition onto the

$F = 1 \rightarrow F' = 2$ repumping transition [116]. This approach enables a stable and flexible locking point that retains the advantages of MTS while providing tunability across the hyperfine manifold. The ZMTS setup uses a 2 mm rubidium vapour cell, ensuring a uniform magnetic field and sufficient optical depth when heated to 120 °C.

3.2.3 Dipole Trapping Laser - 852nm

The laser used for the dipole trap is a Toptica TA Pro consisting of an ECDL with a TA, controlled by a Toptica DLC Pro. The system includes two internal optical isolators to prevent back reflections into the ECDL and TA. Its output is approximately 1 W, however no more than 250 mW is required for the trap so most of that is directed into a beam dump. This system uses an AOM to control switching, and PBSC and HWP pairs to vary power. The output light is fibre coupled to the experiment, where it is tightly focused by high Numerical Aperture (NA) lenses to produce a highly confined optical trap.

The 852 nm laser operates at a wavelength far from any atomic resonances, meaning that frequency fluctuations have no significant impact on the trap depth over the timescales relevant to these experiments. As a result, the laser is not locked to a specific frequency, simplifying the setup while maintaining sufficient stability for trapping. The system relies on the inherent stability of the ECDL and TA, which provide narrow linewidth and stable output power.

3.2.4 Coupling Laser - 480nm

To make the transition from $|5P_{3/2}\rangle$ to a Rydberg state, $|nS_{1/2}\rangle$, we use a Toptica TA-SHG Pro and a TA-SHG 110. Primarily the TA-SHG Pro system is used, which replaced the TA-SHG 110, however there is scope for both to be used simultaneously in future experiments addressing two different Rydberg states. The new system offers greater stability, ease of use and higher power at 480 nm. Similarly to the

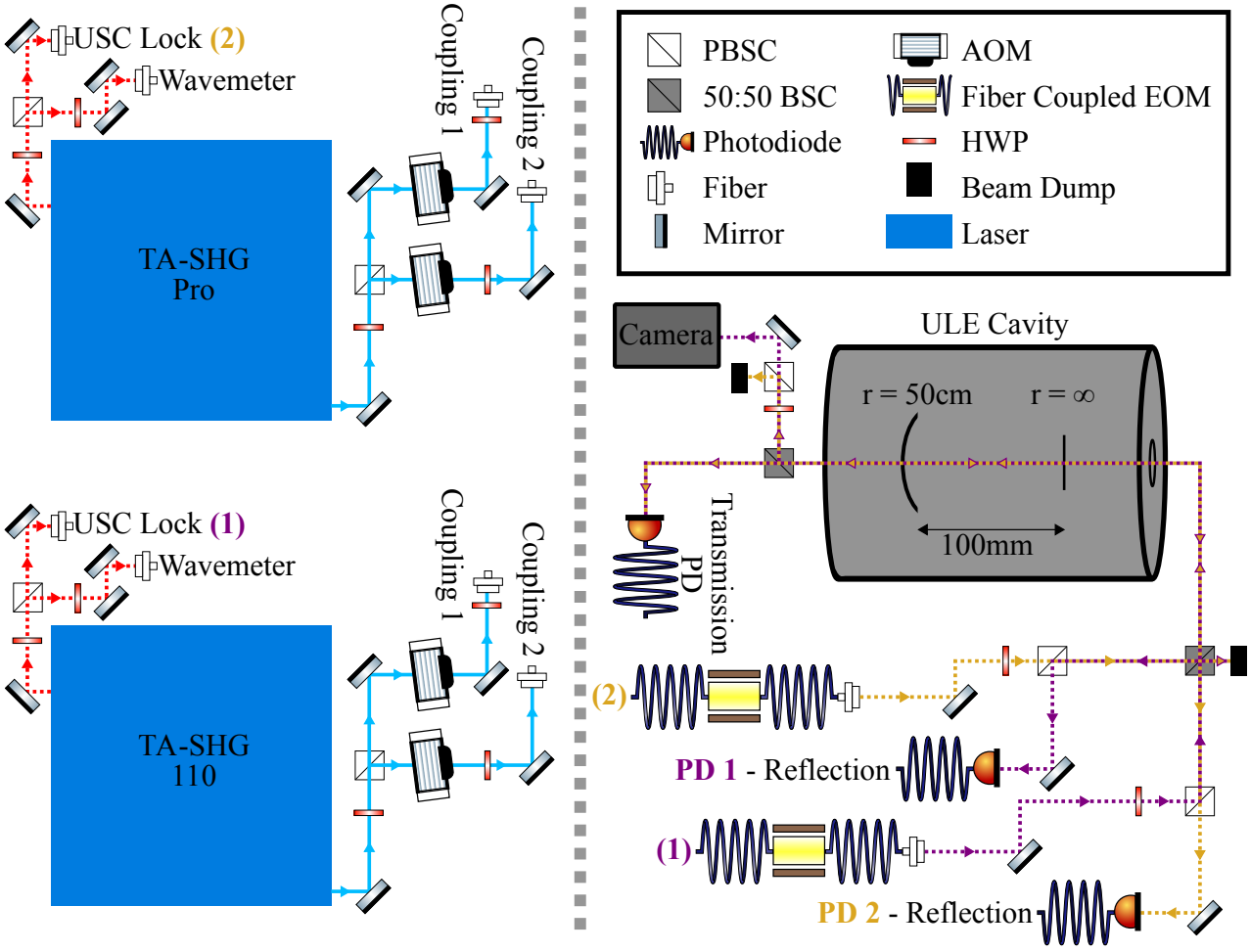

Figure 3.3: Optical setup for generating and stabilising the 480 nm coupling light used to drive the Rydberg transition. **Left:** Beam paths for the two coupling lasers. Fundamental light at 960 nm from two Toptica TA-SHG systems (TA-SHG 110 and TA-SHG Pro) is frequency doubled to produce 480 nm output (blue lines). The doubled beams are delivered to the experiment via optical fibres, with AOMs used for switching and power control. A portion of the fundamental (960 nm) light is picked off (dashed red lines) before the SHG stage for frequency stabilisation. **Right:** PDH locking scheme for stabilising both 960 nm lasers to a ultra stable cavity. Orthogonal linear polarisations (created using HWPs and PBSCs) allow the two laser beams to be combined and coupled into the same cavity. Reflected light is separated onto two photodiodes (PD1 and PD2) for generating individual error signals, while transmitted light is monitored for diagnostics. A fibre-coupled EOM applies sidebands for the PDH lock. This dual locking scheme enables stable, independent control of the coupling frequencies for two Rydberg excitation channels.

other Toptica DL Pros described this laser contains an ECDL and a TA, producing light over the range of 945 nm - 965 nm. Here there is a pick off which we use to lock the laser. After the pick off the remaining light goes through a Second Harmonic Generation (SHG) bow tie cavity to double its frequency, making its wavelength the desired 480 nm. The preparation of the output light is simple. The frequency doubled light is split two ways for each laser and goes to the vacuum chamber via separate fibres. Each path is switched with an AOM and its power varied with PBSC and HWP pair. The 480 mn power at the TA-SHG Pro output is as high as 1.5 W, an order of magnitude more than the previously solely used TA-SHG 110, which has a maximum output of $\approx$ 300 mW.

3.2.4.1 Frequency Stabilisation - Pound-Drever-Hall

The narrow linewidths of the transitions to the Rydberg states, particularly for high n states, require precise frequency stabilization to ensure efficient excitation. Frequency stabilization of both the 480 nm lasers is achieved using the Pound–Drever–Hall (PDH) locking technique [117, 118]. The laser is referenced to an ultra stable, high finesse cavity with a Free Spectral Range (FSR) of 1.5 GHz and a finesse of 100,000. The cavity is constructed from Ultra Low Expansion (ULE) glass, ensuring minimal thermal drift and high long term stability.

The PDH locking scheme involves generating sidebands at $\pm$200 MHz using a tunable RF source. These sidebands are used to create an error signal, which is fed back to the laser to stabilize its frequency. The error signal is derived from the reflection of the laser light off the cavity, with the sidebands providing a reference for the lock point. This setup allows for precise tuning of the laser frequency across the FSR of the cavity, enabling the system to address various Rydberg states with high accuracy.

Using the locking scheme in Figure 3.3 we can separate the light from each laser by setting them to orthogonal linear polarisations. This allows us to lock the two

lasers to the same ULE cavity.

3.3 Ultra-High Vacuum Chamber

A robust and well designed vacuum system is fundamental to the operation of any cold atom experiment. It provides the low pressure environment ($\geq 10^{-10}$ Torr) required for long atomic lifetimes and minimal collisional decoherence, while offering optical and electrical access for trapping, manipulation and detection. The apparatus used here comprises two connected regions: a glass 2D MOT cell that produces a continuous cold atomic beam, and a stainless steel science chamber where atoms are captured, cooled and interrogated. These chambers are linked by a differential pumping stage that maintains a pressure gradient of over three orders of magnitude, ensuring that the science region remains in the UHV regime. The following sections describe the design and functionality of each component in detail.

3.3.1 2D MOT Cell

The 2D MOT chamber is connected to the main science chamber through a four way cross and a differential pumping tube with an aperture of 0.8 mm. The differential pumping tube prevents the build up of pressure in the main chamber, which maintains a pressures bellow 1×10^{-10} Torr. This ensures that the 3D MOT operates under optimal conditions for trapping and cooling.

The 2D MOT cell is a UHV glass cell with internal dimensions of $25 \times 25 \times 100$ mm. The cell contains two Rubidium dispensers (Alvatec AS-3-Rb-250-F) that maintain a high vapour pressure, allowing for efficient loading of atoms into the trap. The 2D MOT traps and cools atoms in two dimensions across four (latterly three, see Chapter 5) cooling volumes, creating an narrow high density atomic beam [119, 120].

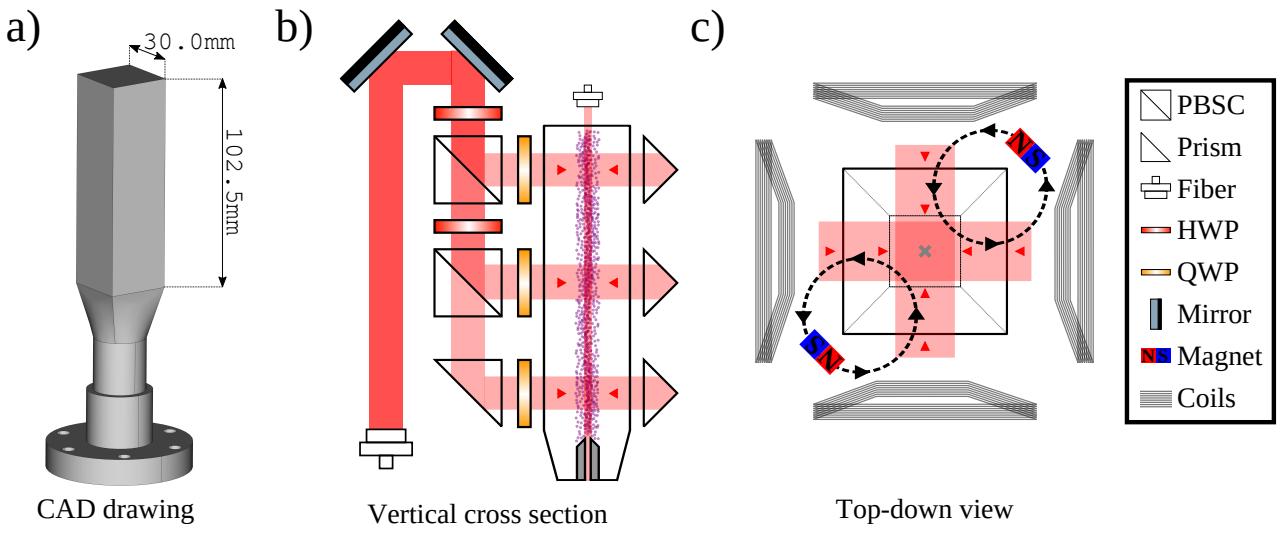

Figure 3.4: **a)** Isometric view of the 2D MOT vacuum cell, a rectangular Pyrex cell (25 mm × 25 mm × 100 mm). **b)** Vertical cross-sectional view showing the paths of the red-detuned cooling beams (red shading) and the axial pushing beam used to direct atoms towards the science chamber. The dense atomic beam is represented by the purple dots. The fibre-coupled input and internal optics are arranged to deliver collimated, circularly polarised beams that intersect at the trapping region. **c)** Top-down view of the 2D MOT cell showing the configuration of the cooling beams in the horizontal plane, along with the magnetic field lines (dotted black) produced by permanent magnets. The magnetic field zero point is marked with a grey cross, corresponding to the centre of the quadrupole field. External compensation coils are mounted around the cell and enable fine adjustment of the magnetic field profile. This configuration enables efficient 2D confinement of Rubidium atoms and a pre-cooled dense atomic beam through the differential pumping tube.

3.3.2 Science Chamber

A stable ultra-high vacuum (UHV) environment is essential for the preparation and manipulation of cold atomic ensembles. Collisions with background gas atoms limit both the trap lifetime and the coherence of Rydberg excitations, making pressures below 10^{-9} Torr critical for achieving long interrogation times and high optical depth [15, 25, 55]. The vacuum assembly used in this work was originally developed by Hannes Busche, Simon Ball and Paul Huillery [112, 113] and has since been adapted and upgraded to support the present experiment. It provides both the low pressure environment required for magneto-optical trapping and the optical

access necessary for high resolution imaging and precise field control. The system consists of two main regions: a glass 2D MOT cell (Section 3.3.1, which generates a continuous cold atomic beam, and a stainless steel science chamber (Section 3.3.2, where atoms are captured, cooled, and interrogated. These are connected via a differential pumping stage that maintains a pressure gradient of more than three orders of magnitude between the source and science regions. Together, these elements form a compact and stable vacuum system optimised for experiments in cold atom and Rydberg physics.

The science chamber * forms the central region of the experiment, where atoms are transferred following initial pre-cooling in the 2D MOT stage. It consists of a compact, stainless steel octagonal cell designed to provide both good optical access and the necessary infrastructure for electric and microwave field generation.

The chamber features eight optical ports arranged in the vertical plane and two more horizontally and perpendicular to the vertical plane. This gives the optical access required for the cooling, trapping, dressing and diagnostics of the ensemble. All viewports are Anti-Reflection (AR) coated windows optimised for 780 nm and 480 nm operation, ensuring high transmission while minimising heating and reflections. The chamber is mounted on a rigid stainless steel mount bolted to the optical bench. All attached field control elements (such as electrodes and antennas) are fixed in a stable configuration to preserve alignment through thermal cycling and experimental runtime.

This layout offers a balance between compactness and accessibility, enabling integration with high resolution imaging systems and single photon counting apparatus.

3.3.2.1 Compensation Coils

To achieve precise control over the magnetic environment within the science chamber, a set of compensation coils are used to cancel the Earth's magnetic field and

*Kimball Physics MCF600-SphOct-F2C8

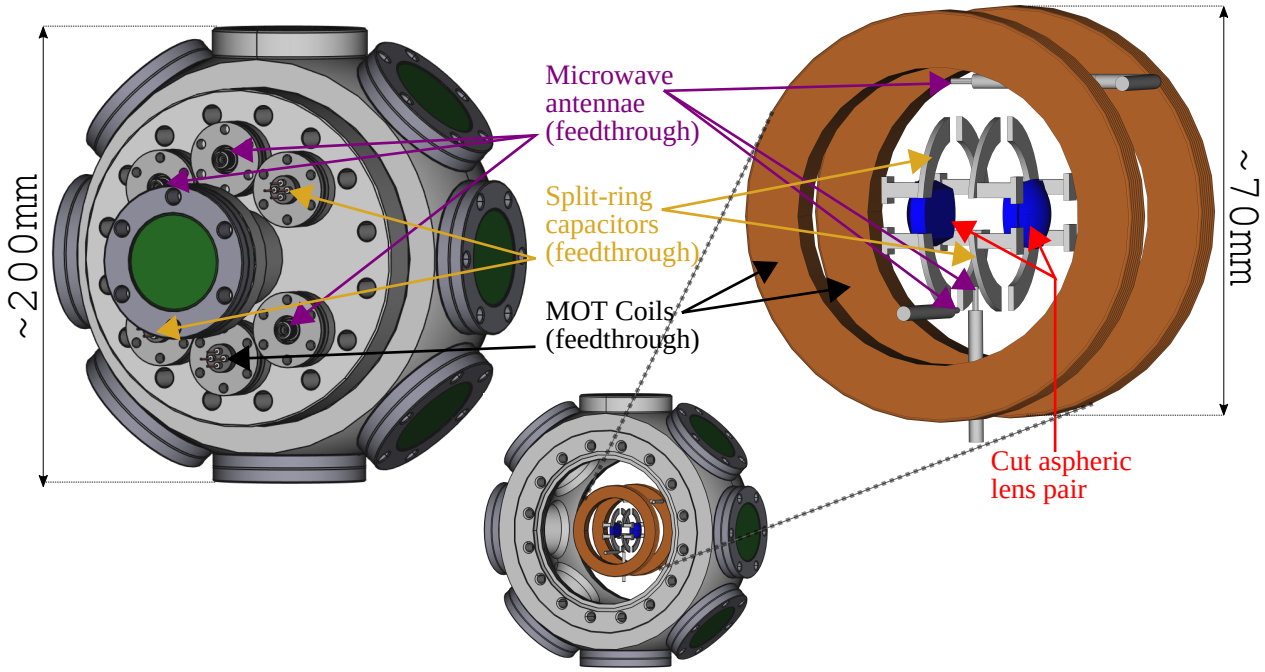

Figure 3.5: Overview of the science chamber assembly and in-vacuo components. **Right:** CAD rendering (adapted from an initially rendered model by Hannes Busche [110]) the full science chamber showing vacuum viewports and the positions of AR coated windows (green shading) used for optical access along horizontal and vertical axes. Electrical feedthroughs for in-vacuo components including microwave antennas, MOT coils and electrodes are indicated. **Left:** Expanded view highlighting the key in-vacuo elements. The MOT coils (black arrows) are in an anti-Helmholtz configuration to generate a quadrupole magnetic field. A high NA = 0.5, ITO coated aspheric lens pair (red arrows) is mounted along the vertical axis to focus trapping, probing and coupling beams at the ensemble centre. Eight split-ring electrodes (yellow arrows) surround the trap region to enable static electric field control. Three orthogonal microwave antennas (purple arrows) allow polarisation controlled microwave driving of Rydberg–Rydberg transitions. The layout enables high resolution optical access, precise field control and mechanical stability required for cold atom and Rydberg physics experiments.

residual magnetic fields, to ensure that the zero point of the 3D MOT's quadrupole is at the focal point of the aspheric lenses. These corrections minimise field gradients that can shift energy levels, or induce decoherence during the experimental sequences.

The compensation system consists of three orthogonal pairs of coils arranged in a pseudo-Helmholtz rectangular configuration, corresponding to the x, y and z

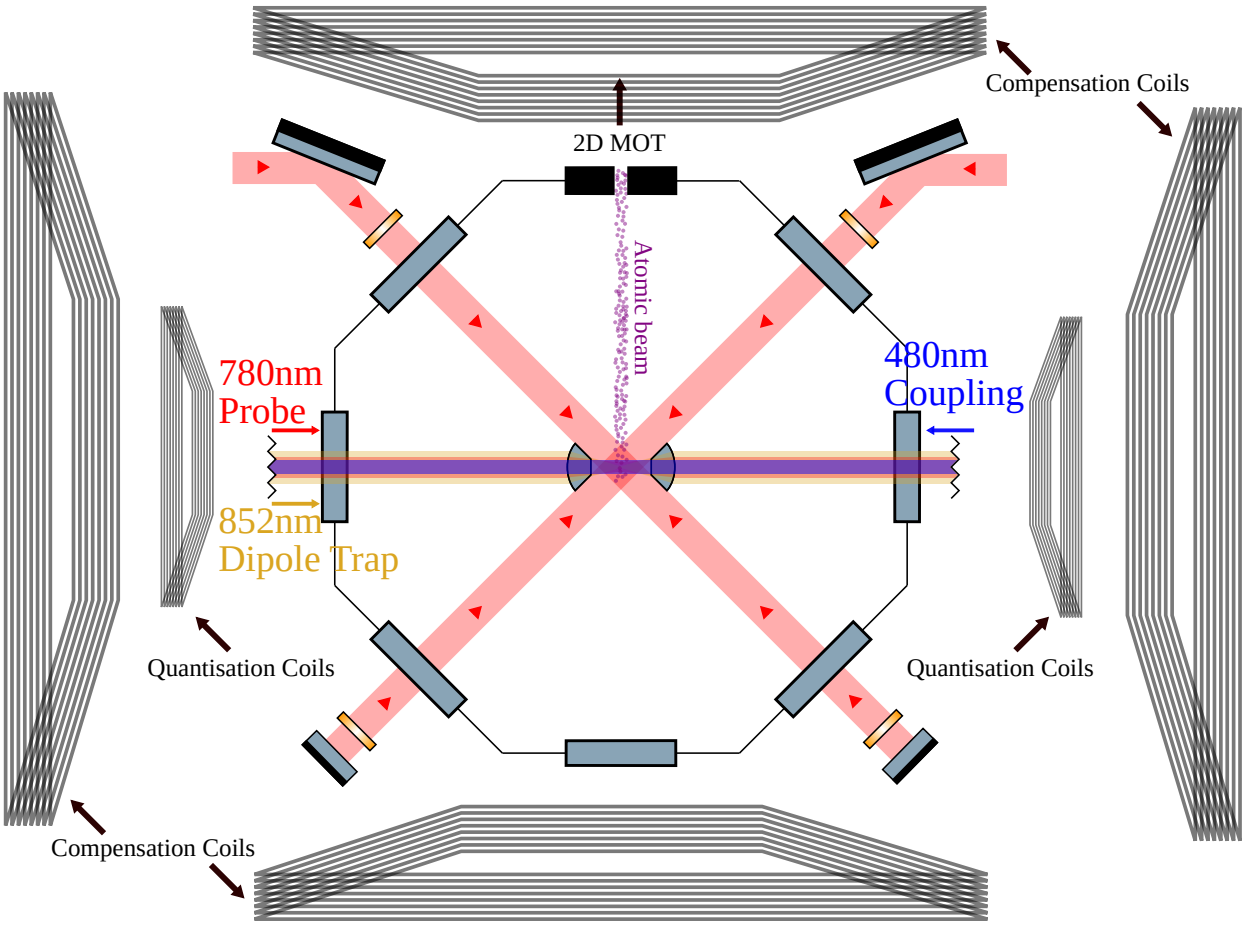

Figure 3.6: Vertical cross section diagram of the main optical and magnetic field components around the science chamber. Four key laser beams are shown converging at the trapping region: the diagonal MOT beams, the 780 nm probe beam, the 852 nm dipole trapping beam and the 480 nm Rydberg coupling beam. These beams are aligned through the high numerical aperture in-vacuo lens pair to ensure spatial overlap at the trap centre. The incoming atomic beam from the 2D MOT enters the chamber from the top and is captured by the 3D MOT at the chamber centre. External compensation coils generate uniform DC magnetic fields to cancel residual stray fields and position the quadrupole zero of the MOT at the lens focus. Quantisation coils generate a magnetic field along the horizontal axis sequences, establishing a defined quantisation axis.

axes of the chamber. Each coil pair is mounted externally to the vacuum system, with their centres aligned to coincide with the trap region. The geometry and winding of the coils are chosen to produce uniform magnetic fields over the extent of the atomic cloud. Currents are supplied via low noise, high stability, digitally

controlled current sources (Agilent 6632B).

3.3.2.2 In-vacuo Lenses

To confine atoms in a smaller volume and at temperatures below those achievable via magneto-optical trapping alone, we use a FORT operating at 852nm. The trap is formed at the focal point of pair of aspheric high NA = 0.5 in-vacuo lenses. The separation of the lenses is 14 mm, twice their working distance. Using a knife edge measurement on a copy of the lens the waist has previously been measured to be $w_0 = 4.5 \pm 0.3$ μm, although has since been measured to be $w_0 = 3.8 \pm 0.1\mu$m on a 4f imaging setup.

Due to the wavelength dependent focal shift introduced by the aspheric lenses, careful collimation of the FORT beams is necessary to ensure overlap with the focal planes of both the probe and Rydberg excitation beams. This is achieved using a pair of lenses at the fibre output. The overlap is verified by measuring the beam profile using our 4f imaging setup (see Section 3.8).

3.3.2.3 Microwave Antennas

Microwave radiation for driving Rydberg state to Rydberg state transitions is applied using three $\lambda/4$ antennas (centred at 18.5 GHz), one for each cardinal direction. A combination of the three antennas can achieve microwave fields with an arbitrary polarisation. Microwave signals are delivered through SMA vacuum feedthroughs and can be driven in either pulsed or continuous wave mode. The system allows for stable and spacially homogenous microwave fields over the trapping volume, enabling precise state manipulation.

3.3.2.4 Split Ring Electrodes

To apply controlled DC electric fields to the trapped atoms, the chamber includes a pair of split-ring electrodes designed to deliver a homogeneous field across the

trapping volume [112, 121], ensuring the uniformity required for accurate Stark-shift tuning and state-dependent control of Rydberg levels.

Each electrode is a quarter-circle titanium arc mounted coaxially with the probe, coupling, and dipole-trapping beams around the centre of the chamber, with a separation of approximately 10 mm. The electrodes are connected to external high-voltage supplies via UHV feedthroughs, allowing both static and time varying fields to be applied.

3.4 Experimental Control

The experimental apparatus is controlled using the Durham Experimental Terminal (DExTer), a modular LabView based interface developed for cold atom amd molecule experiments at Durham University. Originally designed by T. Wiles [122], DExTer was created to provide a general purpose control system for a range of experiments. Over the lifetime of this experiment it has been continually developed and adapted to meet its specific needs [113].

DExTer structures experiments into discrete timesteps of user defined length, controlling digital and analogue outputs to manage hardware components. As alluded to earlier, in this experiment digital outputs switch AOMs, quantisation coils and diagnostic triggers. Analogue outputs modulate AOM frequencies and amplitudes, as well as the 3D MOT and compensation coil currents. To meet the timing demands of nanosecond scale Rydberg experiments, DExTer can support fast digital outputs with a resolution of 5ns.

Control is executed via a National Instruments PCIe-7842R Field Programmable Gate Array (FPGA), providing 96 digital I/O channels and 8 analogue channels. The FPGA operates with a 40 MHz base clock (25 ns period), but overclocked to 200 MHz during our sub-microsecond sequences to improve the precision and determinism of synchronised outputs. This architecture enables reliable

sub-microsecond pulse generation and a practical timing resolution of 5 ns for the fast digital outputs used in Rydberg-excitation sequences.

Photon detection via Single-Photon Avalanche Detector (SPAD) arrays is implemented in the FPGA and is capable of real time photon counting with 5ns resolution. This control infrastructure allows for automation and high rates of experimental repetition to gather the large volume of results to produce the statistics required for this type of experiment.

3.5 Ensemble Preparation

3.5.1 2D MOT

The 2D MOT provides the first stage of cooling for ^{87}Rb atoms before they are transferred to the 3D MOT. The 2D MOT is designed to operate under UHV conditions, ensuring minimal background collisions and efficient cooling of the atomic ensemble. The conditions for the 2D MOT to function are achieved in the following ways:

- **Light**: The cooling and repump light is split evenly between the three channels using HWP and PBSC pairs. Each beam then passes through a Quarter-Waveplate (QWP) to obtain the required circular polarisation and is retro reflected by a total internal reflection prism to provide an equal and opposite light force. In a MOT, the counter propagating beams must have opposite circular polarisations (σ^+ and σ^-). The sequence of internal reflections within the prism reverses the handedness of the returning beam, thereby providing the correct σ^+/σ^- configuration without requiring additional QWPs.
- **Magnetic field**: The quadrupole magnetic field is generated by two sets of permanent neodymium magnets. Adjustments to the zero point of the

field can be made by a two pairs of coils in a pseudo-Helmholtz configuration (Figure 3.4c).

- **Pushing Beam**: A red detuned "pushing" beam is used to enhance the atomic flux by selectively addressing atoms with upwards momentum away from the science chamber and "pushes" them towards it [119, 120]. The pushing beam is aligned coaxialy with the atomic beam. This setup ensures efficient transfer of atoms from the 2D MOT to the 3D MOT.

3.5.2 3D MOT

The 3D MOT serves as the primary trapping and cooling stage, creating a dense and cold atomic ensemble for further confinement in the dipole trap. The 3D MOT is designed to operate under UHV conditions, ensuring minimal background collisions and efficient cooling of the atomic ensemble. The 3D MOT consists of three retroreflected cooling beams aligned with a magnetic quadrupole field produced by in-vacuo coils in the anti-Helmholtz configuration. The 3D MOT is fed atoms from the 2D MOT, the dense atomic beam falling under gravity and aided by the pushing beam through the differential pumping tube and traps them in all three spatial dimensions, cooling them to temperatures of approximately 100 μK.

The 3D MOT is integrated into the experimental setup as follows:

- **Cooling Beams**: The cooling mechanism in the 3D MOT relies on the scattering of photons from the cooling beams, which are 12 MHz red detuned from the $|5S_{1/2}, F = 2\rangle \rightarrow |5P_{3/2}, F = 3\rangle$ transition. The cooling beams are derived from the 780 nm cooling laser system (see Section 3.2.1) and are delivered to the experiment via optical fibres. The cooling beams are split into three axes and passed through QWPs to give them either σ^+ or σ^- polarisation depending on the direction of the magnetic field along the axis

which they are propagating. Once passing through the vacuum chamber the beams are passed again through QWPs to reverse the handedness of their polarisation and provide the light force in the opposite direction.

- **Repump Beam**: The 3D MOT also includes a repump beam, which addresses the $|5S_{1/2}, F = 1\rangle \rightarrow |5P_{3/2}, F = 2\rangle$ transition. The repump beam ensures that atoms are efficiently pumped back into the $|5S_{1/2}, F = 2\rangle$ state, maintaining the cycling transition required for efficient cooling and trapping. This light is only included in one of the three axes of the 3D MOT.

- **Magnetic Quadrupole**: The magnetic quadrupole is produced by in-vacuo coils and is aligned with the cooling beams to create the trapping potential. The pair of copper wire MOT coils have a square cross section and have been wound 56 times each in a 8×7 grid pattern [112, 113]. They are positioned in the Helmholtz configuration such that the $B = 0$ point of the quadrupole produced is at the focal point of the in-vacuo high NA lenses. The $B = 0$ point of the quadrupole can be adjusted to the desired position via a set of three pairs (one for each axis) of external compensation coils, allowing for precise control over the trapping volume. These coils are rectangular and have a pseudo-Helmholtz configuration. The method for establishing the optimum currents for the compensation coils is described in Section 6.2.1-6.2.2.

3.5.3 Dipole Trap Loading

Efficient loading of the dipole trap is achieved through a multi stage cooling sequence designed to maximise atom number and density. Each stage contributes to the gradual reduction in temperature and the removal of untrapped atoms. The full sequence proceeds as follows:

- **3D MOT loading (100-500 ms):** Atoms are pre-cooled in a standard magneto-optical trap with high cooling and repump powers. A flux of cold atoms from the 2D MOT ensures rapid loading.

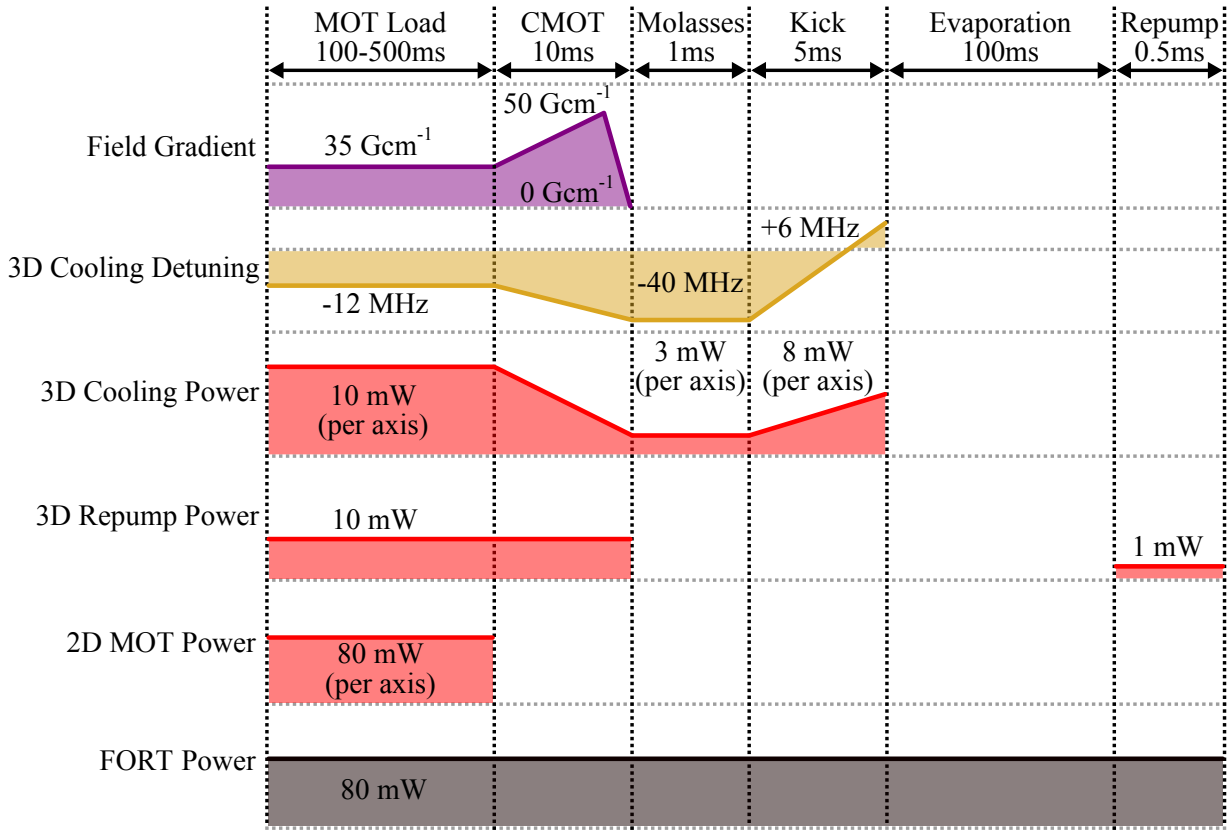

Figure 3.7: Timing diagram for dipole trap loading sequence. The sequence begins with a 3D MOT loading phase (100–500 ms), followed by a CMOT (10 ms), optical molasses (1 ms) and kick stage (5 ms) to remove untrapped atoms. After dipole trap loading, free evaporation (100 ms) is used to reduce ensemble temperature, followed by a short repump pulse (0.5 ms) to prepare atoms in the desired hyperfine ground state. The figure shows the evolution of key experimental parameters during the sequence. Exact detunings and intensities are indicated. This sequence produces a cold, dense ensemble suitable for Rydberg excitation.

- **Compressed Magneto-Optical Trap (CMOT) (2 ms):** The MOT magnetic field gradient is ramped up, the cooling and repump laser powers are ramped down and the cooling beam detuning is increased to $\sim 5\Gamma$. This reduces the trapping volume, compresses the cloud and increases the atomic density.

- **Optical Molasses (2 ms):** The magnetic field gradient and repump light are

switched off, while the cooling detuning and power are held constant, reducing the ensemble temperature to $\mathcal{O}(10\ \mu K)$ whilst also optically pumping atoms into the $|F = 1\rangle$ ground state.

- **MOT Ejection (5 ms):** The cooling beams are ramped from red to blue detuning, giving momentum to untrapped atoms, removing them from the FORT trapping volume, cleaning the trap region. Only atoms confined in the dipole trap potential remain, since their energy levels have been AC Stark shifted such that then are not resonant with the beams.

- **Evaporative Cooling (50 ms):** A short period of free evaporation in the FORT allows high energy atoms to escape, resulting in further reduction in temperature.

- **Repumping (500 μs):** A short repump pulse transfers atoms from the $|F = 1\rangle$ to the $|F = 2\rangle$ hyperfine ground state, preparing the ensemble for state preparation and Rydberg excitation.

- **Quantisation Field:** A quantisation coil is switched on to lift the degeneracy of the Zeeman sublevels, establishing a well defined quantisation axis for subsequent optical excitation sequences, all of which are in the same direction as the field.

This procedure produces an optically dense, ultracold atomic ensemble suitable for experiments in quantum nonlinear optics and coherent light-matter interactions. The sequence is optimised to balance speed, atom number and final temperature, with high repetition rates in the $\mathcal{O}(10\ kHz)$ under typical operating conditions.

3.6 Optical Addressing of the Ensemble

Low photon number probe light at 780 nm, addressing the $|5S_{1/2}, F = 3\rangle \rightarrow |5P_{3/2}, F' = 4\rangle$ transition, is focused by the same aspheric lens system making the dipole trap to

a waist of $w_p = 1.5$ μm. This probe excites atoms from the ground state, the first transition in our two step transition to the Rydberg state.

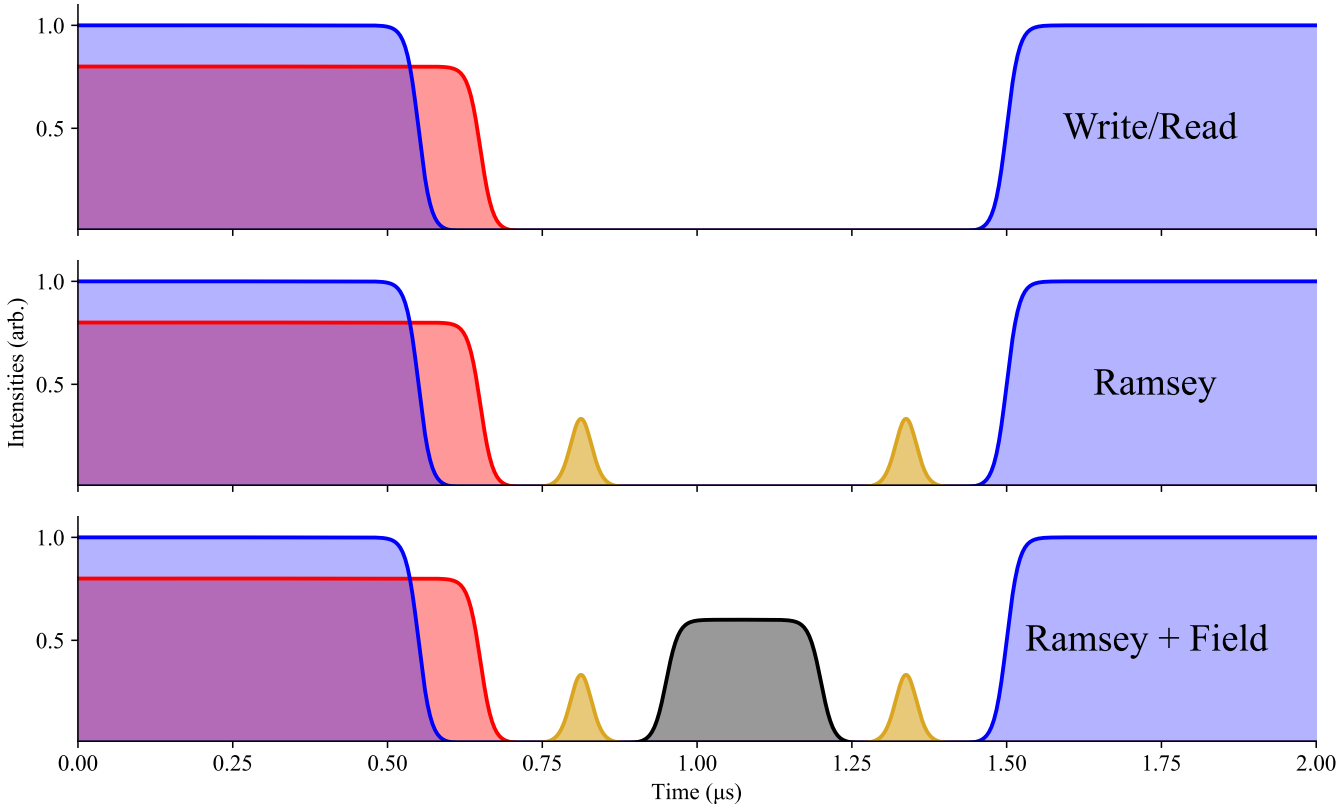

Figure 3.8: Typical optical sequences to address the atomic ensemble. Each row shows a different protocol executed within a single experimental shot. Red pulses indicate 780 nm probe light, blue pulses correspond to 480 nm coupling light for Rydberg excitation, yellow pulses represent applied microwave fields and grey pulses indicate applied electric, magnetic or second microwave fields. **Top:** A standard EIT write/read sequence, where simultaneous probe and coupling pulses excite atoms to a Rydberg state. The second (blue) pulse returns the population to the intermediate $5P_{3/2}$ state via stimulated emission, followed by spontaneous decay to the ground state. **Middle:** Ramsey interferometry sequence with two short probe coupling pulses separated by a dark interval, during which free evolution occurs. **Bottom:** Ramsey sequence with an applied field during the dark interval, demonstrating the ability to measure such a field. The SPAD detection window opens at the start of the second coupling pulse, capturing spontaneous emission photons corresponding to the $nS_{1/2}$ state population.

The coupling field, addressing the $5P_{3/2} \rightarrow nS_{1/2}$ Rydberg transition, is counter-propagating and collimated to a waist of $w_c \approx 25$ μm at the ensemble position. This configuration ensures a uniform Rabi frequency Ω_c across the ensemble. Precise

collimation compensates for wavelength dependent focal shifts, aligning the probe and coupling beams in a common focal plane. Typically an optical depth of OD = 4 is achieved (see Section 6.3).

3.7 Single-Photon Detection

Signal photons transmitted through the atomic ensemble are detected using four fibre-coupled SPADss (Excelitas SPCM-780- 14-FC), arranged in a dual channel HBT configuration, described in Section 2.4.2 and Figure 3.9. Each optical channel is monitored by a pair of SPADs, allowing measurement of photon statistics and detection of photon correlations.

Before fibre coupling, a stack of interference filters centred at 780 nm suppresses stray light from the dipole traps, coupling beams and other sources of unwanted scattering. The overall detection efficiency exceeds 20%, limited primarily by the quantum efficiency of the SPADs (approximately 60%) and losses in the collection optics and fibre coupling.

Each SPAD generates a TTL pulse upon photon detection, which is time tagged with 5ns resolution. This enables recording of individual photon arrival times, facilitating detailed analysis of photon counting statistics.

Extensive measures are taken to suppress detection noise; SPADs are contained in a light tight box, the whole optical bench is in an enclosure and fibre coupling of the SPADs all contribute to this end. Electronic dark counts and residual optical noise are characterised and corrected for in data analysis, each dataset is started with a new reference. The detection system enables reliable observation of single photons and photon correlations essential for quantum optics experiments.

3.8 Imaging

Accurate characterisation of ultracold atomic ensembles is essential for optimising experimental parameters and interpreting results. In this work, two complementary imaging techniques are employed: absorption imaging to obtain quantitative information on atom number, density and temperature, and fluorescence imaging for qualitative diagnostics and alignment.

3.8.1 Absorption Imaging

Absorption imaging is used to determine the spatial density distribution of atoms by measuring the attenuation of resonant probe light. The transmitted intensity $I(x, y)$ is related to the incident intensity $I_0(x, y)$ and the column density $n_{\mathrm{col}}(x, y)$ via the Beer–Lambert law:

$$I(x, y) = I_0(x, y)\, e^{-n_{\mathrm{col}}(x,y)\sigma_0}, \tag{3.1}$$

where $\sigma_0 = \frac{3\lambda^2}{2\pi}$ is the resonant scattering cross-section for the D_2 transition.

The column density represents the number of atoms per unit area along the probe beam direction and is obtained by integrating the three dimensional density over the imaging axis,

$$n_{\mathrm{col}}(x, y) = \int n_{\mathrm{3D}}(x, y, z)\, \mathrm{d}z. \tag{3.2}$$

Two images are recorded: one with the atomic ensemble present and a reference image without atoms. The ratio of the transmitted to incident intensity defines the local optical depth,

$$\mathrm{OD}(x, y) = -\ln\left(\frac{I(x, y)}{I_0(x, y)}\right), \tag{3.3}$$

which is directly proportional to the column density via $\mathrm{OD}(x, y) = n_{\mathrm{col}}(x, y)\,\sigma_0$. Hence,

$$n_{\mathrm{col}}(x, y) = -\frac{1}{\sigma_0} \ln\left(\frac{I(x, y)}{I_0(x, y)}\right). \tag{3.4}$$

The imaging system is a $4f$ relay with focal lengths $f = 1000$ mm and $f = 400$ mm, providing a $2.5\times$ magnification that matches the field of view of the Charge Coupled Device (CCD) to the ensemble size. A resonant probe beam derived from the 780 nm cooling laser system is used. The beam has a diameter of approximately 10 mm and passes horizontally through the vacuum chamber, overlapping but slightly misaligned with the axial MOT beams while maintaining orthogonal polarisation. After passing through the chamber, the probe and MOT beams are separated by a PBSC; this, combined with the small misalignment, ensures that only probe light reaches the CCD.

The image is captured on an Andor Luca CCD camera with 10 μm pixels. Optical noise from stray light and interference fringes is mitigated using narrowband interference filters and post-processing with Fourier filtering techniques.

Absorption imaging provides reliable measurements of cloud position, size, and temperature. Time-of-Flight (TOF) measurements, where the ensemble expands freely after release from the trap and images are taken after different expansion times, allow the determination of temperature. Cloud sizes are extracted by fitting Gaussian profiles to the density distributions at various expansion times.

3.8.2 Fluorescence Imaging

Fluorescence imaging is employed for qualitative diagnostics, particularly for aligning the optical traps and monitoring ensemble positions. Due to optical access constraints, imaging is performed along the axis of the in-vacuo aspheric lenses. A two inch flip mirror enables switching between fluorescence imaging and photon detection modes without realignment.

The fluorescence light emitted by atoms illuminated by the MOT beams is collected by the same in-vacuo lenses used for trapping and probing. A telescope consisting of a 10.3 mm aspheric lens and a 400 mm lens images the fluorescence onto an Andor iXon Electron Multiplying Charge Coupled Device (EMCCD) camera, achieving a magnification of 40×.

While fluorescence imaging provides limited quantitative information due to depth of field constraints, it serves as a critical alignment tool. The high NA (NA = 0.5) of the in-vacuo lenses yields a shallow focal depth of approximately DOF $\approx 2\lambda/\mathrm{NA}^2 \simeq$ 6 μm at $\lambda = 780$ nm, meaning that only atoms within a few micrometres of the trap centre are sharply resolved. For comparison, the axial extent of the dipole-trapped ensemble is of order $\mathcal{O}(10\ \mu\mathrm{m})$, while the 3D MOT cloud extends to $\mathcal{O}(1\ \mathrm{mm})$, so only a small fraction of either ensemble lies within the $\sim 6\ \mu$m focal depth at any one time. Fluorescence from atoms outside this region appears blurred, reducing image contrast.

Despite this, the method is invaluable for rapid visual diagnostics, and was also used to measure the size, quality, and focal alignment of both the dipole-trap and probe beams. By imaging the spatial profiles of these beams at the focus, adjustments could be made to optimise beam quality, minimise aberrations, and ensure proper overlap with the atomic ensembles. Examples of absorption and fluorescence images can be seen in Figures 6.4 and 6.9, respectively.

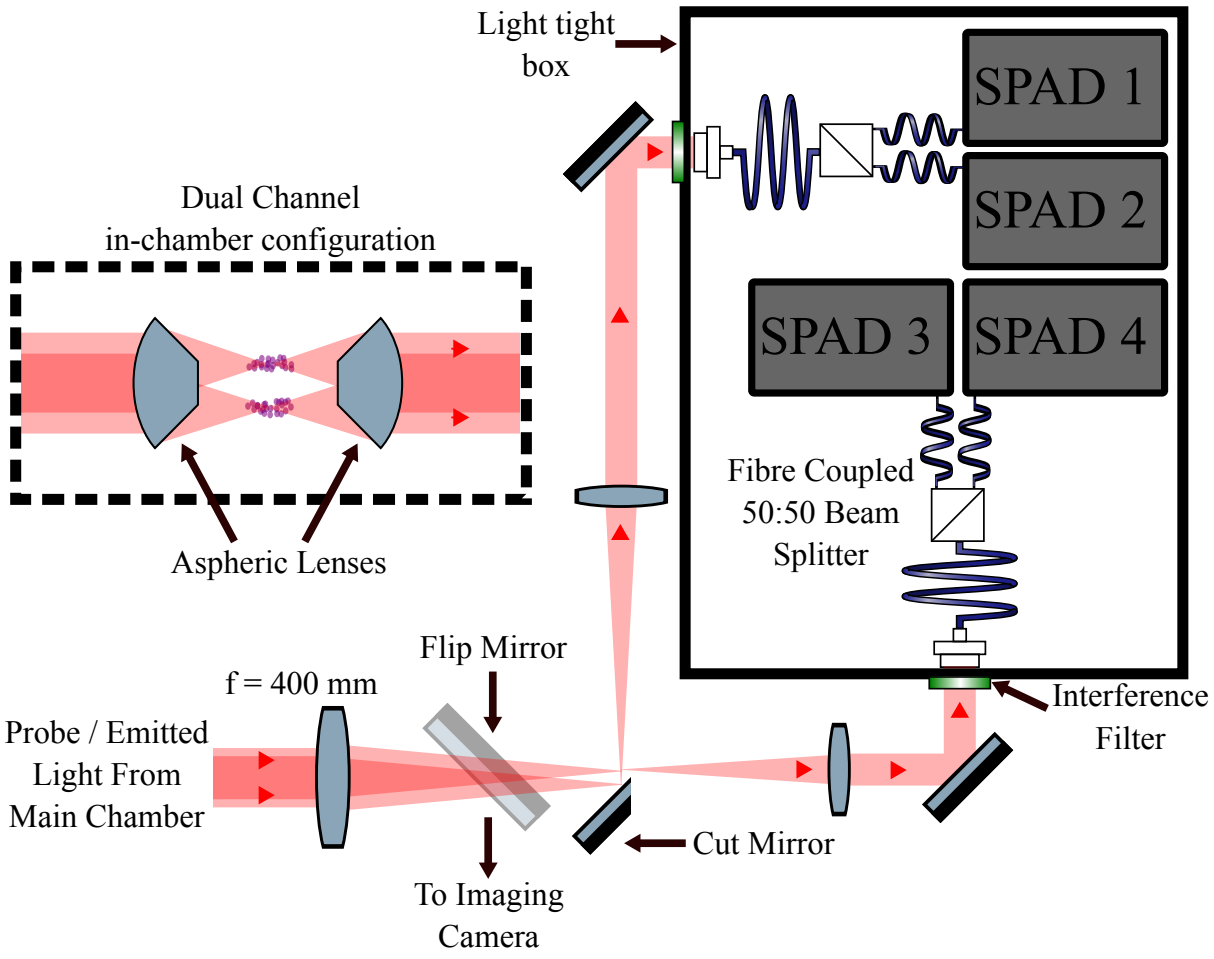

Figure 3.9: Schematic of the Hanbury Brown–Twiss (HBT) detection system used for photon correlation measurements. Fluorescence or transmitted light from the main chamber is collected and collimated using an $f = 400$ mm lens. A flip mirror allows the light to be directed either to the imaging camera or toward the single-photon detectors. A cut mirror separates the two channels. After interference filtering at 780 nm, the signal is fibre coupled into a light tight box containing a 50:50 fibre beam splitters and four SPAD detectors (two per optical channel). Each detection event is time-stamped with 5 ns resolution for analysis. The dashed box shows the optional in-chamber configuration for the two-channel detection setup, which includes the pair of aspheric collection lenses cut at an angle to provide clearance for the MOT beams (See Figure 3.6) while preserving the required NA. This configuration was developed for dual-channel operation but was not implemented in this work.

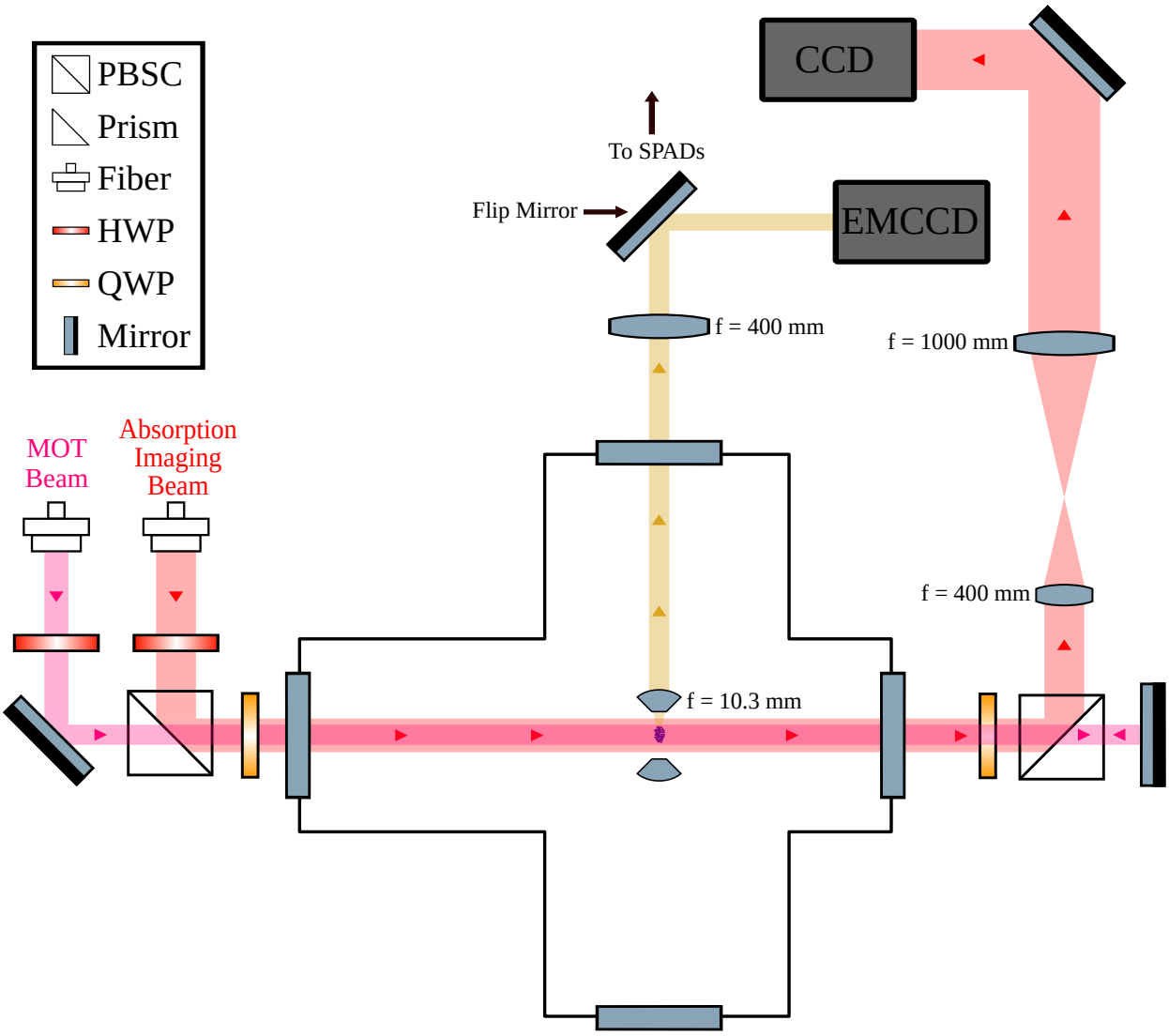

Figure 3.10: Optical setup for both absorption and fluorescence imaging of the atomic ensemble. **Absorption imaging (horizontal path):** A resonant probe beam derived from the 780 nm cooling laser is directed horizontally through the atomic cloud and separated from the MOT beams using a PBSC. The transmitted light is imaged onto a CCD camera using a 4f telescope comprising lenses with focal lengths of 1000 mm and 400 mm, resulting in a magnification of 2.5×. **Fluorescence imaging (vertical path):** Fluorescence from atoms excited by the MOT beams is collected along the vertical axis through the in-vacuo high NA (f = 10.3 mm) aspheric lens. The light is reimaged by a second 4f system using the in-vacuo and a 400 mm lens onto an EMCCD camera, giving a total magnification of 40×. A flip mirror allows switching between the fluorescence imaging path and the fibre-coupled SPADs used for photon counting. This dual imaging setup allows for quantitative measurements as well as diagnostics for beam alignment and ensemble positioning.

Chapter 4

Results

4.1 Overview

This chapter presents experimental results demonstrating the preparation, coherent control and characterisation of a single photonic *qutrit* encoded in a cold ensemble of ^{87}Rb atoms. These results build directly on previous work [1, 2] in which collective Rydberg qubits were created and manipulated using the experimental setup described in Chapter 3. By extending the accessible Hilbert space from two to three dimensions, the experiments reported here enable richer quantum dynamics, including multilevel coherence and interference and pave the way for exploring higher dimensional quantum information protocols [123, 124, 125, 126, 127, 128].

The results presented here precede the overhaul of the experiment described in Chapter 5, but operate on the same principles. A dense, cold ensemble was loaded into an optical dipole trap and coupled to a Rydberg state via a ladder type two photon excitation. The current work extends this platform to implement a qutrit encoded in a single collective Rydberg excitation and demonstrates its coherent control using two independent microwave transitions [3].

It is motivated both by the potential of higher dimensional quantum systems for QIP and by recent theoretical work on qutrit visualisation and dynamics [129]. The results are presented in the context of a draft publication [3] and include new exper-

imental data on qutrit population dynamics, coherence via Ramsey interferometry and photon correlation statistics.

This chapter is based on the following pre-print publication and the data was taken jointly with Yuechun Jiao:

Yuechun Jiao, Oliver D. W. Hughes, Max Z. Festenstein, Zhengyang Bai, Jianming Zhao, Weibin Li, Kevin J. Weatherill, and C. Stuart Adams. Single photonic qutrit in a collective Rydberg polariton, Sep 2025. URL `https://link.aps.org/doi/10.1103/3xnw-cpj2`

4.2 Photon Storage and Retrieval

The scheme used to prepare the polariton consists of the ^{87}Rb states $|g\rangle = |5S_{1/2}, F = 2\rangle$, $|e\rangle = |5P_{3/2}, F = 3\rangle$ and $|r_1\rangle = |nS_{1/2}\rangle$. A weak 780 nm probe laser addresses the $|g\rangle \leftrightarrow |e\rangle$ transition, while a strong 480 nm control beam couples $|e\rangle \leftrightarrow |r_1\rangle$. Together, these form a ladder EIT scheme through which a single probe photon may be coherently stored as a Rydberg polariton.

Storage is initiated by turning off the control field during the probe pulse, mapping the optical excitation into a collective Rydberg state. Retrieval is accomplished by reapplying the control beam, converting the polariton back into an optical photon via a two step process. Stimulated emission, $|r_1\rangle \rightarrow |e\rangle$ and then spontaneous emission, $|e\rangle \rightarrow |6\rangle$, which is detected by the SPADs.

With storage and retrieval demonstrated, we now extend the system to encode and manipulate a three-level qutrit.

4.2.1 Photon Statistics After Retrieval

To assess the quantum nature of the light field retrieved from the Rydberg ensemble, we measure the second-order correlation function $g^{(2)}(\tau)$ following storage and retrieval at various principal quantum numbers. This analysis probes the degree

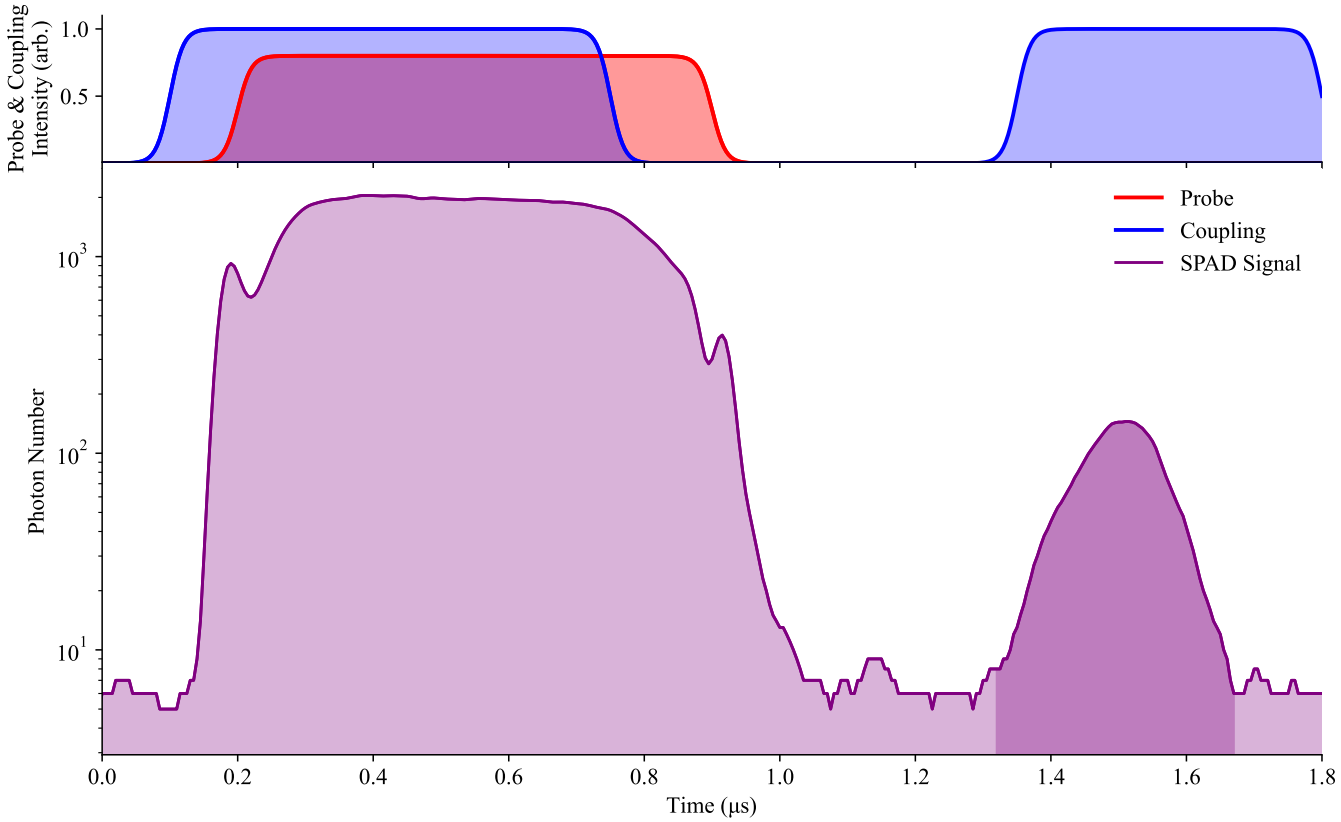

Figure 4.1: Storage and retrieval of a single photon in a Rydberg polariton scheme. **Top:** Normalised time profiles of the coupling (blue) and probe (red) pulses, shown relative to the total experimental sequence. The first control window facilitates storage of a single probe photon as a Rydberg polariton, while the second enables its retrieval via stimulated emission. **Bottom:** Detected signal showing the retrieved photon pulse following reapplication of the control beam, with counts recorded in 5 ns time bins. The trace represents photon-detection events accumulated over many experimental repetitions, corresponding to the retrieval of individual photons rather than simultaneous multiphoton emission. The darker purple shaded region denotes the integrated signal strength.

of photon antibunching and allows us to quantify the extent to which the system behaves as a single photon source.

The correlation function $g^{(2)}(\tau)$ is obtained by comparing photon arrival times on the two SPAD detectors within each retrieval window, producing a histogram of coincidence counts as a function of delay τ (as shown in the inset of Figure 4.2). The central bin at $\tau = 0$ represents simultaneous detections within the same time bin (5 ns), while adjacent bins correspond to events separated by 5 ns time delays.

Within each retrieval event, the photon detection record is discretised into time bins indexed by i, and detections on the two channels are represented by binary variables $A_i, B_i \in 0, 1$ indicating whether a photon arrived within that bin.

Correlations between detections separated by k time bins are then calculated according to:

$$g^{(2)}(k) = \frac{\frac{1}{N_k}\sum_i A_i B_{i+k}}{\left(\frac{1}{N_k}\sum_i A_i\right)\left(\frac{1}{N_k}\sum_i B_{i+k}\right)}, \tag{4.1}$$

where N_k is the number of valid bin pairs at offset k.

The value at $k = 0$ gives $g^{(2)}(0)$, corresponding to coincidences within the same 5 ns time bin, while $|k| \geq 1$ represents correlations between photons separated by longer delays. The resulting histograms are averaged over many retrieval events to improve the signal-to-noise ratio, as illustrated by the delay peaks in the inset of Figure 4.2.

This discrete time bin analysis is equivalent to the definition given in Section 2.4, Equation 2.35, but implemented using the time-tagged photon records from the experiment. Small corrections are applied in software to account for differences in detector count rates.

Figure 4.2 shows measured values of $g^{(2)}(0)$ for a range of Rydberg levels from $50S_{1/2}$ to $90S_{1/2}$. We see decreasing $g^{(2)}(0)$ with increasing n. This is consistent with an enhanced Rydberg blockade effect at higher n (see Section 2.2.2), which prevents the simultaneous excitation of more than one atom within the blockade radius and thus suppresses multi-photon emission.

These measurements provide direct evidence that the stored polariton corresponds to a single collective excitation and that this property is preserved during retrieval. This validates the system as a viable source of single-photon storage and quantum memory operation.

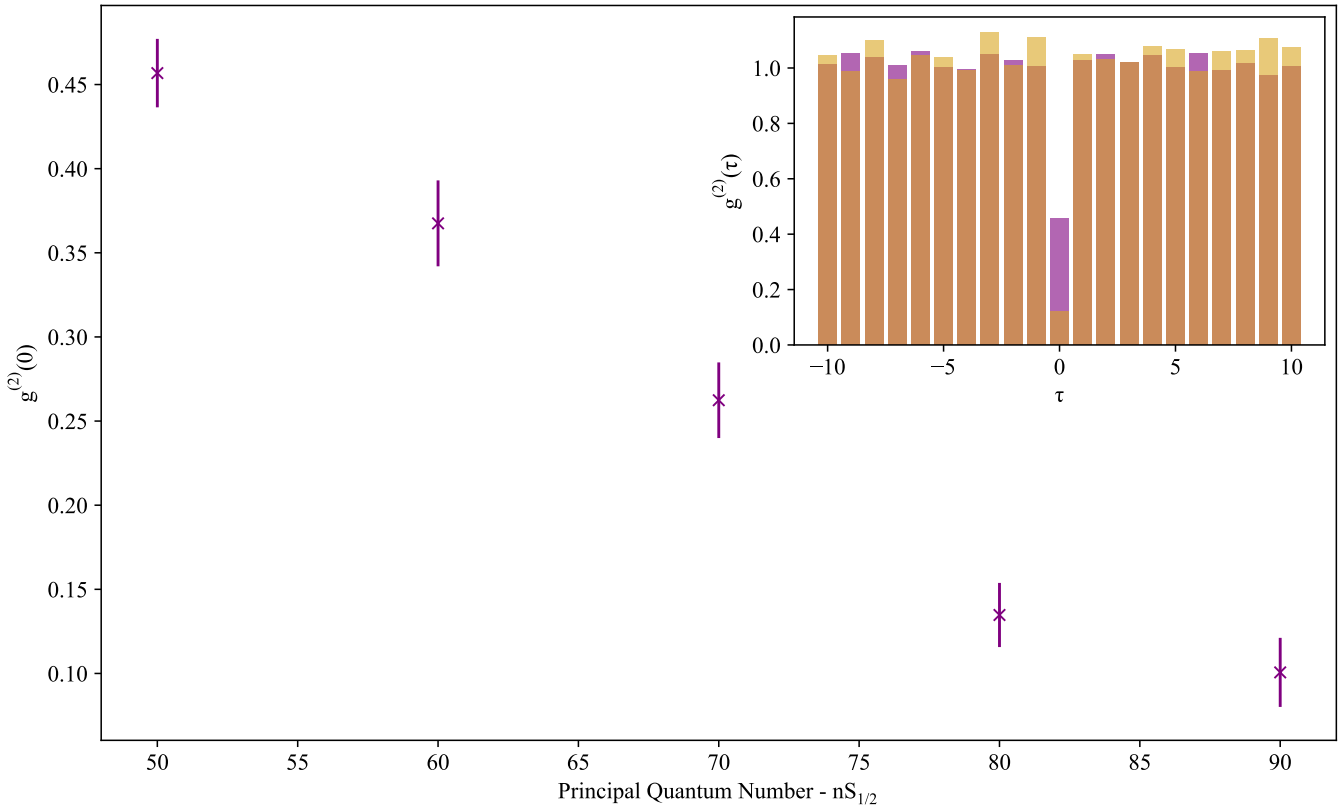

Figure 4.2: Measured second-order correlation at zero delay, $g^{(2)}(0)$, as a function of Rydberg principal quantum number n for the $nS_{1/2}$ series. Each data point is extracted from photon correlation histograms. The inset shows representative $g^{(2)}(\tau)$ histograms for $n = 50$ (purple) and $n = 90$ (yellow). The strong suppression of coincidences at $\tau = 0$ for $n = 90$ reflects enhanced Rydberg blockade, due to a larger blockade radius, compared to $n = 50$.

4.3 Qutrit Population Dynamics

Following the storage of a single optical photon as a Rydberg polariton in the collective state $|r_1\rangle = |60S_{1/2}\rangle$, we implement microwave driven population transfer to prepare and probe a qutrit encoded in three Rydberg states. The qutrit basis states $|r_1\rangle$, $|r_2\rangle$ and $|r_3\rangle$ correspond to $|60S_{1/2}\rangle$, $|59P_{3/2}\rangle$ and $|59S_{1/2}\rangle$, respectively. Coherent transitions between these states are driven by two microwave fields at 18.51 GHz (μ_1) and 18.23 GHz (μ_2), enabling control between these states. Typically we use π and $\pi/2$ pulses, a π pulse corresponds to complete population transfer between the two states, while a $\pi/2$ pulse creates an equal superposition of the two

states. The optical control beam at 479.84 nm couples $|r_1\rangle$ to the intermediate state $|5P_{3/2}\rangle$, allowing the collective excitation to be read out as a single photon.

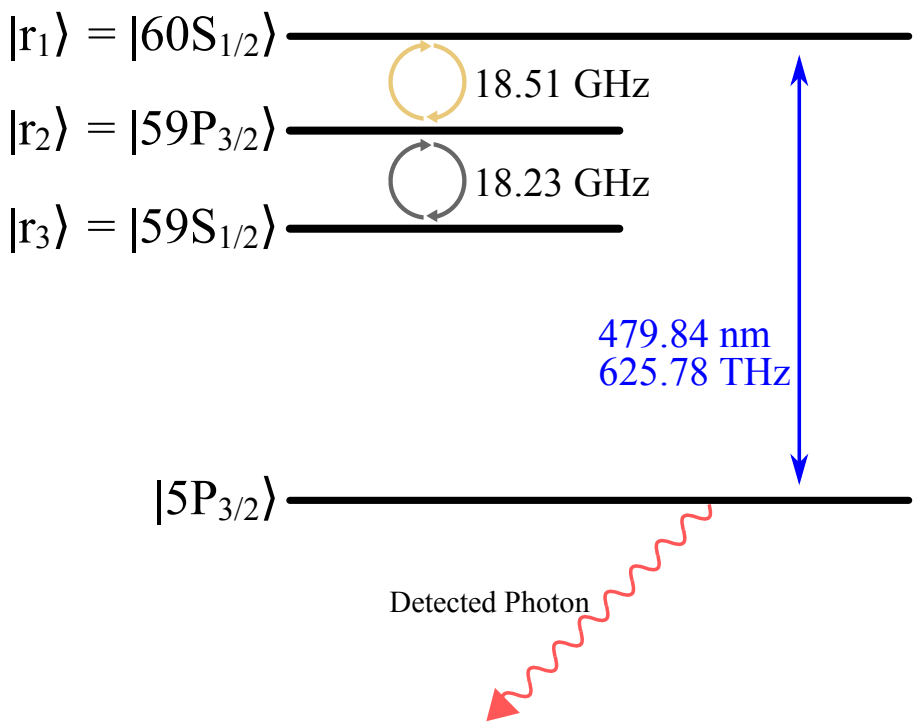

Figure 4.3: Qutrit level structure and optical readout scheme. The three qutrit basis states $|r_1\rangle$, $|r_2\rangle$ and $|r_3\rangle$ correspond to the Rydberg levels $|60S_{1/2}\rangle$, $|59P_{3/2}\rangle$ and $|59S_{1/2}\rangle$, respectively. Microwave transitions between $|r_1\rangle \leftrightarrow |r_2\rangle$ and $|r_2\rangle \leftrightarrow |r_3\rangle$ are driven by fields at 18.51 GHz and 18.23 GHz. The control beam at 479.84 nm couples $|r_1\rangle$ to the excited state $|5P_{3/2}\rangle$, enabling optical retrieval of the collective excitation as a single photon.

$$|\psi\rangle = \alpha\,|r_1\rangle + \beta\,|r_2\rangle + \gamma\,|r_3\rangle\,, \tag{4.2}$$

where the coefficients α, β and γ are determined by the applied pulse areas and phases. In the standard preparation used in Figure 4.4, we implement a balanced superposition with $\alpha = \sqrt{\frac{1}{2}}$, $\beta = \sqrt{\frac{1}{4}}$ and $\gamma = \sqrt{\frac{1}{4}}$.

The final populations are extracted using three sequential π pulses that map $|r_3\rangle$, $|r_2\rangle$ and $|r_1\rangle$ back to the readout state. First, the population remaining in $|r_1\rangle$ is

retrieved directly. Next, a μ_1 π pulse transfers the population from $|r_2\rangle$ to $|r_1\rangle$, which is then read out. Finally, the $|r_3\rangle$ population is transferred in two steps: a μ_2 π pulse moves it to $|r_2\rangle$, followed by a second μ_1 π pulse that brings it into $|r_1\rangle$ for readout. The detected retrieval trace shows three temporally resolved peaks corresponding to the state populations $P(|r_1\rangle)$, $P(|r_2\rangle)$ and $P(|r_3\rangle)$, as shown in Figure 4.4. These features are used to quantify the coherence and control of the qutrit.

To obtain accurate population values, each peak in the photon count trace was fitted empirically using an asymmetric Gaussian profile with a fixed baseline corresponding to the base detection count rate. The functional form,

$$f(t) = B + A \begin{cases} \exp[-(t-t_0)^2/(2\sigma_{\mathrm{L}}^2)], & t < t_0, \\ \exp[-(t-t_0)^2/(2\sigma_{\mathrm{R}}^2)], & t \geq t_0, \end{cases} \tag{4.3}$$

accounts for the asymmetric temporal profiles of the retrieved pulses. Each feature was fitted independently, and the fitted curve was integrated analytically to obtain the total photon number associated with that state. For a split Gaussian profile of amplitude A_i and left and right widths $\sigma_{\mathrm{L},i}$ and $\sigma_{\mathrm{R},i}$, the integral of the baseline-subtracted signal is

$$N_i = A_i \sqrt{\frac{\pi}{2}} (\sigma_{\mathrm{L},i} + \sigma_{\mathrm{R},i}) \,, \tag{4.4}$$

which represents the total number of photons retrieved from state i. The relative population in each state is then obtained by normalising these photon numbers such that $P(|r_1\rangle) + P(|r_2\rangle) + P(|r_3\rangle) = 1$.

For consistency, the fitted areas were also limited to the region within which the signal remained above $1/e^2$ of its maximum amplitude, corresponding to the interval $[t_0 - \sqrt{2}\sigma_{\mathrm{L}},\, t_0 + \sqrt{2}\sigma_{\mathrm{R}}]$. The resulting effective populations were found to be

$$P(|r_1\rangle) = 0.554 \pm 0.003, \qquad P(|r_2\rangle) = 0.283 \pm 0.005, \qquad P(|r_3\rangle) = 0.163 \pm 0.003.$$

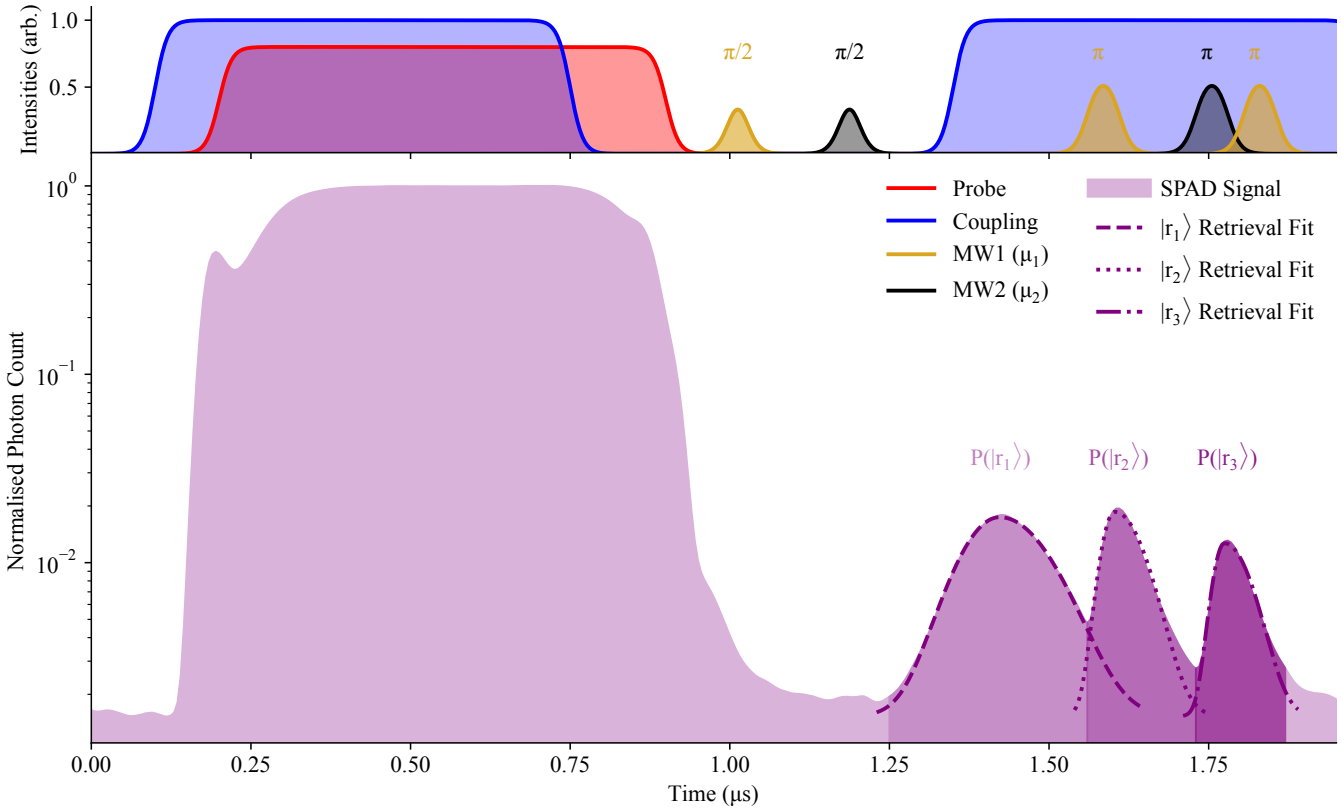

Figure 4.4: Qutrit control sequence and state resolved population retrieval. **Top:** Timing diagram showing probe and coupling pulses for polariton storage and retrieval, alongside microwave control pulses on transitions $|r_1\rangle \leftrightarrow |r_2\rangle$ (μ_1, yellow) and $|r_2\rangle \leftrightarrow |r_3\rangle$ (μ_2, black). After storing a single photon in $|r_1\rangle$, two $\pi/2$ pulses create a coherent qutrit superposition. State selective readout is performed using a sequence of π pulses, with each target state mapped back to $|r_1\rangle$ for optical retrieval. **Bottom:** Detected retrieval signal showing three readout peaks corresponding to the final populations in $|r_1\rangle$, $|r_2\rangle$ and $|r_3\rangle$. The solid lines represent the empirical fits to each feature, with shaded regions indicating the $1/e^2$ of the maximum amplitude, which were used to calculate the effective populations $P(|r_1\rangle) = 0.554 \pm 0.003$, $P(|r_2\rangle) = 0.283 \pm 0.005$, and $P(|r_3\rangle) = 0.163 \pm 0.003$. The dashed, dotted, and dash-dotted lines represent the respective fits to each state, highlighting the minimal overlap between features.

Integration of the fitted functions over each peak's $1/e^2$ window yields overlap fractions of $X_1 = 0.1\%$, $X_2 = 5.2\%$, and $X_3 = 0.1\%$, where each X_i represents the proportion of the fitted population $P(|r_i\rangle)$ that arises from neighbouring pulse contributions within the integration window. These values show that only the central feature, $P(|r_2\rangle)$, exhibits a small degree of temporal overlap, while the outer states remain well isolated in time.

The deviation from the idealised superposition reflects imperfect microwave pulse calibration and residual dephasing during the state-selective retrieval sequence. These results represent preliminary measurements; due to the unscheduled vacuum break described in Chapter 5, the calibration could not be further optimised or repeated under improved conditions. Having established state preparation and readout, we next probe coherent population dynamics between the excited Rydberg states.

4.4 Coherent Population Transfer

To demonstrate coherent control within the qutrit manifold, we perform a Rabi experiment by varying the duration t_{μ_2} of the μ_2 pulse that couples $|r_2\rangle$ and $|r_3\rangle$. A fixed $\pi/2$ pulse on μ_1 first prepares a superposition of $|r_1\rangle$ and $|r_2\rangle$. The μ_2 pulse is then applied with variable duration, inducing coherent population transfer between $|r_2\rangle$ and $|r_3\rangle$. The state selective retrieval sequence described in Figure 4.4 is used to extract the final populations in each qutrit state. The only modification to the previous sequence is the introduction of a variable length μ_2 pulse instead of a $\pi/2$ pulse before the retrieval stage.

Figure 4.5 shows the resulting Rabi oscillations. The populations $P(|r_2\rangle)$ and $P(|r_3\rangle)$ exhibit clear antiphase oscillations, consistent with coherent dynamics driven by μ_2. Small deviations from ideal sinusoidal behaviour are evident, including unequal amplitudes, which we attribute to residual microwave pulse imperfections and dephasing during the retreival sequence. The population in $|r_1\rangle$ remains approximately constant throughout, suggesting that the dynamics are confined to the $|r_2\rangle$–$|r_3\rangle$ subspace. These measurements confirm coherent control across the full qutrit basis. Due to an unscheduled vacuum break documented in Chapter 5, these results represent preliminary data and improved measurements could not be acquired.

These measurements confirm that the Rydberg ensemble supports coherent popula-

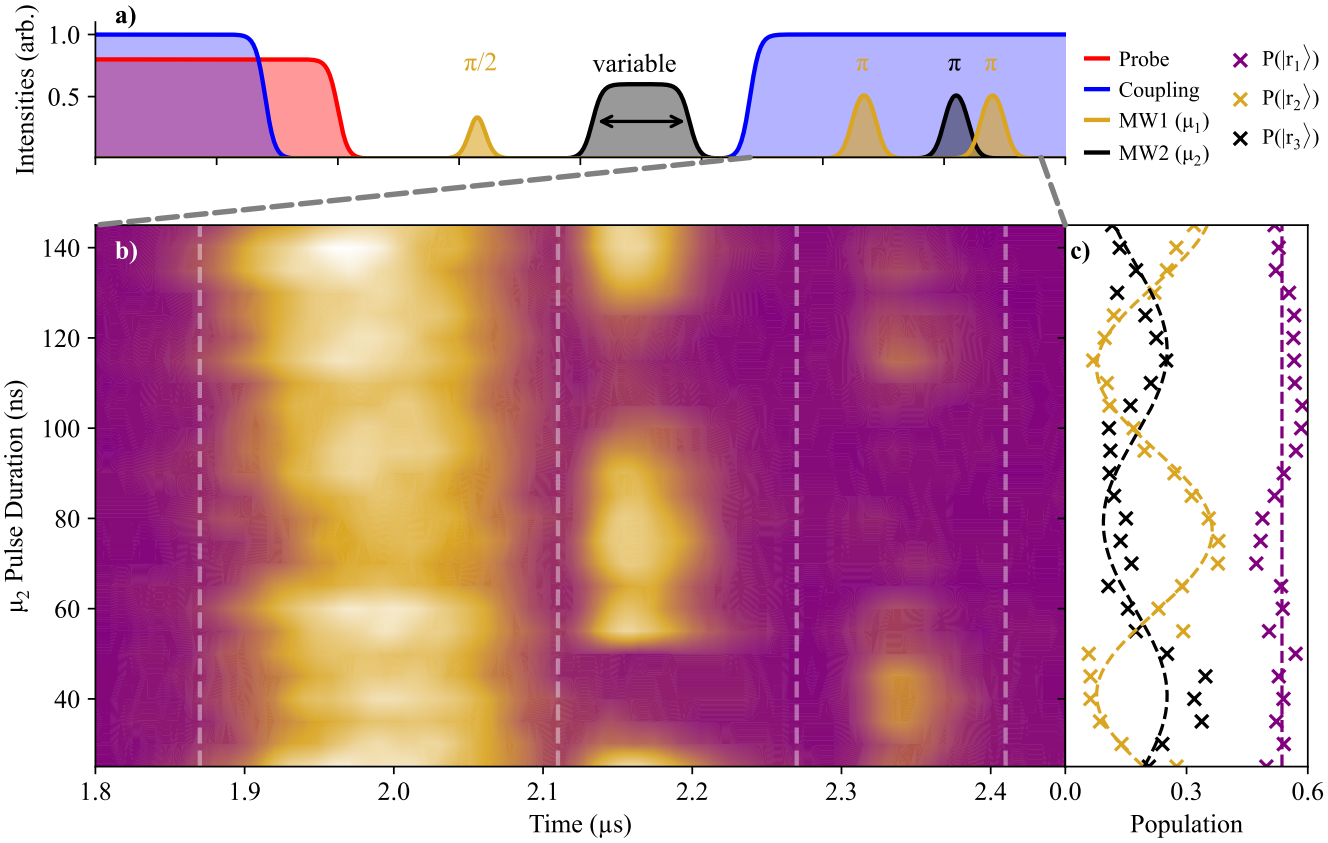

Figure 4.5: Qutrit Rabi oscillations between $|r_2\rangle$ and $|r_3\rangle$. **(a)** Full experimental pulse sequence used in the Rabi experiment. A $\pi/2$ pulse on μ_1 prepares a superposition of $|r_1\rangle$ and $|r_2\rangle$, followed by a variable timed μ_2 pulse that drives coherent population transfer between $|r_2\rangle$ and $|r_3\rangle$. After this, a sequence of three π pulses enables state-selective retrieval. **(b)** Time-resolved retrieval signal as a function of μ_2 pulse duration. Each horizontal slice corresponds to a single measurement of the retrieved photon signal. Vertical white dashed lines denote the time bins used to extract populations in $|r_1\rangle$, $|r_2\rangle$ and $|r_3\rangle$. **(c)** Extracted populations summed over time according to the time bins. $P(|r_1\rangle)$ (purple), $P(|r_2\rangle)$ (yellow) and $P(|r_3\rangle)$ (black) as a function of μ_2 pulse duration. The antiphase oscillations of $P(|r_2\rangle)$ and $P(|r_3\rangle)$ confirm coherent Rabi dynamics in the $|r_2\rangle$–$|r_3\rangle$ subspace. Dashed lines are sinusoidal fits to guide the eye.

tion dynamics across all three qutrit states, with state selective control and readout. This capability forms the basis for subsequent interferometric characterisation of qutrit coherence.

4.4.1 Ramsey Interferometry

To probe quantum coherence between the qutrit states $|r_2\rangle$ and $|r_3\rangle$, we implement a Ramsey interferometric protocol based on microwave pulses in the upper Rydberg manifold. This builds directly on the Rabi oscillations presented in Section 4.4, extending the verification of coherent control from population dynamics to phase stability. By inducing and measuring interference in the final state populations, the Ramsey sequence provides direct evidence of phase coherence within the $|r_2\rangle$–$|r_3\rangle$ subspace.

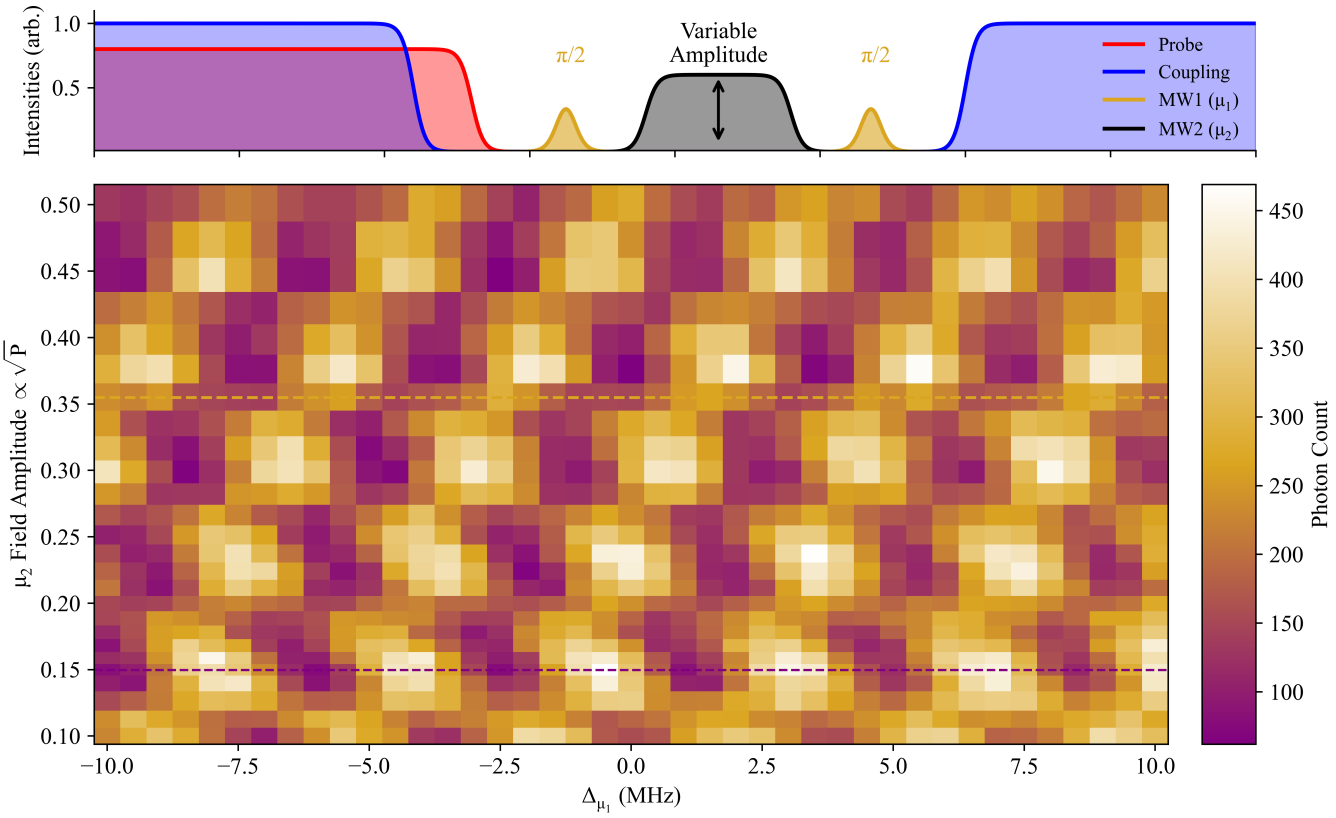

Figure 4.6: Ramsey interferometry in the $|r_2\rangle$–$|r_3\rangle$ subspace. **(a)** Pulse sequence showing probe (red), coupling (blue) and microwave fields (yellow and black). The μ_2 (black) pulse acts as a phase-evolution operator between two μ_1 (yellow) $\pi/2$ pulses. **(b)** Ramsey fringe pattern extracted from retrieval as a function of μ_1 detuning and μ_2 amplitude. Dashed lines indicate cross-sections shown in Figure 4.7.

The pulse sequence is illustrated in Figure 4.6 (a). A standard storage process first

prepares the system in $|r_1\rangle$ (see Section 4.2). A Ramsey sequence is then applied, comprising two μ_1 $\pi/2$ pulses, separated by a μ_2 pulse with variable amplitude. The first μ_1 pulse creates a superposition of $|r_1\rangle$ and $|r_2\rangle$, which evolves under μ_2 into a superposition involving $|r_3\rangle$ in the form of the general qutrit state defined in Equation 4.2. The second μ_1 pulse then projects this superposition back into the measurement basis. After recombination by the second μ_1 pulse, population in $|r_1\rangle$ is optically retrieved and detected, a measurement of the final qutrit state along the $|r_1\rangle$ axis. The resultant Ramsey fringes are shown in Figure 4.6 (b).

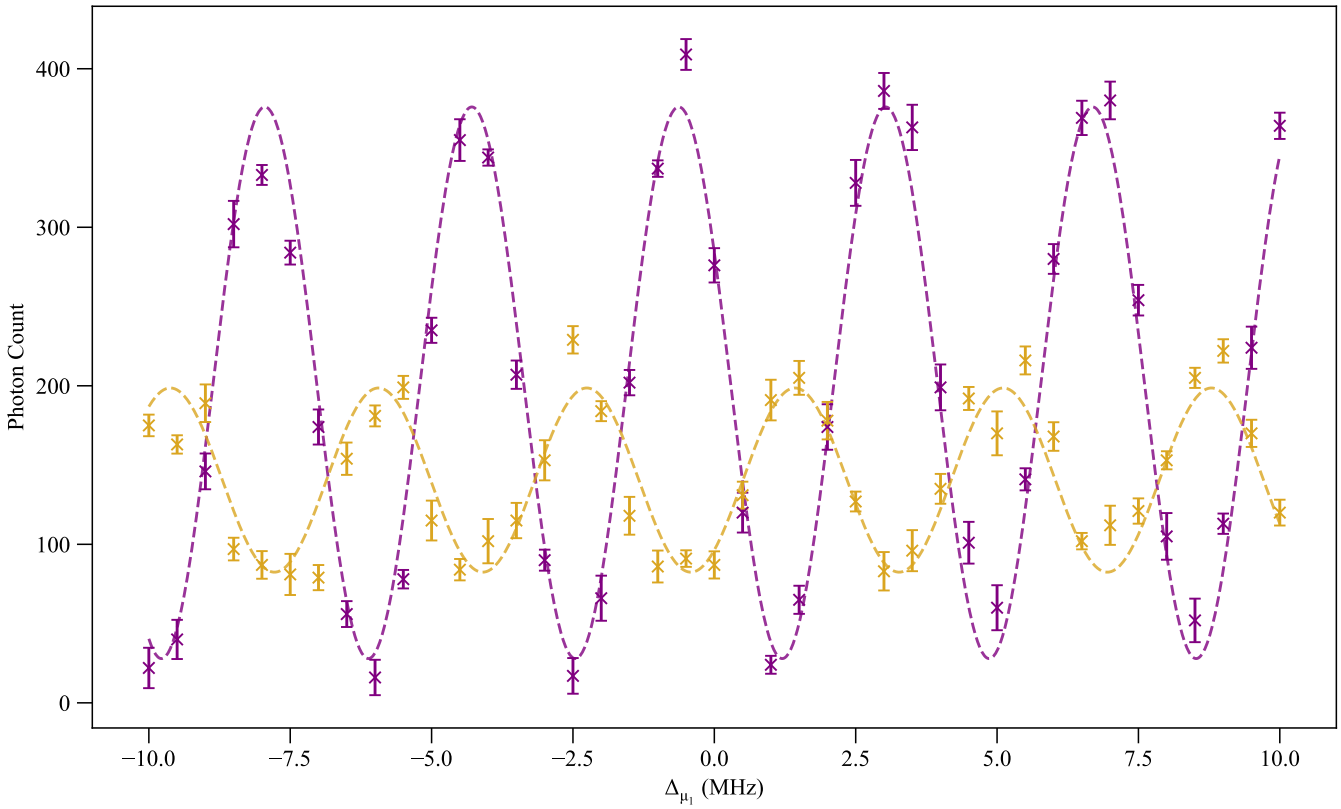

Figure 4.7: Cross-sections through the Ramsey heatmap (marked with purple and yellow dashed lines in Figure4.6). Ramsey fringes for two μ_2 amplitudes, with sinusoidal fits (dashed lines). A clear phase shift and contrast change are observed.

Two representative cross-sections through the Figure 4.6 (b) fringe pattern are shown in Figure 4.7, corresponding to distinct values of μ_2 amplitude. Oscillations in the retrieved photon signal reflect phase interference between $|r_2\rangle$ and $|r_3\rangle$. A clear shift in fringe phase is observed, along with a reduction in amplitude and

therefore visibility, consistent with increased dephasing or imperfect μ_2 pulse area.

To interpret the observed variation in contrast, we model the visibility as a function of the effective μ_2 rotation angle, defined as $\phi = \Omega_{\mu_2} t_{\mu_2}$. Under idealised evolution in the $|r_2\rangle$–$|r_3\rangle$ subspace, the visibility of the Ramsey interference pattern is expected to follow [3]:

$$V(\phi) = \left| \frac{2\cos(\phi/2)}{1+\cos^2(\phi/2)} \right|. \tag{4.5}$$

This expression predicts maximal visibility when ϕ is a multiple of 2π and vanishing contrast when $\phi = (2k+1)\pi$, corresponding to complete transfer into $|r_3\rangle$. A fit of this model to the measured visibilities captures both the periodicity and decay of the fringe visibility shown in Figure 4.8.

Although the model reproduces the expected periodicity, the residuals (Figure 4.8) exhibit a systematic trend: all but one lie below the theoretical curve. This indicates that the measured visibilities are uniformly lower than predicted, consistent with a small systematic reduction in contrast rather than random noise.

Such behaviour is expected with experimental imperfections such as amplitude or phase noise in the microwave drive, slow drifts in atom number, or residual laser frequency fluctuations. In particular, noise processes can only diminish interference contrast and therefore naturally lead to negative residuals when compared with the idealised model of Eq. 4.5.

Hence the sign of the residuals most likely reflects the cumulative effect of experimental noise and calibration uncertainty, rather than a deficiency in the visibility model itself. Within these limitations, the data remain consistent with coherent evolution in the $|r_2\rangle$–$|r_3\rangle$ subspace.

The right-hand panel of Figure 4.8 shows the same data stacked over multiple cycles and expressed in phase units between 0 and π. This representation highlights a

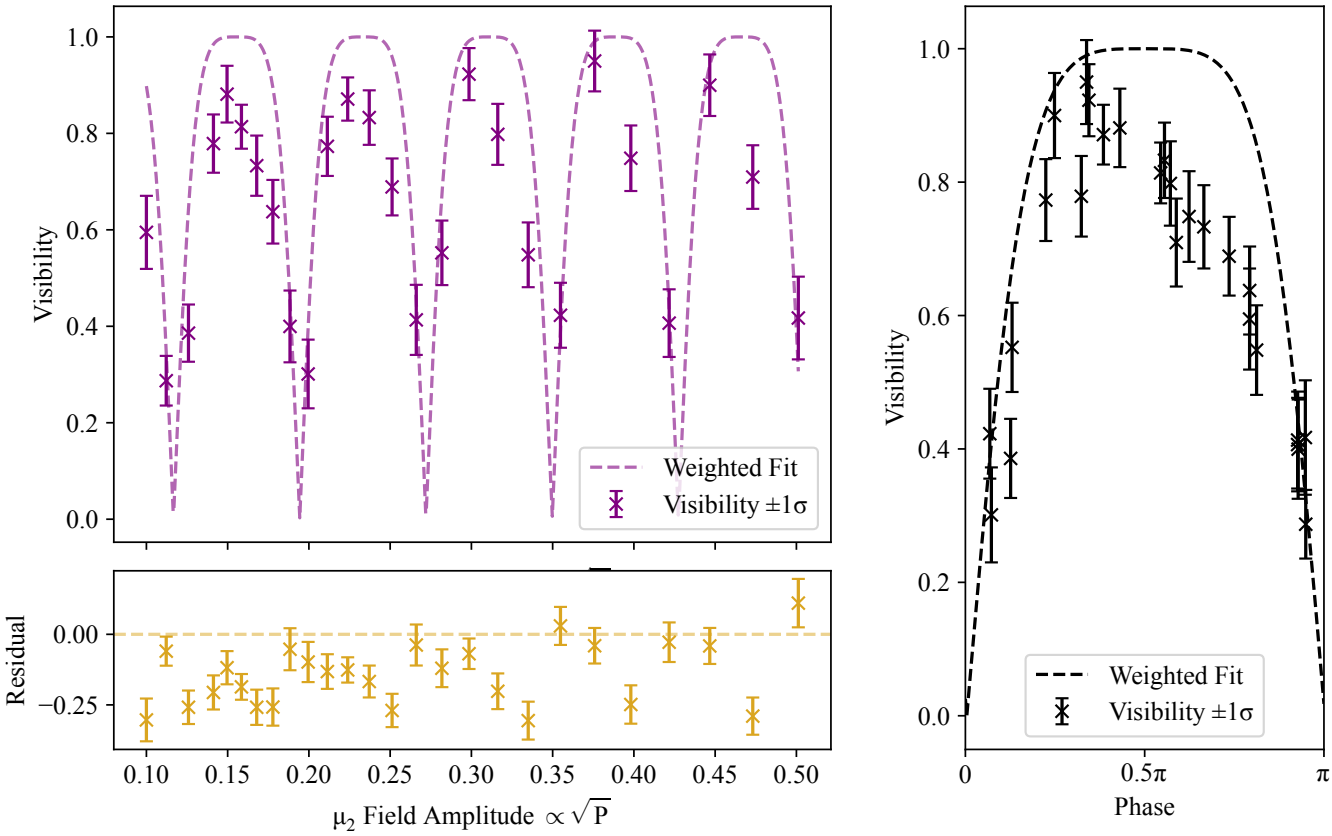

Figure 4.8: Ramsey fringe visibility as a function of μ_2 field amplitude. **Left:** measured visibilities as a function of microwave field amplitude with empirical fit (top) and corresponding residuals (bottom). The periodic model reproduces the expected contrast variation but shows a systematic offset in the residuals, indicating a constant reduction in measured visibility. **Right:** data stacked over successive oscillation cycles and rescaled in phase between 0 and π, showing the asymmetry in fit quality between the left and right sides of the periodic function. Error bars represent uncertainties from individual Ramsey fringe fits.

slight asymmetry in the fitted curve, with marginally better agreement on the rising (left-hand) side compared with the falling (right-hand) side.

These measurements were acquired before the unscheduled vacuum break described in Chapter 5, which limited further optimisation. Nonetheless, the results provide clear evidence of coherent phase evolution in a three level Rydberg system. With improved stability and calibration, this approach may enable future implementations of full quantum process tomography or gate based protocols [123, 125].

4.5 Coherence and Control in a Rydberg Qutrit

The results presented in this chapter demonstrate coherent control of a three-level quantum system encoded in single Rydberg excitations. Using a combination of polariton storage, microwave driven state transfer and time resolved photon retrieval, we have made progress in verifying population dynamics and phase coherence within the $|r_1\rangle$–$|r_2\rangle$–$|r_3\rangle$ manifold. In particular, Ramsey interferometry in the upper Rydberg subspace reveals interference fringes whose contrast and phase depend sensitively on the amplitude of a variable microwave pulse. The extracted fringe visibility shows the same periodicity and phase as theoretical predictions based on unitary rotation in the $|r_2\rangle$–$|r_3\rangle$ subspace, confirming the phase preserving nature of the control sequence.

Taken together, these measurements constitute a direct demonstration of qutrit coherence in a cold atom Rydberg platform. The ability to implement controlled superpositions, drive coherent population transfer and resolve interference in state selective retrieval establishes the foundational toolkit for more complex protocols. This includes quantum state tomography and qutrit gate operations [126, 130, 131].

While the current dataset was acquired prior to the system improvements described in Chapter 5, it provides clear evidence that the underlying platform supports coherent qutrit operations. With improved vacuum conditions and enhanced stability, further gains in coherence time, visibility and readout fidelity are expected. These improvements would enable more stringent tests of qutrit gate performance and could be expanded to a more generalised qudit scheme [125, 127, 128, 130, 131] .

Chapter 5

Vacuum Break and Experimental Changes

The following chapter outlines the sequence of modifications, restorations and design updates made to the experimental vacuum apparatus following a catastrophic system failure. The initial vacuum break was caused by an accident that resulted in the irrecoverable loss of vacuum due to a crack in the ceramic seal of a high-voltage electrical feedthrough. This component was subsequently replaced with an identical part, a LewVac FHP5-25C4-16CF.

In the course of recovering the system a total of three vacuum breaks were performed. The first was to replace the damaged feedthrough. The second followed the discovery of a leak in a homemade viewport [132], which was ultimately replaced by a commercially manufactured LewVac DN40CF viewport. The third and final, vacuum break occurred following the failure of the initial rubidium dispenser activation: a large quantity of rubidium was deposited on the walls of the 2D MOT cell, reducing optical transmission below functional levels. After unsuccessful attempts to remove the rubidium via Light-Induced Atomic Desorption (LIAD), thermal cycling and laser ablation, the 2D MOT cell was replaced.

For clarity and brevity, the detailed procedures described in this chapter refer to

this third and final vacuum reconstruction unless otherwise stated.

This chapter proceeds by first summarising the preparatory steps required before work could be done on the vacuum system, followed by a description of the reassembly and re-evacuation of the chamber, as detailed in Sections 5.1-5.2.5. The latter half of the chapter, presented in Section 5.3, outlines specific hardware changes and adaptations made to the system.

5.1 Preparation

The repair of the vacuum system began with a detailed cleaning and preparation process to ensure the integrity and cleanliness of all components to be introduced into the UHV environment.

5.1.1 Cleaning

Components added to the vacuum chamber were cleaned using a multi-stage protocol adapted from established procedures for UHV preparation [133]. The goal of this procedure was to remove surface contaminants, such as hydrocarbons and machining residues, that could otherwise outgas under vacuum leading to an increase in pressure.

Initially, all metal components were submerged in a 5% solution of Decon 90 in deionised water and placed in an ultrasonic bath for 30 minutes. Extreme care was taken to orient components in the bath such that CF flange knife edges did not contact any hard surfaces, preventing nicks that would compromise sealing.

Following this stage components were rinsed and then transferred into an ultrasonic bath of 5% acetone solution for a further 30 minutes. Notably, during this step, the Viton O-ring in the original gate valve became visibly stretched and brittle, suggesting long term degradation exacerbated by the solvent exposure. This failure

rendered the valve unusable and led to its removal from the vacuum design, which was subsequently replaced by a compact 4-way cross (see Section 5.3.2).

5.1.2 Spot Welding and Assembly

Dispenser wires were spot welded onto the electrical feedthrough pins using a precision discharge welder. Initial trials were conducted on old dispenser filaments to determine the required power settings. Starting at low current, power was incrementally increased to achieve reliable connections without overheating the wire.

After successful attachment, the dispensers were mounted into the new upper glass cell and the entire upper chamber assembly was joined to the main vacuum chamber using copper gaskets and CF flanges. Care was taken to minimise torque asymmetry and to follow cross pattern tightening for all flanges to preserve gasket conformity and prevent leaks.

5.2 Evacuation

Once the vacuum chamber was reassembled, the system underwent a multi-stage evacuation procedure to achieve UHV conditions. This process consisted of five main stages: an initial pump-down using a turbomolecular and rotary pump, a high temperature bake-out to remove adsorbed gases from interior surfaces, activation of the Non-Evaporable Getter (NEG) element, initiation of the ion pump and finally the activation of the rubidium dispensers. These stages were carefully monitored and certain steps were repeated, such as additional baking, to ensure optimal conditions for trapping atoms.

5.2.1 Pump Down

The system was initially evacuated using a combination of a diaphragm rotary pump and a turbomolecular pump. The roughing pump brought the chamber

from atmospheric pressure down to approximately 10^{-3} mbar, at which point the turbopump was engaged to reach high vacuum levels. The pressure was monitored via a cold cathode gauge. The pumping setup is shown in Figure 5.1.

This preliminary pump-down was critical not only for removing the bulk of atmospheric gases but also for verifying the integrity of the vacuum system. Prior to baking, all flanges, viewports and feedthroughs were visually inspected and retightened to ensure good copper seal compression.

Although leak testing with helium was also done (see Section 5.2.2), this initial evacuation stage served as a baseline check. The chamber was left under vacuum for several days to monitor the rate of pressure change and to allow for outgassing from internal surfaces. Once pressure reached the 10^{-7} mbar range and plateaued, the system was deemed ready for the next stage of preparation.

5.2.2 Leak Testing

To verify the vacuum integrity of the system following reassembly, leak testing was conducted using a Residual Gas Analyser (RGA) capable of detecting species up to 100 amu. This procedure was carried out after the pump down and each bake-out once the chamber had reached a stable pressure at each stage, with particular importance put on the testing after bake-outs as small leaks can open up under thermal expansion.

The leak test operates by scanning for partial pressure spikes corresponding to helium gas, which is locally introduced at vacuum joins. Due to helium's small molecular size and chemical inertness, it is ideal for identifying small leaks that may not be otherwise detectable under static vacuum conditions.

The detector operates using an electron multiplier configuration to enhance sensitivity. A narrow helium nozzle was then used to gently apply helium gas to the periphery of all vacuum joints. Care was taken to flush the delivery tubing by

Figure 5.1: Experimental vacuum system during pump down and bake-out. The system is shown inside a bakeout oven with external heater tapes and thermocouples attached. The vacuum chamber is connected to the external pumping rig via flexible bellows and DN40CF flanges. Tin foil is used to minimise temperature gradients across the chamber, especially at glass and glass-metal interfaces, to prevent stress induced cracking. The pumping rig (not pictured) sits beneath the oven.

opening the regulator valve before the canister valve, preventing backflow of air into the helium source.

During this procedure, helium was systematically applied to all new connections, including standard CF flanges, glass-metal seals and electrical feedthroughs. When the probe passed over a leak site, the RGA registered a spike in the partial pressure of helium; a typical pressure spike is shown in Figure 5.2. A significant leak would be expected to register on the order of 10^{-7} mbar.

Although most of the system exhibited no anomalous signals, a clear helium response was detected when probing a homemade viewport. Specifically, helium applied to the recess holding the glass optic (rather than the knife edge seal) pro-

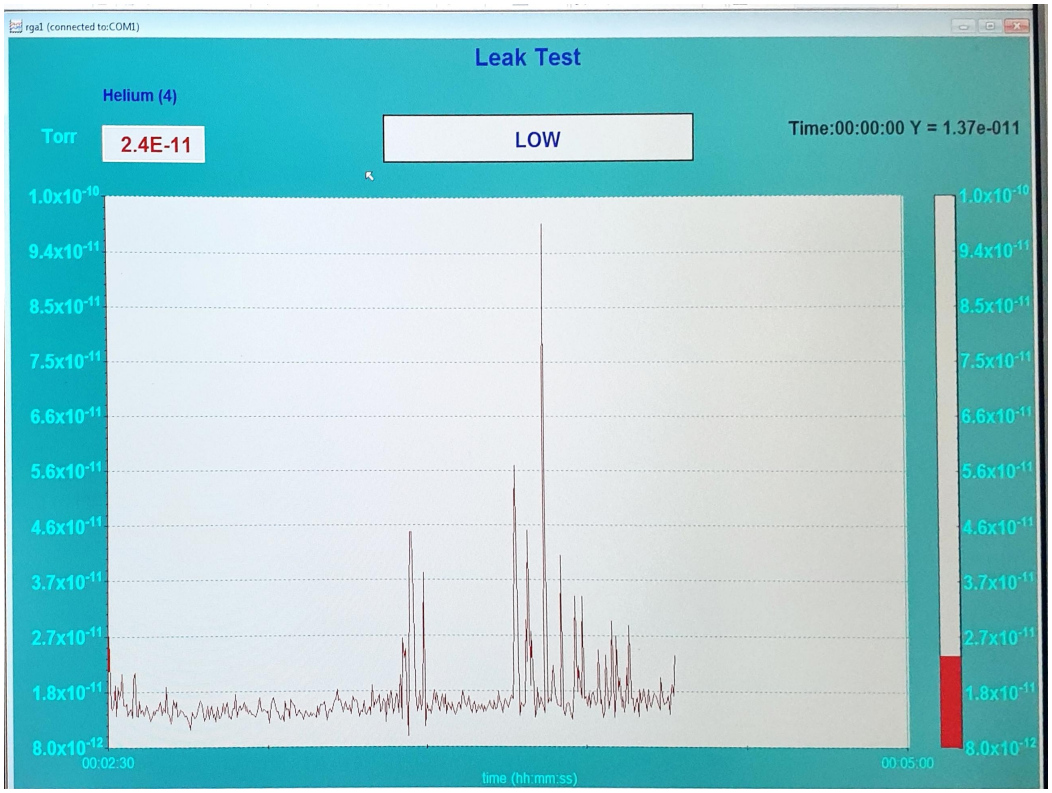

Figure 5.2: RGA (Residual Gas Analyzer) partial pressure readout in helium leak test mode. The peak shown is due to helium applied around a vacuum flange during routine leak checking. While this particular signal is not indicative of a significant leak, it is representative of the expected profile. A substantial leak would exhibit a similar structure but with a peak approximately three orders of magnitude higher (on the order of 10^{-7} mbar).

duced a measurable signal increase. Due to the fragility of the glass and the risk of fracture under additional torque, it was concluded that the unit could not be re-seated or repaired. A replacement LewVac DN40CF viewport, anti-reflection coated for 780nm and 480nm, was sourced and installed.

Besides this leak additional testing confirmed no remaining detectable leaks after each pump down and bake out stages of all three vacuum breaks. This validated the system's readiness and UHV operation.

5.2.3 Bake-Out

Following initial leak testing and confirmation of base pressure stability, the entire vacuum system was prepared for thermal bake-out to remove residual adsorbed gases from internal surfaces. This step is critical for achieving UHV conditions, as many contaminants, especially water vapour and hydrocarbons, desorb only under higher temperatures.

The final bake-out cycle documented here followed two earlier attempts, the first of which was interrupted by the failed homemade viewport that developed a leak and the second by the unsuccessful activation of the rubidium dispensers, which damaged the original 2D MOT cell (see Figure 5.6). All components had been thoroughly re-cleaned or replaced by this point.

The bake-out was performed by wrapping the majority of the chamber in fiber glass heater tape and insulation, carefully avoiding heat sensitive elements like the ion pump. The 2D MOT cell was surrounded by a copper tube before being warped to ensure even heading across the glass and the glass-metal boundaries to ensure the were no significant temperature gradients that could lead to a crack. Three thermocouples monitored the temperature of key locations: the upper dispenser region (to make sure we did not heat to a point they could be activated prematurely), the main chamber body and the ion pump. The dispenser oven temperature was regulated using a dedicated feedback loop from the sensor on the main chamber. This setup is shown in shown in Figure 5.1.

During the bake, chamber temperatures were ramped up to 140° C over several hours and held for an extended duration. A characteristic pressure increase of approximately one order of magnitude per 100° C was observed, consistent with desorption of surface bound gases [134]. Once the target temperature was maintained for a sufficient period, heating was ceased and the system was allowed to cool gradually while under continuous pumping, depicted in Figure 5.3. Final pressures were monitored until a stable baseline was established.

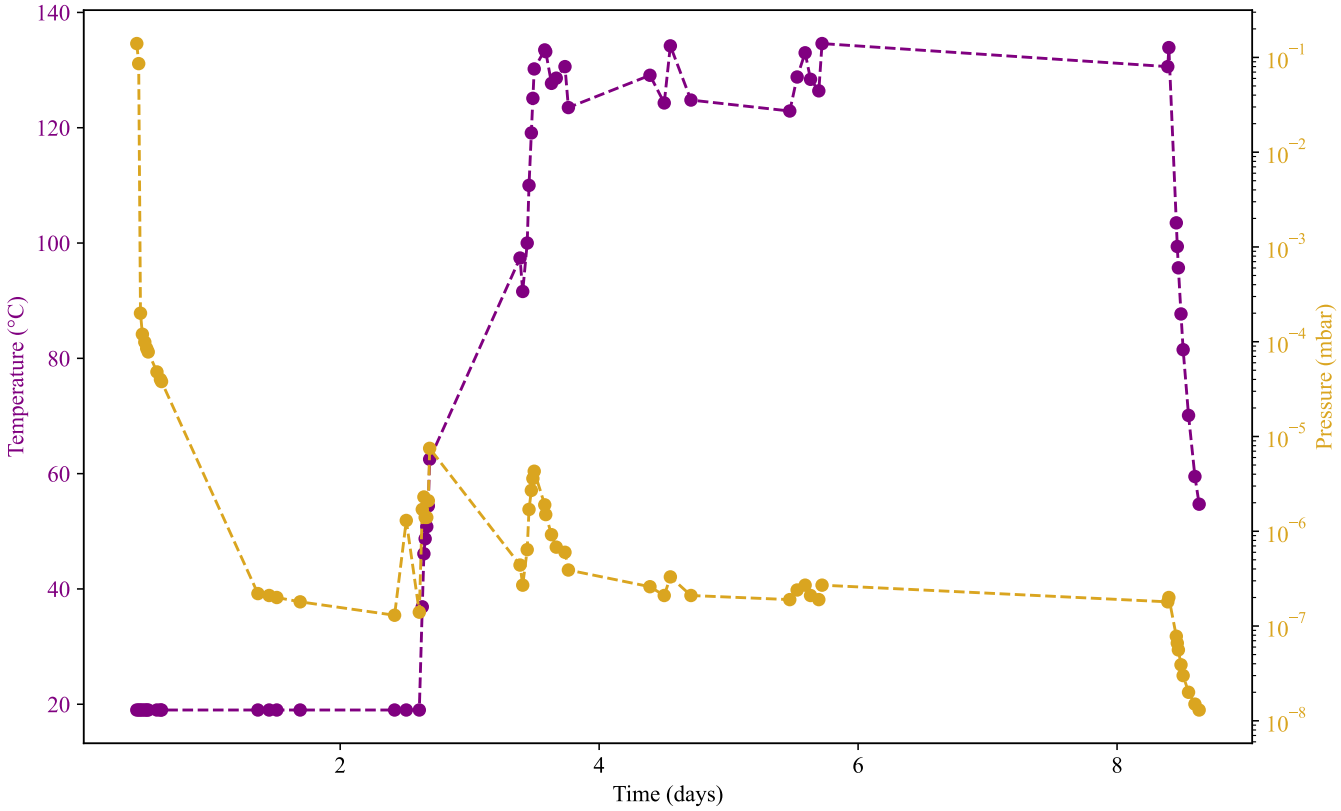

Figure 5.3: Pressure (yellow) and temperature (purple) profile during the pump-down and final bake-out of the vacuum system. The onset of temperature increase above room temperature marks the start of the bake, which was carried out over several days using fibreglass heating tapes and monitored via thermocouples. As the temperature rose, thermal desorption led to a corresponding increase in chamber pressure. The overall decline of more than two orders of magnitude in the bake-out phase confirms recovery of UHV conditions.

5.2.4 NEG and Ion Pump Activation

Following the bake-out and leak testing, attention was turned to the activation of the vacuum pumps. The system uses a NEXTorr D100-5 pump, which combines a NEG with a ion pump. The NEG component requires periodic activation to restore its pumping capacity, while the ion pump must only be used once the vacuum is sufficiently low to prevent electrical arcing.

The NEG activation began by wrapping the pump body in fibreglass heater tape and insulating it with foil and a fire blanket. The system was brought up to a stable conditioning temperature of 170° C in controlled increments to avoid overshooting.

After temperature stabilisation, the NEG was placed into its conditioning mode, during which moderate power is applied. The conditioning phase is necessary to drive surface contaminants deeper into the NEG material, ensuring effective absorption performance upon activation. The temperature and pressure profile during conditioning and activation is shown in Figure 5.4.

Initial pressure during this phase rose to the low 10^{-4} mbar range, indicating substantial outgassing, but steadily declined over the course of conditioning. After approximately 19 hours, the pressure had fallen to the 10^{-8} mbar range and the temperature had stabilised near 70° C, at which point a timed activation sequence was initiated. During this phase, the NEG was ramped to full power with no observed arcing or fault conditions and completed activation without incident. The system was allowed to cool before heater tape and insulation were removed and magnets were reinstalled.

Following this, the ion pump was engaged. Initially, the pump current was around 200mA but quickly decreased. Within two hours, the current had fallen to 15nA, consistent with previous operating behaviour. This low current indicated a healthy vacuum state and successful pump operation.

A few days later the base pressure reached $< 10^{-10}$ mbar (or a current of 0-3nA); the lowest pressure the controller can read, confirming the system had returned to UHV conditions and was ready for the next stage of the procedure.

5.2.5 Dispenser Activation

The rubidium dispensers, once spot-welded into the vacuum system, require electrical activation to release rubidium vapour into the chamber. This is achieved by passing a current through the dispenser, causing an internal indium seal to melt and release inert argon gas, followed by rubidium vapour released from an alloy when heated. Because the rubidium alloy is very reactive in air, it is performed after establishing UHV conditions.

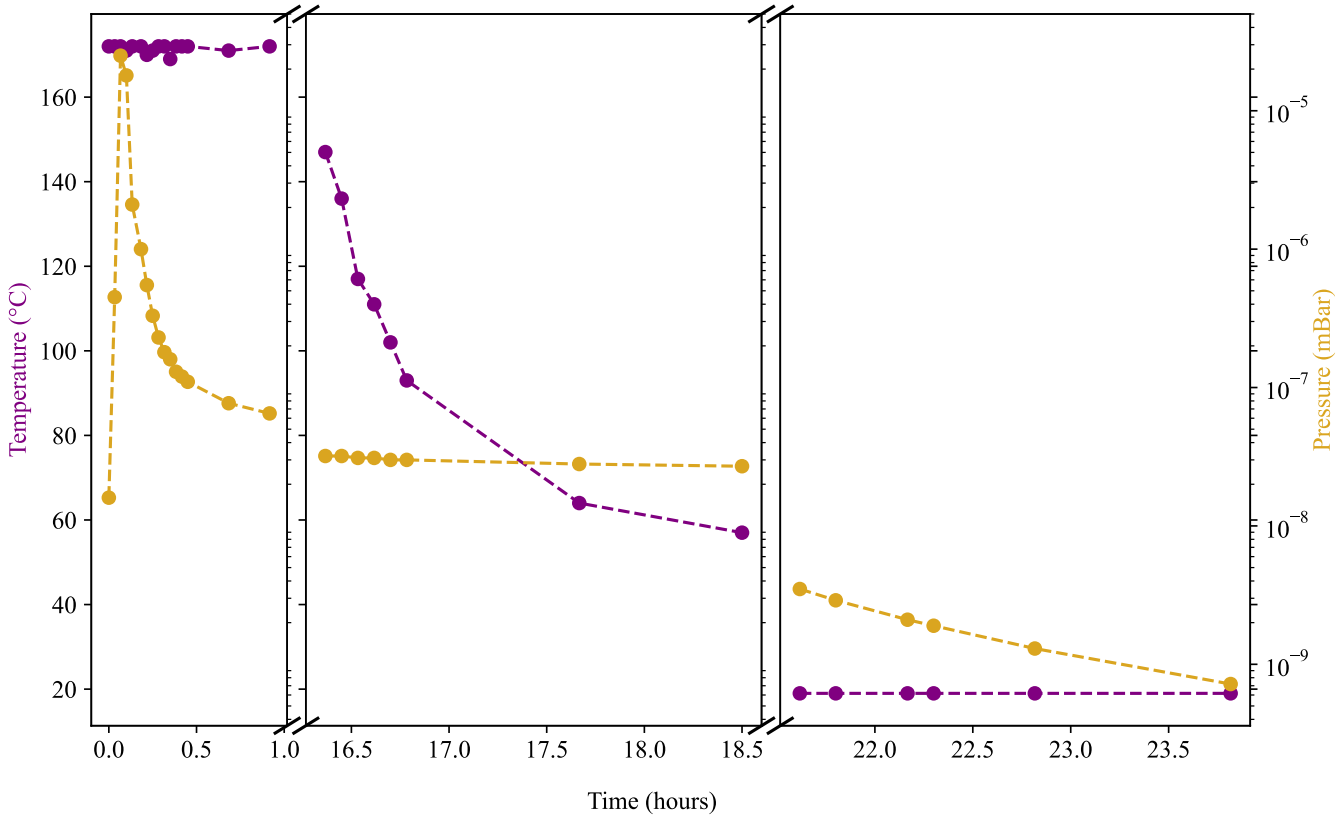

Figure 5.4: Temperature (purple) and pressure (yellow) during the conditioning and activation of the NEXTorr D100-5 pump. The NEG was gradually heated to approximately 170°C in controlled increments and held there during an extended conditioning cycle to desorb surface contaminants. This process initially raised the chamber pressure to the 10^{-4} mbar range, followed by a steady decline as the NEG began absorbing residual gases. The timeline includes two breaks in the time axis: one overnight during the NEG conditioning phase and another between the end of conditioning and the initiation of the ion pump. Following NEG activation, the ion pump was engaged and the pressure continued to fall. After several days, the system reached a final pressure below 10^{-10} mbar,the lowest detectable value for the ion gauge, confirming successful re-establishment of UHV conditions.

Before activation, electrical continuity was verified using a multimeter to confirm no shorts between dispensers, to the chamber, or across the feedthrough.

The activation of the two dispensers was performed sequentially. A power supply was used to gradually ramp the current until a distinct argon spike was observed on the RGA. In the first attempt, current was increased until pressure spiked beyond the safe operating range of the ion gauge, requiring it to be powered down. This procedure released a large quantity of rubidium vapour, which subsequently

deposited heavily on the walls of the upper glass cell, as shown in Figure 5.6(a).

This accumulation of rubidium severely attenuated optical access and rendered the original 2D MOT cell unusable. Overactivation leads to rubidium condensing on chamber walls and optics. On glass, this creates metallic films that reduce transmission and are difficult to remove, especially under vacuum. Multiple cleaning techniques were attempted (discussed later in Section 5.3.1.1), but none restored sufficient transparency. This failure led to the third and final vacuum break to replace the upper cell.

In the second round of dispenser activation, a more conservative approach was taken. Currents were limited to lower levels and exposure durations increased to avoid overactivating the dispensers. While the initial argon spikes were smaller than expected, pressure stabilised and the RGA confirmed successful release of rubidium.

5.2.5.1 Mini-Bake of Upper Cell

To remove residual rubidium and indium used in the dispenser seal from the inner walls of the replacement 2D MOT cell, a partial reheat of the upper chamber was performed; colloquially referred to as a "mini-bake." The aim was to thermally desorb rubidium from the warm glass walls, allowing it to condense onto the cooler differential pumping tube or metal walls of the main chamber. This successfully removed the Rubidium deposits, as shown in Figure 5.5.

Heater tape and thermal insulation were wrapped around the upper cell and thermocouples were used to regulate the bake to 120° C, safely below the rubidium emission temperature of the dispensers. Two thermocouples were used: one near the cell wall and another at the case, with the latter eventually used for stable overnight control. Pressure readings were monitored throughout the procedure to track changes and confirm safe operation.

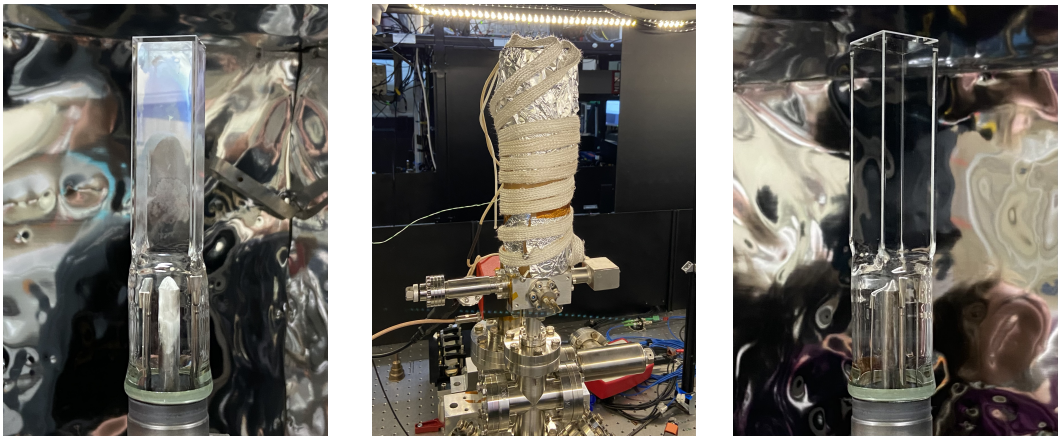

(a) Cell coated in rubidium (b) Mini-bake setup (c) Cleaned cell after bake

Figure 5.5: Progression of the mini-bake procedure. (a) Significant rubidium deposits on the inner surface of the 2D MOT cell following dispenser over-activation. (b) Mini-bake setup; heater tape and a copper heat jacket were used to raise the cell temperature locally while maintaining the rest of the chamber near room temperature. (c) Cell following mini bake out and successfully removal of rubidium, showing significantly improved optical clarity.

5.3 Design Changes

Several significant hardware upgrades were implemented during the reconstruction process. Table 5.1 summarises the key modifications, each of which is discussed in more detail in the following sections.

5.3.1 2D MOT Cell

5.3.1.1 Attempt at Repair

The original 2D MOT cell became unusable following the initial activation of the rubidium dispensers. The procedure released a significant quantity of rubidium vapour into the chamber, which subsequently condensed on the interior walls of the upper glass cell. The resulting deposits severely attenuated optical transmission, especially in the central cooling region and rendered the cell impractical for continued use.

Table 5.1: Summary of hardware changes to the vacuum system and their motivations.

Component	Change	Motivation
2D MOT Cell	Replaced with custom Pyrex cell (100 mm) without AR coating	Original 150 mm cell rendered unusable by rubidium deposits. Shorter, non-coated cell used due to time and cost constraints.
2D MOT Optics	Retrofitted with compensating lenses and new mounts	Adjusted for shorter, uncoated cell to maintain beam uniformity and adequate radiation pressure
Gate Valve	Replaced with 4-way cross	Degraded rubber seals rendered the valve unusable; simplification, better mechanical support and additional optical access
Electrical Feedthrough	Replaced like-for-like	Ceramic component cracked breaking vacuum; replacement ensured continued electrical integrity
Rubidium Dispensers	Switched from Alvatec AS-3-Rb-250-F to AlfaVakuo AS-Rb-3F-275	Alvatec no longer available; AlfaVakuo is successor and compatible replacement
Viewports	Homemade viewport replaced with LewVac DN40CF AR-coated window	Leak at glass recess of original unit

A range of cleaning and desorption techniques were explored in an attempt to recover the cell's transmission properties. These included:

- **Thermal desorption:** The upper chamber was wrapped in copper tubing and heater tape, then heated to approximately 120° C. The aim was to thermally excite the rubidium atoms off the glass and encourage recondensation onto colder metallic regions of the chamber; following the procedure described in Section 5.2.5.1 and shown in Figure 5.5. Although this process was repeated several times no measurable improvement was observed.
- **Light-Induced Atomic Desorption (LIAD):** A high-power (1.6W) 450 nm diode laser was used to irradiate the glass surfaces in an effort to release

rubidium atoms via photon-stimulated desorption [135, 136, 137]. Despite sustained exposure and varying beam alignment, no increase in optical transmission was recorded.

- **Laser Ablation:** A 1064nm IPG fibre laser with a red guiding beam was employed to ablate rubidium from the inner walls, using the setup shown in Figure 5.6(b). A weak probe beam was overlapped with the high power (several Watts) IR beam to monitor transmission changes in real time. Beam power, position and scan rate were varied systematically. In some cases, localised colour changes were observed (including the formation of a gold coloured film), as shown in Figure 5.6(a), suggesting possible partial desorption or chemical reaction; an effect that has previously been observed [138]. However, no consistent improvement in transparency was achieved.

After multiple rounds of diagnostics, probe transmission measurements and unsuccessful cleaning attempts, it was concluded that the deposits could not be removed to a satisfactory level. The cell was therefore replaced with a new, slightly shorter version with three cooling regions instead of four. Though this reduced the available trapping volume, the new cell's clarity restored essential optical access and MOT performance. The implications of this design change are discussed in more detail later in this chapter.

5.3.1.2 New 2D MOT Cell

Following the failure of the original 2D MOT cell due to heavy rubidium deposits that rendered the glass opaque, a replacement cell was installed. The new unit was custom made by Precision Glassblowing and, while similar, differed from the previous cell in a few notable respects. The replacement 2D MOT cell can be seen in Figure 5.5(a,c).

The new cell measured $25 \times 25 \times 100$ mm, compared to the 150 mm length of the original. This reduced the number of defined cooling regions from four to three.

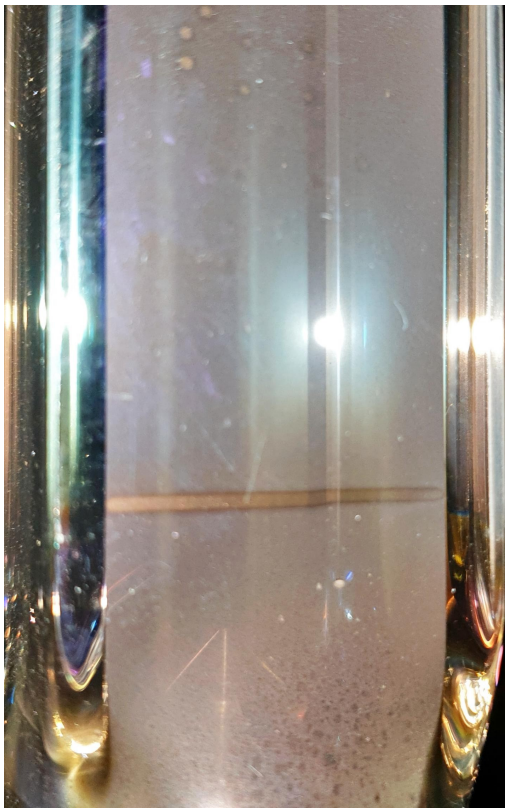

(a) Interior of the original 2D MOT cell showing rubidium deposits and discolouration from laser ablation attempts.

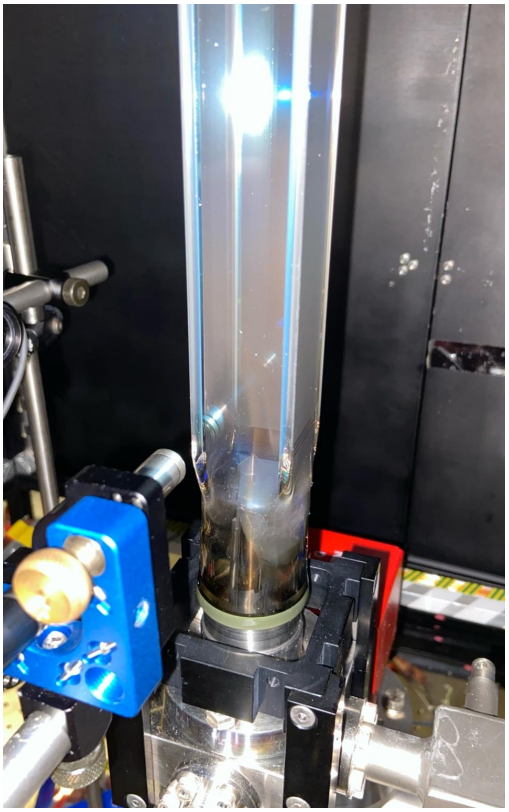

(b) Laser ablation setup using a 1064 nm fiber laser.

Figure 5.6: Characterisation and attempted recovery of the original 2D MOT cell following contamination by rubidium. (a) shows the extent of internal rubidium deposits and discolouration after dispenser over activation. (b) shows the setup used to remove the deposits using laser ablation. Despite multiple techniques, including laser ablation, thermal desorption and LIAD, no substantial improvement in transmission was achieved. The cell was ultimately replaced.

However, prior work on this experimental setup indicated that the lowest cooling region has the greatest impact on 3D MOT loading efficiency [112]. Therefore, the reduction in length was not expected to significantly affect performance.

The new cell was fabricated from Pyrex rather than Tempax glass and it did not include AR coatings on any surfaces. A measurement across two air-glass interfaces (i.e., one optical path through the cell) showed a transmission of 84.3%, corresponding to approximately 95.8% per interface, consistent with uncoated Pyrex [139].

5.3.1.3 2D MOT Optics

The installation of the new, shorter, uncoated 2D MOT cell required corresponding updates to the optical delivery system. Because the replacement cell lacks AR coatings, transmission through each glass interface is reduced, leading to a measurable drop in beam intensity along the cell axis. To mitigate this, a pair of weakly focusing lenses was introduced into the beam path to compensate for this intensity drop in the retroreflected beams.

Using transmission data from the cell and a Gaussian beam propagation model, an optimal focal length for the compensating lens was calculated such that the beam profile remains approximately uniform across the length of the cell, with specific emphasis on the centre. The results of this simulation are shown graphically in Figure 5.7. It shows that across the cell, the difference in intensity between the first pass and retro-reflection of the beam is reduced to 5% at the edges and close to 0% in the centre, compared to more than 15% across the whole cell when no lenses are used.

The simulation concluded that the optimal focal length would be 1032 mm, so for convenience we used standard 1" lenses with focal length, f = 1000 mm (ThorLabs LA1464-B).

Custom mounts were fabricated in-house (see Figure 5.8) to accommodate the new optical layout and to position the lenses precisely with respect to the vacuum viewport and cooling volumes. This modification ensured adequate radiation pressure in all three remaining cooling regions of the 2D MOT. The resulting optical access and beam profiles remained comparable to those of the previous system.

5.3.2 4-Way Cross

As part of the vacuum system overhaul, the gate valve situated between the main science chamber and the 2D MOT section was removed. This valve, which had

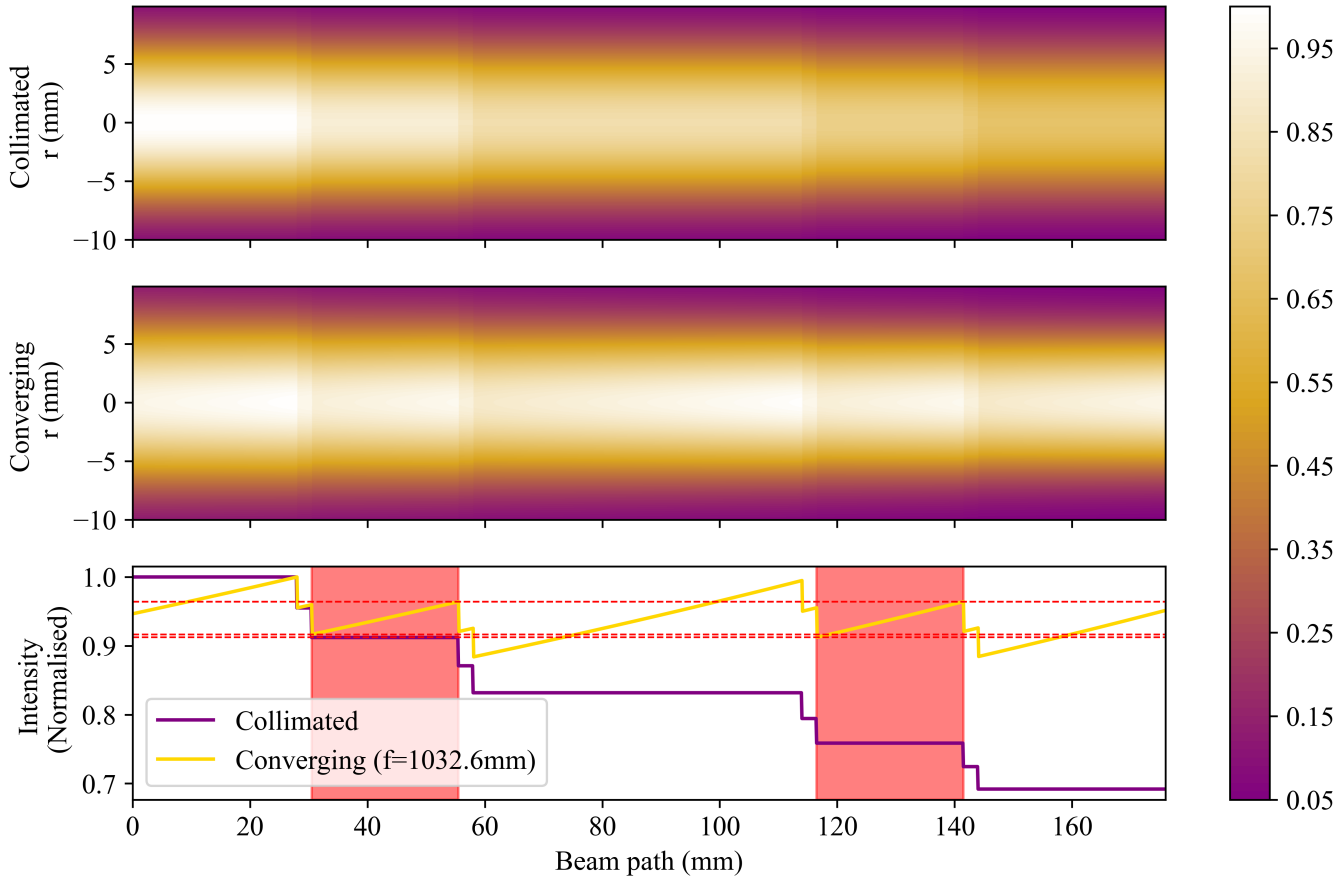

Figure 5.7: Simulated beam profiles along the axis of the 2D MOT cell. **Top:** Heatmap of simulated collimated Gaussian beam passing through four Pyrex panes. **Middle:** Heatmap of simulated converging Gaussian beam passing through four Pyrex panes. **Bottom:** Intensity at the axial centre of the beams. Without a converging lens (purple line), reflections at the glass interfaces reduce transmitted intensity. The addition of a weakly focusing lens (yellow line) compensates for these losses, leading to a more uniform beam intensity along the cell length. Red shaded regions correspond to the interior of the 2D MOT cell—the areas requiring uniform intensity. Dashed red lines denote the extremes of beam intensity in each region.

previously served as a isolation point between the two regions, was found to be no longer usable due to degradation of its internal rubber seals (discussed in Section 5.1.1). The rubber components had deteriorated over the lifespan of the system and were further damaged during the cleaning process, rendering the valve incapable of maintaining vacuum integrity.

The original purpose of the gate valve was to allow for a vacuum break in the upper

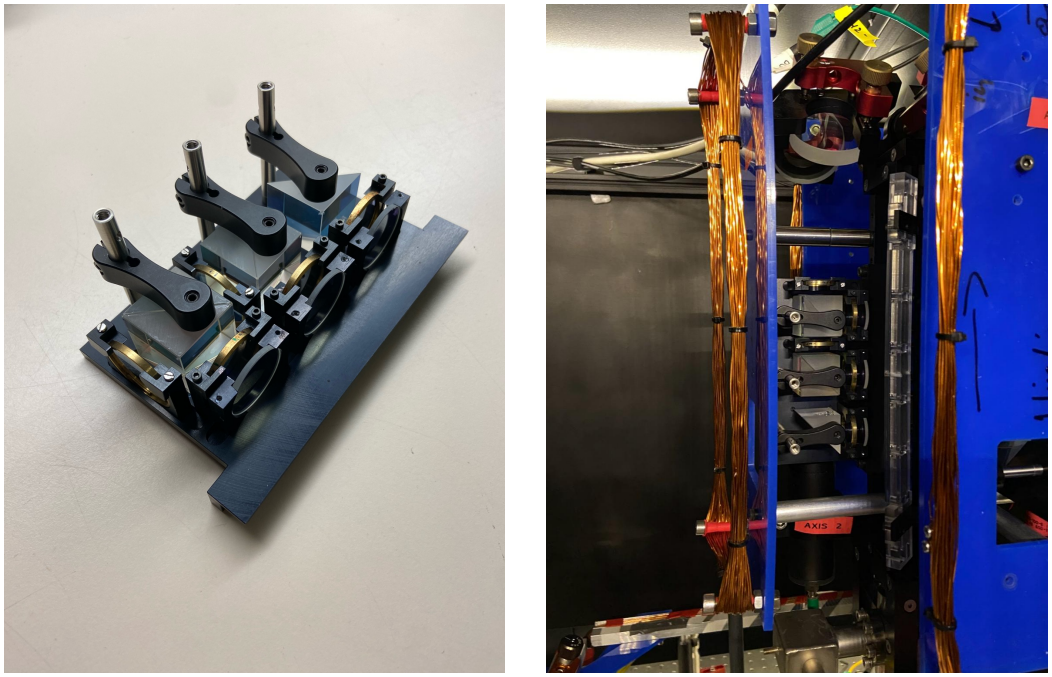

Figure 5.8: Redesigned 2D MOT lens mount shown both ex situ and in situ. **(a)** photo of completed 2D MOT optics mount showing three converging lenses and their supporting frame. This design compensates for the shortened MOT cell and it's lack of AR coating. **(b)** shows the final installed configuration, where the new mechanical supports and compact footprint accommodate the shortened MOT cell and surrounding coil structure.

chamber, enabling the replacement of rubidium dispensers once depleted without requiring a full system vacuum break [112, 113, 121]. Although this feature provided a degree of convenience, it was ultimately considered non-essential, particularly given the long lead times for replacement valves. Since the typical lifetime of the dispensers spans several years, the potential time savings of approximately one week did not justify the complexity introduced by the valve or the time lost due to long lead times on a new valve.

In place of the gate valve, a four-way cross was installed to serve as a permanent vacuum connection (Figure 5.9). This modification removed the need for a mechanical valve and simplified the vacuum layout. It also improved optical access for alignment and diagnostics. A possible future enhancement would be to incorporate a direct, horizontal temperature measurement of the atomic beam along this

section via an absorption or EIT spectrum.

The removal of the gate valve slightly reduced the overall length of the system and decreased the distance the atomic beam has to travel between the two vacuum regions. This change was not found to affect MOT loading or background pressure during operation.

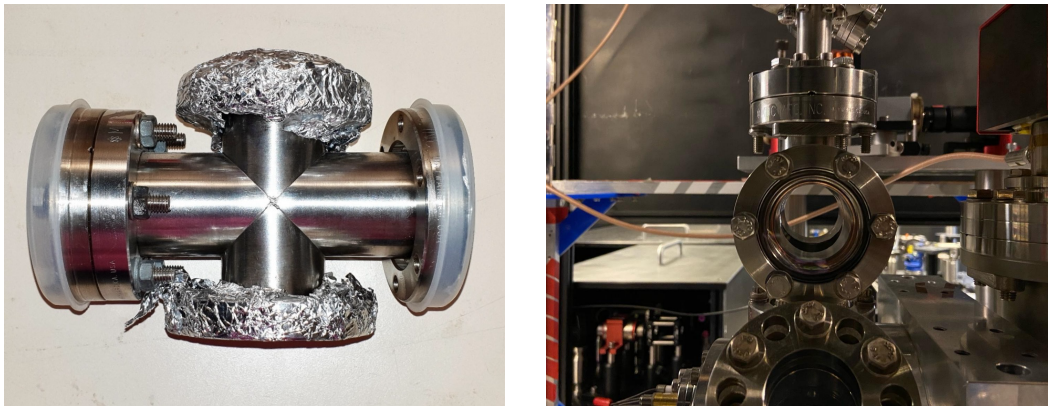

Figure 5.9: CF 4-way cross used in the vacuum system. The shortened vertical arms allow compact integration between the 2D MOT and main chamber, while the added horizontal ports enable transverse optical access. **(a)** Photograph of the CF 4-way cross. The vertical ports connect the upper 2D MOT cell to the main science chamber. The horizontal ports introduce additional optical access not available in the previous configuration. **(b)** In-situ view through the vertical axis of the CF cross, showing the unobstructed optical access provided by the horizontal ports.

Chapter 6

Characterisation of the New System

6.1 MOT Loading and Fluorescence Diagnostics

Following the modifications described in Chapter 5, in particular the replacement of the 2D MOT cell and the installation of auxiliary optics to compensate for internal reflections caused by the lack of AR coating (see Section 5.3.1.3), the 3D MOT performance was evaluated using fluorescence measurements.

The fluorescence emitted by the trapped atoms is approximately proportional to the total atom number at low optical densities, but can saturate at higher densities due to reabsorption and multiple scattering. The MOT fluorescence was collected through one of the in-vacuo aspheric lenses, as described in Chapter 3 and shown in Figure 3.5. Assuming the MOT forms at the focal point of the lens pair and that its fluorescence can be approximated as originating from a point source, the first lens collimates the emitted light. This collimated light can then be efficiently collected and focused onto a photodiode outside the chamber. The collection efficiency is set by the effective solid angle defined by the aspheric lens, which was approximately $\Omega \approx 2.1$ sr given the lens geometry and position. After collimation, the beam passed through a short lens tube assembly and was focused onto the active area

of a high gain photodiode. The overall detection efficiency includes transmission losses through the viewport and optics and the photodiode's quantum efficiency at 780 nm. All loading measurements were performed under fixed alignment and optical power conditions to ensure consistent comparison.

A typical fluorescence trace recorded during MOT loading is shown in Figure 6.1. The data were fit to the standard exponential model:

$$N(t) = N_\infty \left(1 - e^{-t/\tau}\right), \quad t \geq 0, \tag{6.1}$$

where N_∞ is the steady-state atom number (the number the MOT would load if left in perpetuity) and τ is the MOT loading time constant. From these fits the loading rate can be extracted as $R = N_\infty/\tau$.

To quantify the influence of the newly installed 2D MOT lenses (Section 5.3.1.3), loading curves were acquired at several dispenser currents, both with and without the lenses in place. The results are shown in Figure 6.2.

The data clearly demonstrate that increased dispenser current leads to faster loading and higher steady state atom numbers, as expected due to the greater flux of rubidium atoms entering the MOT region. When heated, rubidium is released from an Rb–Bi alloy within the dispenser, which activates at around 144 °C according to the manufacturer manual (AlphaVacuo). The corresponding threshold current depends on contact resistance and weld quality, so it varies between setups. Our observed onset is therefore consistent with reaching the activation temperature, though the exact current cannot be related quantitatively to the internal temperature.

More notably, the addition of the auxiliary lenses significantly improves loading across the full range of dispenser currents tested. This validates the lens installation strategy proposed in Section 5.3.1.3 to counteract reflection losses introduced by the uncoated cell and is clearly seen in the comparison of loading rates in Figure 6.3.

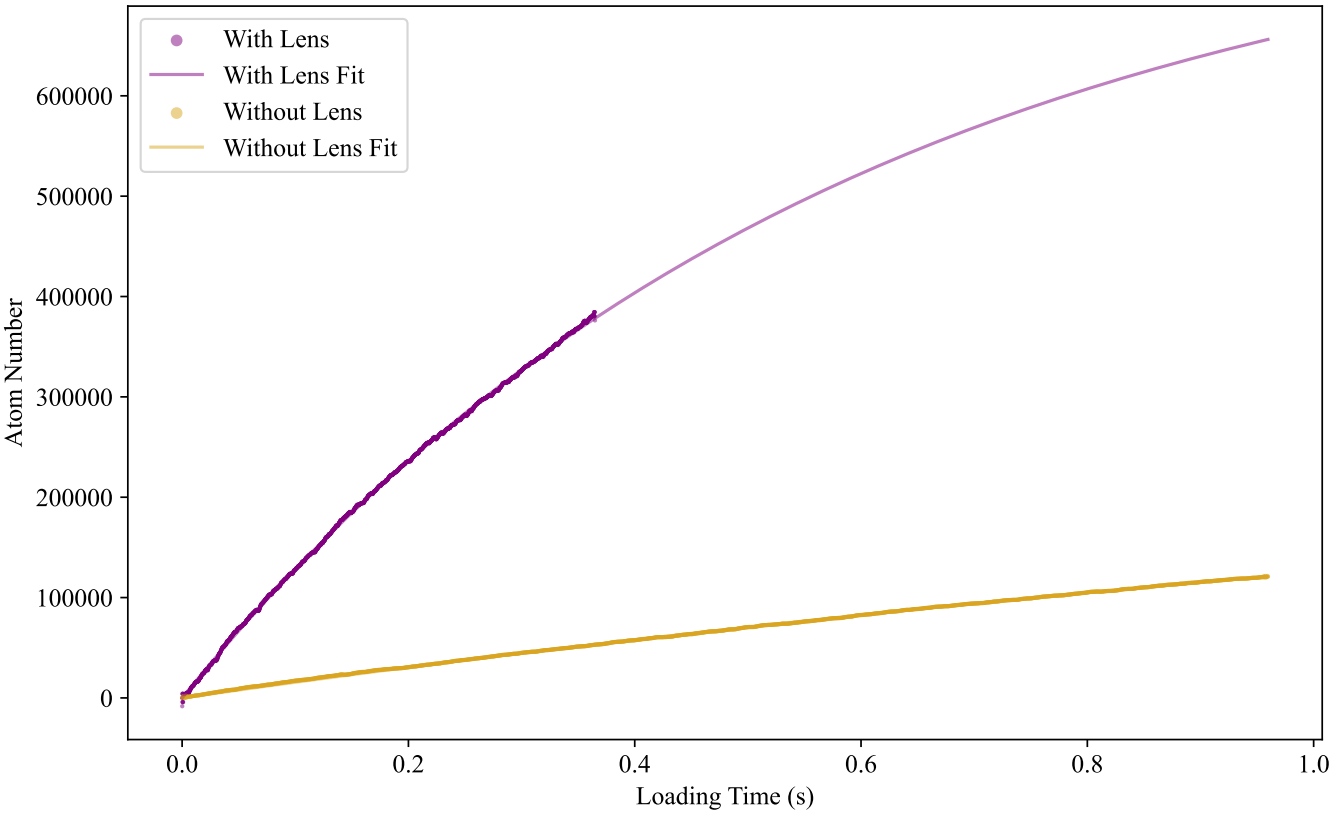

Figure 6.1: MOT loading curves showing total atom number as a function of loading time, with (purple) and without (yellow) compensating 2D MOT lenses. The curves are fit to an exponential model $N(t) = N_\infty(1 - e^{-t/\tau})$, shown as solid lines. The presence of the lenses yields both a higher steady state atom number and a faster loading time compared to the configuration without lenses, confirming improved atomic flux.

To provide a concise summary of the data, the extracted loading rates for each configuration are plotted in Figure 6.3. The loading rate increases with dispenser current in both configurations, but the enhancement from the lens system is consistent and substantial. This demonstrates the success of the optical modifications in preserving atomic flux and enhancing MOT loading efficiency.

6.2 MOT Optimisation

To characterise the spatial and density distribution of the MOT and ultimately optimise conditions for dipole trap loading, resonant absorption imaging was used.

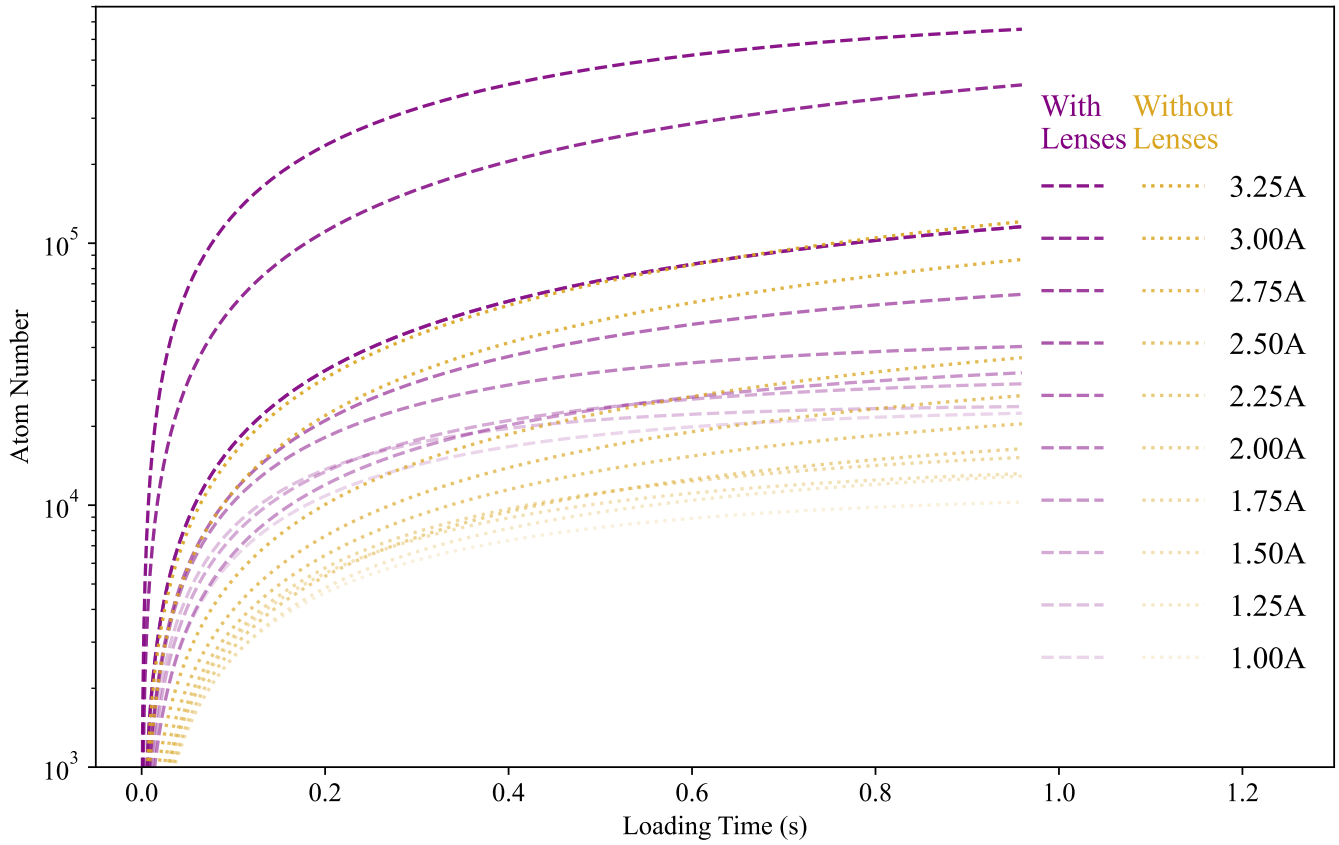

Figure 6.2: MOT loading curves at various dispenser currents (1.00–3.25 A), with (purple) and without (yellow) auxiliary 2D MOT lenses. Each curve shows the atom number as a function of loading time, measured via collected fluorescence. Atom number is presented on a logarithmic scale to highlight both initial rise and asymptotic behaviour. The presence of the lenses enhances both the loading rate and the final atom number across the full current range.

This diagnostic provides spatially resolved, quantitative measurements of the atomic column density, enabling assessment of cloud size, shape and position.

The imaging system (see Figure 3.10) consisted of a weak probe beam resonant with the $5S_{1/2} \rightarrow 5P_{3/2}$ transition, propagating along the horizontal MOT axis. The transmitted light was imaged onto a Andor Luca CCD camera using a calibrated 4f system. A series of 200 images, alternating between with and without atoms to establish an average signal and average background, was used to generate the Optical Depth (OD):

$$\mathrm{OD}(x, y) = -\ln\left[\frac{I(x, y)}{I_0(x, y)}\right], \tag{6.2}$$

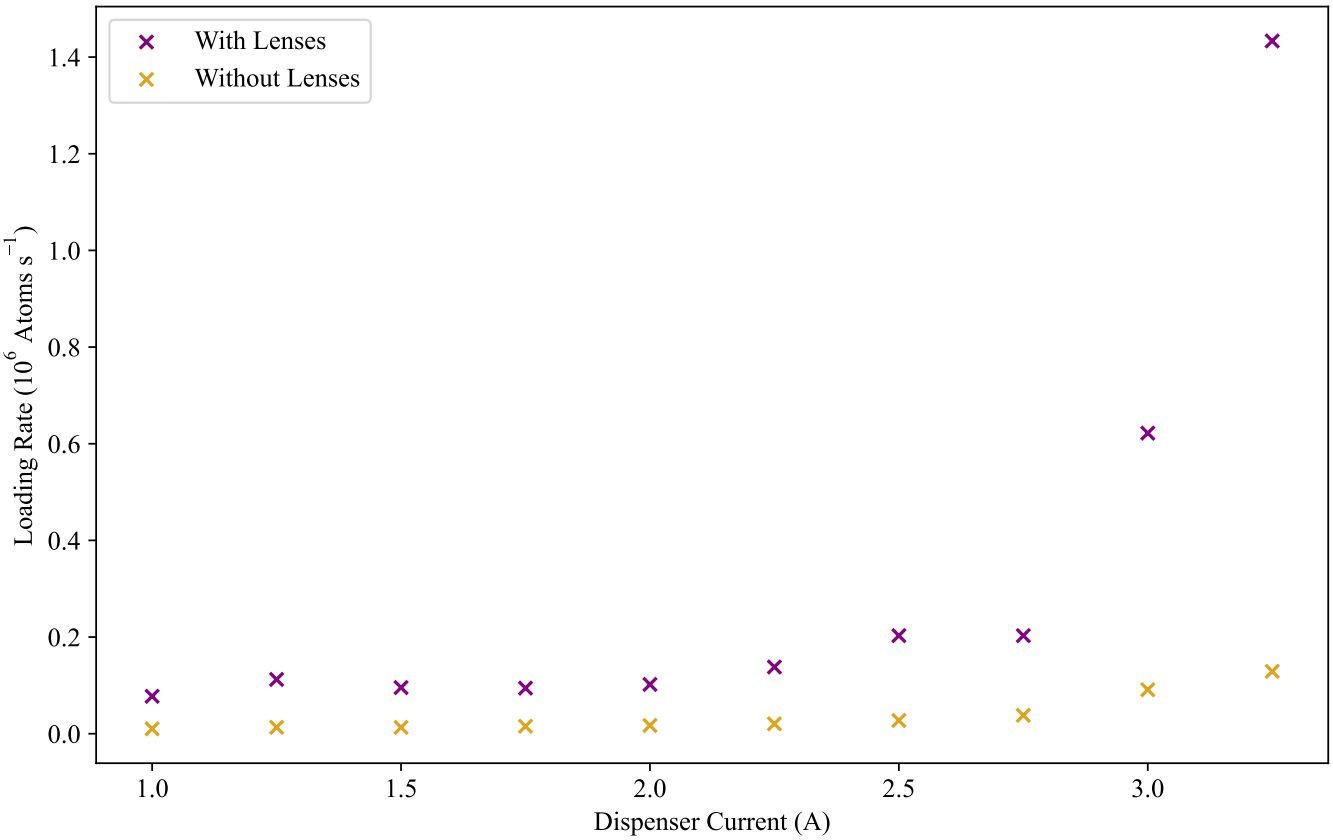

Figure 6.3: Extracted MOT loading rates as a function of dispenser current, with (purple) and without (yellow) auxiliary 2D MOT lenses. Each data point was derived from exponential fits to fluorescence loading curves (Figure 6.2), using $R = N_\infty/\tau$. The lens configuration consistently yields higher loading rates across the full range of dispenser settings, demonstrating the success of the optical modification in improving atomic beam collimation and enhancing MOT capture efficiency.

where $I(x, y)$ and $I_0(x, y)$ are the probe images with and without atoms, respectively. This was used to extract both the atom number and the cloud position.

Beyond static characterisation, absorption imaging also enabled measurement of the cloud temperature via TOF balistic expansion. By allowing the cloud to freely expand after release from the MOT and tracking its increasing size over time, the temperature is extracted by fitting the time dependence of the Gaussian width (standard deviation) $\omega(t)$:

$$\omega(t) = \sqrt{\omega_0^2 + \frac{k_B T}{m} t^2}, \tag{6.3}$$

where ω_0 is the width at release, T is the cloud temperature in kelvin, k_B is the Boltzmann constant and m is the mass of a ^{87}Rb atom.

A typical series of processed images for TOF calculation is shown in Figure 6.4. Additionally, the imaging system proved invaluable in tuning the compensation coil currents. By observing the MOT position and symmetry under various magnetic field configurations, residual stray fields could be cancelled and field zeroes optimised for efficient atom capture and transfer.

6.2.1 Displacement Based Compensation Field Optimisation

Precise alignment of the MOT at the magnetic field zero is critical for implementing advanced cooling techniques, such as compressed MOT and optical molasses and for ensuring reliable overlap with the dipole trap. This requires cancelling both the Earth's magnetic field and ambient stray fields using three orthogonal pairs of compensation coils. However, due to the non-ideal geometry of the setup, the coils do not form perfect Helmholtz configurations and each pair introduces residual fields along the other axes. Consequently, the cancellation process is inherently coupled and must be approached iteratively [140].

The optimisation strategy aimed to maintain the MOT position while varying the quadrupole field gradient. If the compensation is not correctly tuned, the MOT position shifts as the quadropole field zero moves with changing gradient. To identify the optimal compensation current for a given axis, we performed a series of measurements using absorption imaging to track the MOT position while scanning the compensation current for several fixed quadrupole gradients. This is necessary for the CMOT since if we move the position of the MOT while compressing it results in additional heating.

For example, in the east–west and vertical directions, a set of MOT positions was recorded as a function of compensation current at multiple quadrupole gradients. The optimal compensation current was identified at the intersection point of the

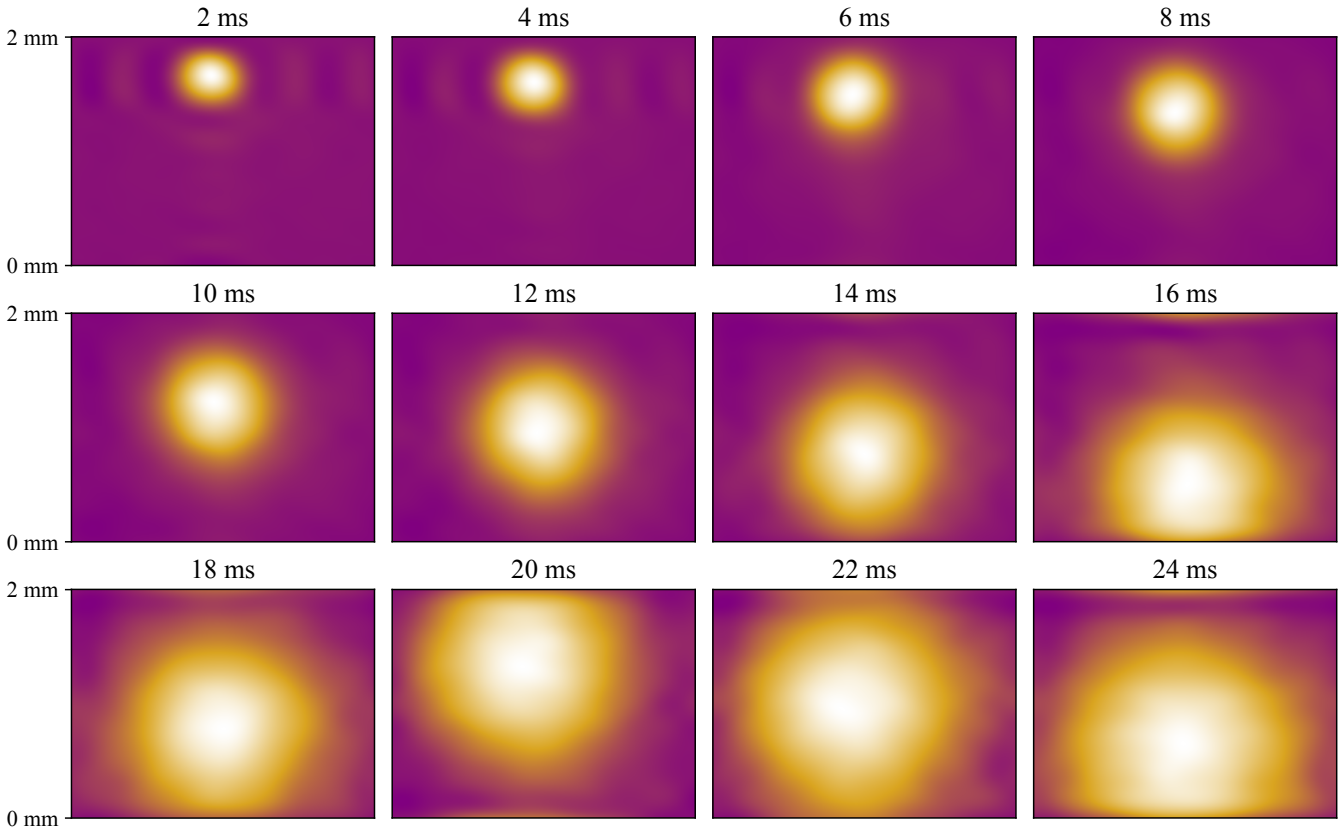

Figure 6.4: Typical absorption images of the atomic ensemble taken at increasing TOF durations after release from the 3D MOT. Each image corresponds to a different TOF, increasing from 2 ms to 24 ms in 2 ms steps (left to right, top to bottom). During free expansion, the atomic cloud falls under gravity and expands due to its initial thermal velocity distribution. The vertical displacement of the cloud in early frames reflects gravitational acceleration, while the later images have been recentered to maintain the cloud in view. From the measured displacement of the cloud centre between 2 ms and 16 ms, the inferred acceleration is $10.8\,\mathrm{m\,s^{-2}}$, this deviation is likely due to a slight mispositioning of our imaging lenses or residual stray magnetic fields. Each image represents an average over 100 experimental runs to improve the signal-to-noise ratio. These images are used to extract temperature and expansion rates of the ensemble by fitting 2D Gaussian profiles to the atomic density distributions as a function of time.

resulting MOT position curves. This corresponds to the true magnetic field zero for that axis. An example result is shown in Figure 6.5.

The north–south direction presented greater challenges due to the absence of an imaging axis along that direction. A temporary workaround was implemented using a upward looking camera that displays MOT fluorescence in real time on a

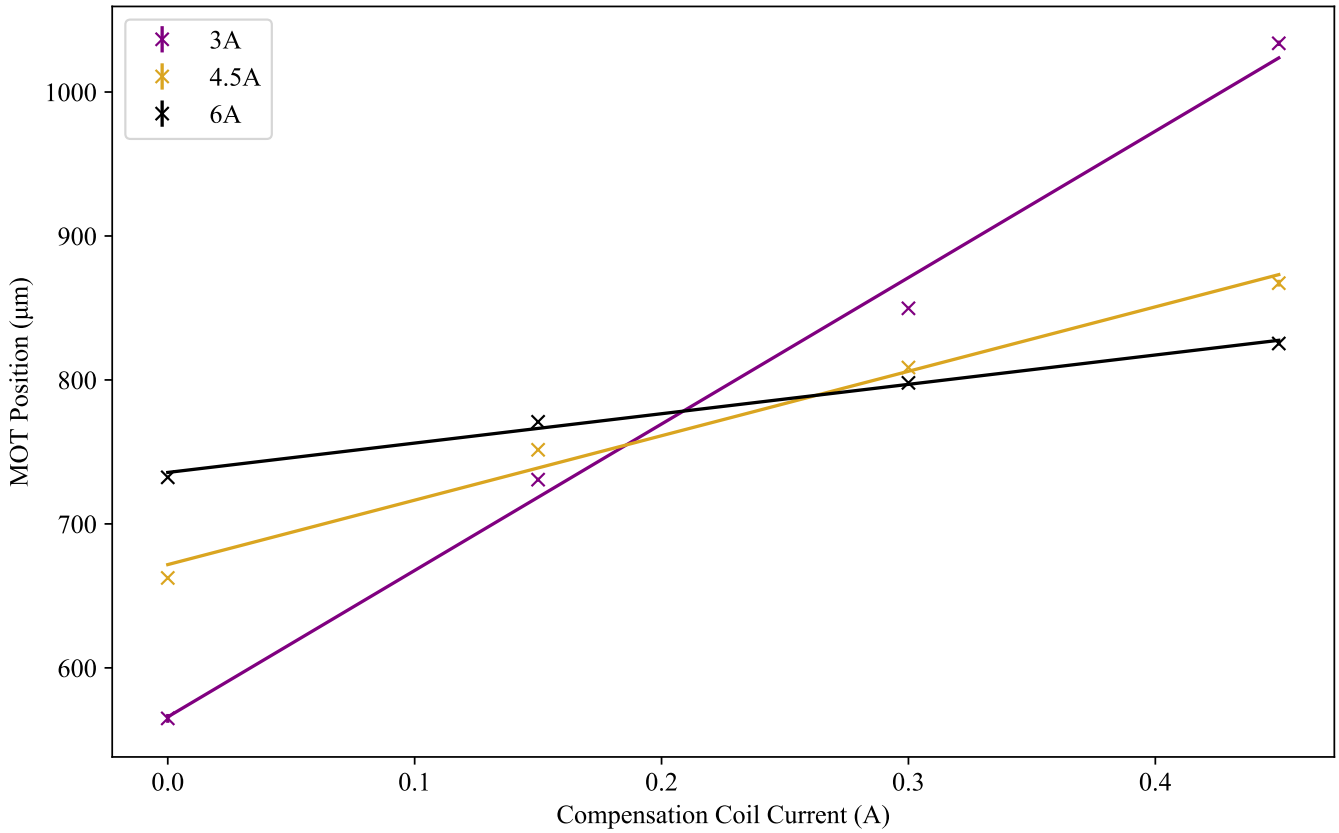

Figure 6.5: Measured MOT position along the vertical axis as a function of vertical compensation coil current, for three different quadrupole field gradients (3 A, 4.5 A, 6 A). The intersection point of the lines indicates the optimal compensation setting that keeps the MOT centred regardless of gradient, corresponding to a magnetic field zero along the vertical axis.

monitor. Displacements were measured with too larger uncertainties and is not suitable for precise optimisation.

6.2.2 Temperature-Based Compensation Field Optimisation

While the east–west and vertical compensation currents were initially determined by locating the magnetic field zero using position measurements (Section 6.2.1), the lack of optical access along the north–south axis necessitated an alternative approach. Rather than relying on direct imaging, we exploited the sensitivity of the atomic cloud's temperature to shifts in the magnetic field zero changing suddenly.

In the ideal case, the MOT remains centred at the magnetic field zero regardless

of the quadrupole field gradient. However, if the compensation field is incorrectly tuned, the field zero shifts with changing quadrupole gradient, resulting in the atomic ensemble being effectively 'shaken', which leads to heating. We implemented a sequence that abruptly switched between different quadrupole gradients (by changing the MOT coil currents). At each compensation coil current setting, the MOT temperature was recorded by releasing the cloud and measuring its expansion after 4 ms of time of flight using absorption imaging.

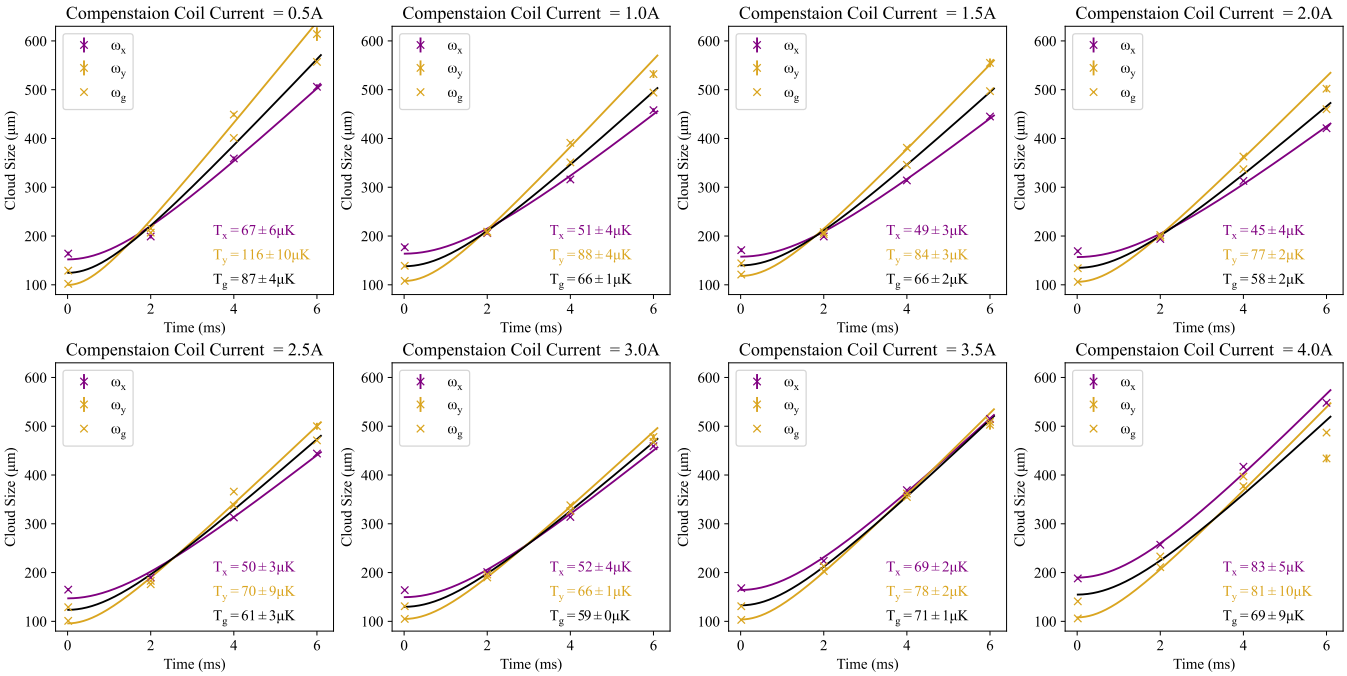

Figure 6.6: Mosaic of TOF graphs with expansion times between 0-4 ms, at different N-S compensation coil currents. These graphs were used to extract temperatures shown in Figure 6.7(a). The MOT size increases with temperature, allowing quantitative thermal analysis in the x (purple) and y (yellow) dimensions and the geometric mean of them (g, black) via Gaussian fitting.

The optimal set of compensation currents was identified as the one that showed the lowest temperature following the sudden switching sequence, under the assumption that this corresponds to minimal displacement of the magnetic field zero.

To mitigate cross-axis coupling caused by the imperfect Helmholtz geometry of the compensation coils, this procedure was repeated iteratively using the currents from the last measurement on the other two axes. It was decided this method produced

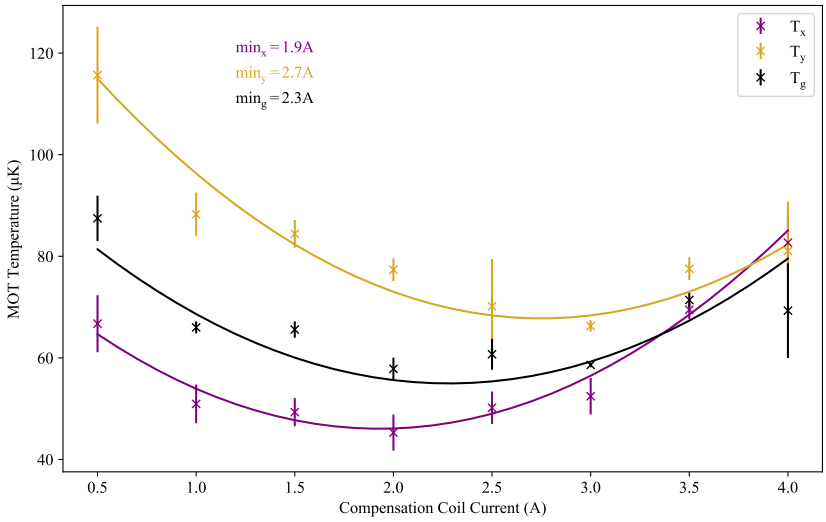

(a) Initial scan of MOT temperature versus N-S compensation coil current. Temperatures were extracted from 4 ms TOF expansion data (see Figure 6.6).

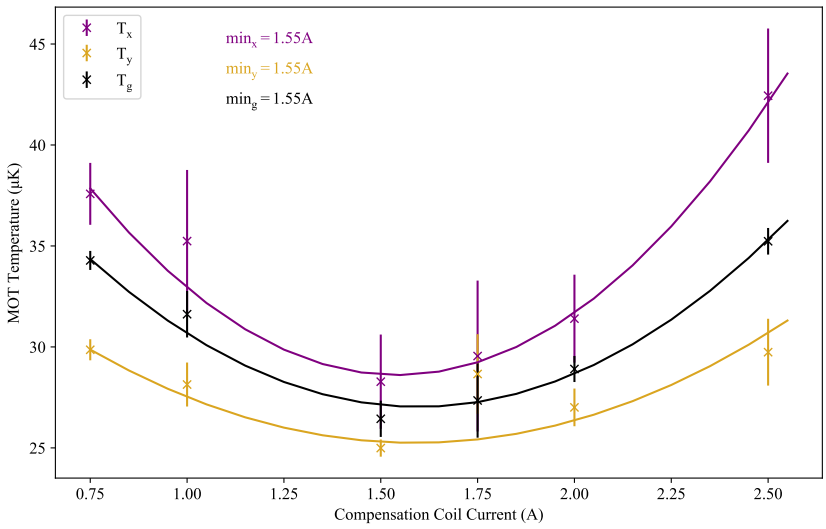

(b) Second scan following application of refined shim settings from (a). The convergence of temperature minima across all three curves confirms improved alignment of the magnetic field zero.

Figure 6.7: Optimisation of the N-S compensation coil current via temperature-based diagnostics. A sequence of sudden MOT gradient changes was used to sensitively probe residual magnetic field misalignment. The temperature minima indicate effective field zeroing. Iterating this process from scan (a) to (b) reduced cross-axis offsets introduced by the imperfect compensation coil geometry. Temperatures were measured in the x (purple) and y (yellow) directions and their geometric mean (black, "g").

better results than the conventional displacement based optimisation, so we used it for all three axes, using the results from Section 6.2.1 as a starting point.

Following this, the optical molasses stage was optimised by adjusting ramp times, beam power and detuning. The resulting measured temperature after the full sequence (shown in Figure 3.7 was $12.8 \pm 0.5\mu$K (Figure 6.8). This was taken as evidence that the magnetic field zero had been reliably centred at the MOT location in all three dimensions, completing the field alignment process and preparing the system for dipole trap loading.

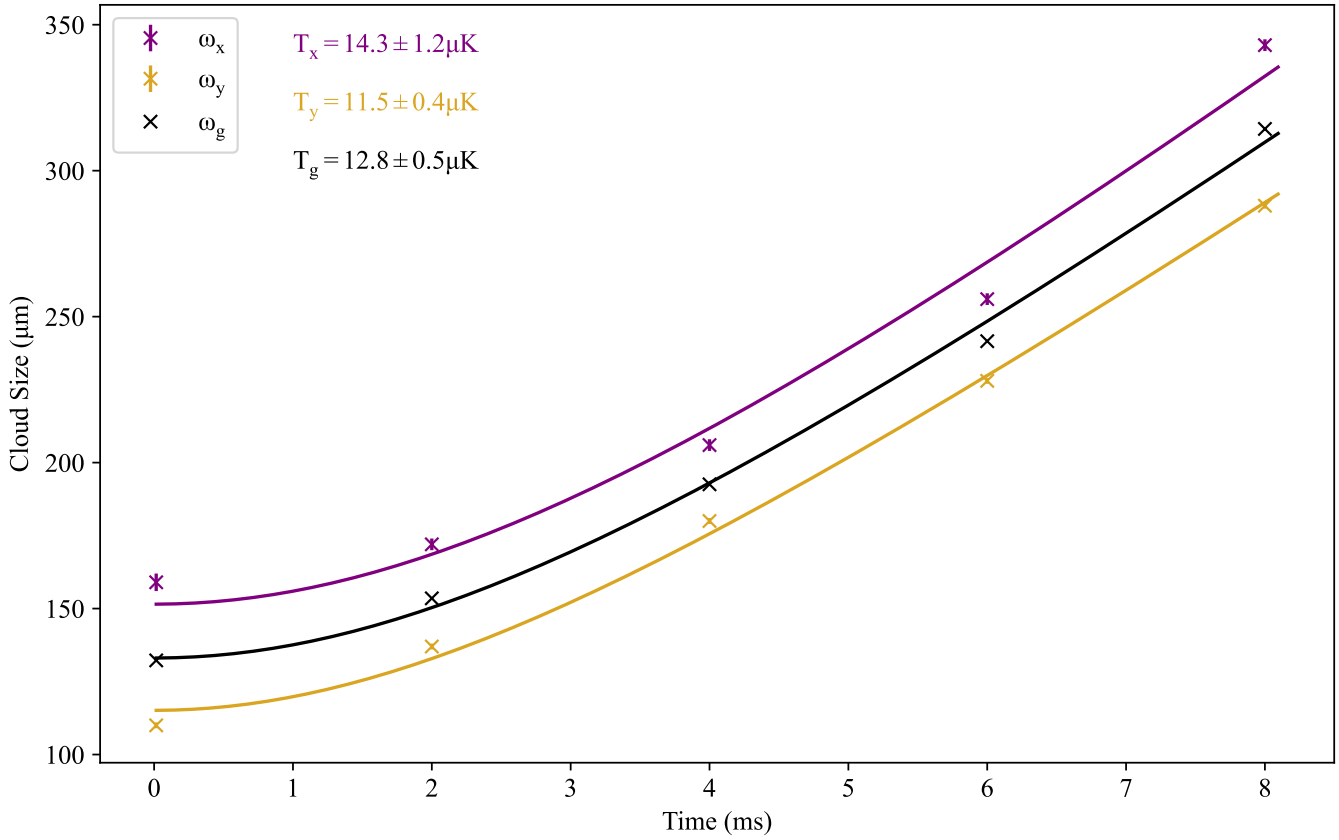

Figure 6.8: TOF temperature measurement after optical molasses cooling. Expansion along two orthogonal axes was recorded and fit to Gaussian models, yielding temperatures of $T_x = 14.3 \pm 1.2\mu$K, $T_y = 11.5 \pm 0.4\mu$K and a geometric mean $T_g = 12.8 \pm 0.5\mu$K. The result confirms effective magnetic field compensation and good molasses parameters.

6.3 Dipole Trap Loading and Spatial Alignment Constraints

A critical step towards producing high density, cold atomic ensembles is the efficient loading of the dipole trap. This requires precise spatial overlap between two key, but physically immovable, components of the system: the magnetic field zero of the quadrupole and the optical focus of the in-vacuo aspheric lens pair.

(1) Unique field zero: There exists only one spatial location where the magnetic field can be zeroed for all quadrupole field gradients using fixed compensation currents. This "true" zero point is defined by the geometric centre of the in-vacuo MOT coils. It is the only location where the field remains consistently zero throughout all MOT stages: loading, compression and optical molasses.

(2) Cooling sensitivity: Cooling schemes such as CMOT, optical molasses and PGC are particularly sensitive to residual magnetic fields. If the magnetic field zero shifts with changing gradient strength, the atoms experience unwanted forces that result in heating; an effect confirmed experimentally.

(3) Fixed trap location: The dipole trap forms at the optical focus of a beam delivered through the aspheric lens system (see Section 3.3.2.2). This focus defines the only point where a stable, tightly confining trap can form. Since both the lenses and the MOT coils are mounted inside the vacuum chamber, their relative positions are fixed after assembly. The fixed geometry constrains the possible overlap between the trap focus and the magnetic field zero (see Figure 3.5).

(4) Limited adjustability: Minor tuning of either the magnetic field zero (via compensation coil currents) or the dipole trap position (by slightly defocusing the trapping beam) is possible. However, these adjustments degrade performance. Misalignment reduces trap quality, disrupts probe and coupling beam overlap and impedes detection on the SAPDs without further modifications.

(5) Misalignment discovered: During characterisation, it was found that the

true magnetic field zero and the dipole trap focus did not coincide. The required combination of compensation coil offsets and beam shaping exceeded acceptable limits. Although trap fluorescence was detected (see Figure 6.9), no significant optical density was observed. This misalignment likely resulted from a small spatial shift (on the order of 500 μm) introduced during vacuum chamber reassembly (see Chapter 5).

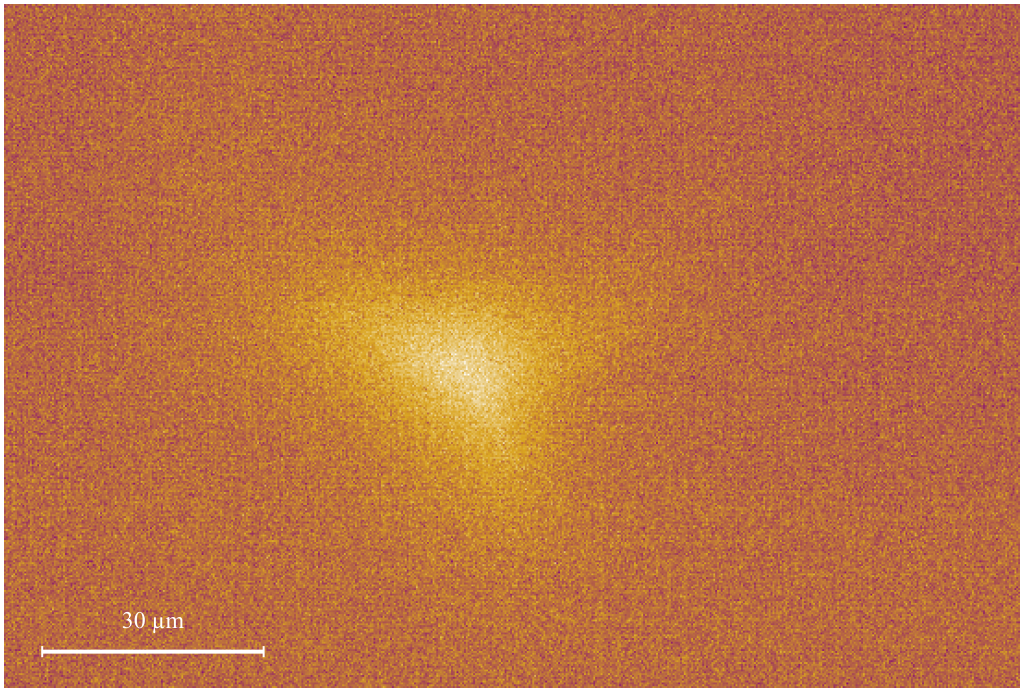

Figure 6.9: Fluorescence image of the dipole trap prior to implementation of dynamic compensation field control. Although atoms are successfully loaded, the fluorescence signal appears broader than expected. This is due to the combined effects of an intentionally deformed trapping beam (required to achieve overlap with the MOT) and imaging along the trap's longitudinal axis. Since the trap length exceeds the imaging system's depth of focus, the resulting image is intrinsically blurred. Despite this, fluorescence remains a useful diagnostic for confirming trap loading and general spatial alignment. The image was processed using the same background subtraction and normalisation methods described for absorption imaging in Section 6.2.

(6) Dynamic solution: To resolve the misalignment, a switchable compensation coil system was implemented. This enabled dynamic compensation of residual fields to ensure of the magnetic field zero is aligned to the dipole trap location during MOT loading, compression and molasses stages. The full sequence is described in

Chapter 3 and illustrated in Figure 3.7. This ensured both spatial overlap and consistent field cancellation throughout.

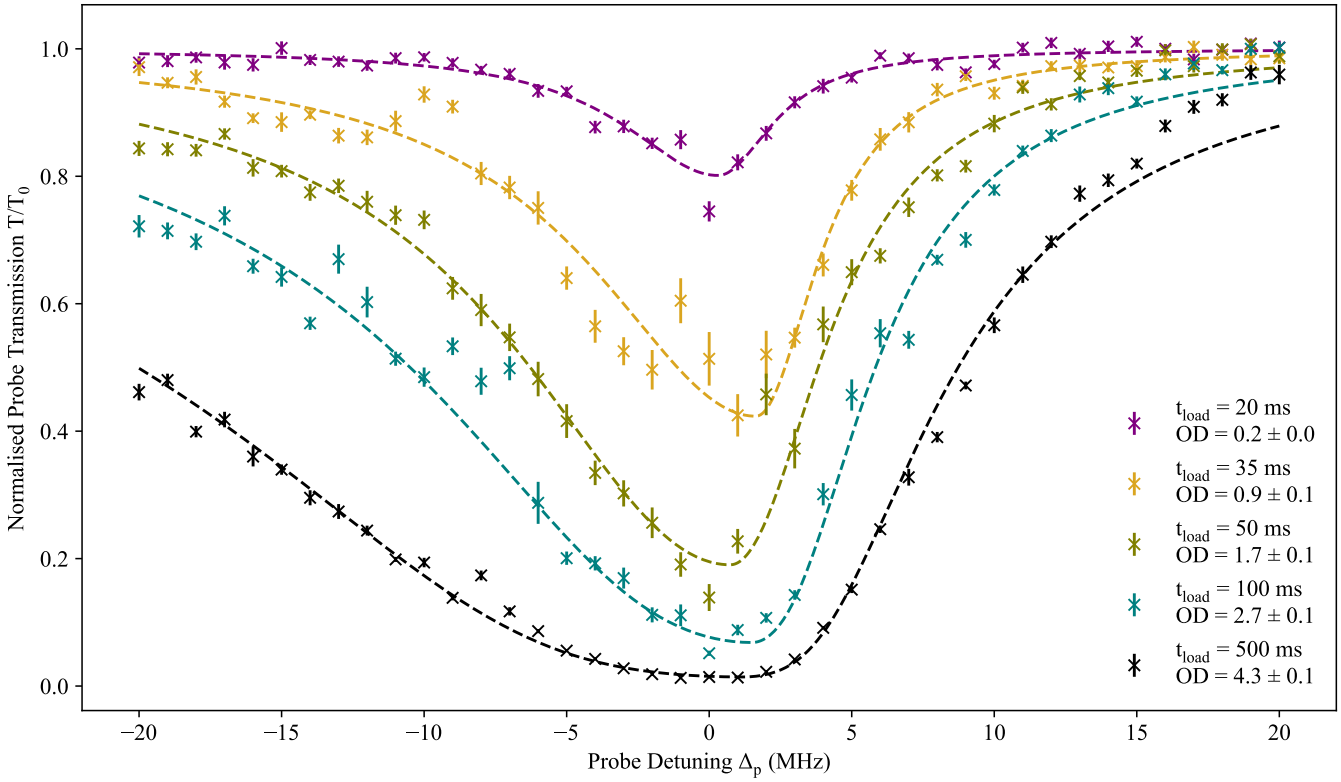

Figure 6.10: Optical depth measurement in the optimised configuration. The transmission spectra were fit using a Lorentzian model with OD dependent linewidth and an empirical asymmetry term. The fitted OD values and uncertainties are indicated in the legend. This data set was taken by Karen Wadenpfuhl and Aaron Reinhard.

(7) Successful outcome: With this upgrade, robust dipole trap loading was achieved. To quantitatively assess the optical depth (OD) of the ensemble, transmission spectra were fit using a Lorentzian absorption model with both broadening and asymmetry introduced phenomenologically to account for density-dependent and interaction-driven effects.

The transmission was modelled as

$$T(\Delta) = \exp\left[-\frac{\mathrm{OD}_0}{1+4\left(\frac{\Delta-\Delta_0}{\Gamma(\Delta)}\right)^2}\right], \tag{6.4}$$

where Δ is the probe detuning, Δ_0 is the resonance centre and OD_0 is the optical depth at resonance. The detuning-dependent linewidth $\Gamma(\Delta)$ is defined as:

$$\Gamma(\Delta) = \begin{cases} \Gamma_0 + \beta \cdot \mathrm{OD}_0 \cdot (1 - \alpha), & \text{if } \Delta < \Delta_0 \\ \Gamma_0 + \beta \cdot \mathrm{OD}_0 \cdot (1 + \alpha), & \text{if } \Delta \geq \Delta_0 \end{cases}$$

Here, $\Gamma_0 = 6.06\,\mathrm{MHz}$ is the natural linewidth of the ^{87}Rb D_2 transition. The coefficient β accounts for density-dependent self-broadening due to resonant dipole–dipole interactions [141]. The asymmetry parameter α is an empirical addition introduced in this work to capture the skew observed in the transmission spectra at higher densities. α effectively parameterises any resulting effects that generate asymmetry between the red and blue wings. Additional contributions to the skew could also arise from reabsorption within the optically thick cloud or residual magnetic field gradients.

While this specific functional form is not derived from microscopic theory, it provides a compact and effective means of characterising the lineshape. Similar asymmetries and shifts are known to arise from the optical dipole–dipole interaction [141], although a rigorous treatment would require integration over all pairwise Doppler and dipolar couplings, beyond the scope of this work.

This model assumes that for a fixed geometry and resonant cross-section, the on-resonance optical depth scales linearly with atomic number density, $\mathrm{OD}_0 \propto N$.

The fitted optical depths, shown in Figure 6.10, reached values up to OD $\sim 4.3 \pm 0.1$ in the optimised configuration. The results are comparable to previous system performance, validating the upgrade strategy and confirming effective loading into the tightly focused dipole trap.

Chapter 7

Conclusion and Outlook

This thesis has presented the reconstruction, characterisation and application of a cold atom experimental platform for investigating coherent dynamics and single photon control in Rydberg blockaded ensembles. By making use of precision trapping, narrow linewidth laser excitation, microwave control and single photon detection, we demonstrated the coherent manipulation of a collectively encoded Rydberg qutrit and developed tools that establish the groundwork for future quantum information and quantum optics experiments.

7.1 Summary of Contributions

The theoretical framework underpinning the work was developed around driven two and three level atomic systems, with particular focus on ladder type configurations supporting Rydberg dark state polaritons under EIT conditions. The exaggerated properties of high principal quantum number Rydberg states, including large dipole moments and strong van der Waals interactions, were identified as key mechanisms enabling optical nonlinearities, photon–photon interactions and single photon production. In particular, the Rydberg blockade effect, whereby strong interactions prevent multiple simultaneous excitations within a blockade radius, was investigated as the central mechanism for collective encoding and non-classical

light generation.

The experimental platform was restored following a vacuum failure and modified to improve optical access and maintain UHV compatibility. This included replacement of the 2D MOT cell, the addition of compensating optics and reconfiguration of the vacuum architecture. Detailed procedures for cleaning, reassembly, evacuation and dispenser activation were carried out to ensure a high-quality vacuum and reproducible system performance.

A key methodological contribution was the development and application of a temperature based optimisation technique to identify the true zero of the quadrupole magnetic field. By monitoring heating induced by abrupt gradient changes and iteratively adjusting compensation coil currents, optimal magnetic-field alignment was achieved, maximising the stability of the MOT, reducing heating and ensuring reliable overlap with the dipole trap and probe beam. On this foundation, MOT temperatures below 15 μK were achieved and a high-density dipole-trapped ensemble was prepared.

Finally, a collectively encoded Rydberg qutrit was realised and characterised using microwave fields to couple between three Rydberg levels. A time-resolved sequential readout protocol allowed population in each qutrit basis state to be independently measured, and a Ramsey interferometric sequence confirmed coherence and phase-dependent interference consistent with multilevel unitary evolution.

These contributions, together with the developed methods, position the experiment as a promising platform for the next generation of quantum optics and quantum information experiments.

7.2 Impact and Significance

The work presented here demonstrates the transition of the experiment from recovery and reconfiguration to a mature platform capable of coherent multilevel

control. The apparatus now routinely produces cold, dense atomic ensembles with reliable dipole trap loading and single-photon detection, establishing the technical foundation required for exploring strongly interacting quantum optics.

The collectively encoded Rydberg qutrit realised in this work represents a step toward extending Rydberg blockade physics beyond binary qubit operation into a controlled multilevel regime. By coherently addressing and reading out three Rydberg states, the experiment demonstrates that coherent population transfer and phase dependent interference can be achieved within a three level manifold.The measured coherence and reproducibility indicate that such systems can support multilevel control sequences on microsecond timescales, consistent with the timescale of their coherence. These results are a step towards collectively encoded Rydberg qutrits as a platform for exploring multilevel QIP and hybrid photonic–atomic schemes.

The temperature based magnetic field alignment technique developed here constitutes a broadly applicable methodology. It provides a reliable means of identifying the magnetic field zero through measurable thermal responses rather than direct imaging, offering a robust and transferable approach for MOT optimisation where optical access is limited. Its implementation was central to achieving sub-Doppler temperatures, stable trap alignment, and high optical depth in the present apparatus.

Taken together, these developments transform the system from a re-established cold atom setup into a flexible, high-performance platform for investigating photon–photon interactions, nonlinear optical phenomena, and multilevel quantum logic.

7.3 Outlook

With sub-15 μK atom temperatures, reliable dipole trap loading, and single photon sensitive detection now re-established, the apparatus has transitioned from the characterisation phase to the regime of strongly interacting quantum optics. This

enables new experiments, such as the study of photon–photon correlations, interaction induced phase shifts, and multilevel coherence in Rydberg ensembles.

The system developed here serves as a versatile platform for exploring strongly interacting quantum optics, and a number of near term and longer term goals can now be pursued:

- **FORT Characterisation and Optimisation**: As outlined in Chapter 6, the spatial mismatch between the MOT field zero and the dipole trap focus was dynamically compensated. Future work should focus on reoptimising trap geometry and loading sequences to maximise loading rates and optical depth, which are crucial for achieving higher density samples and more precise control over the interaction dynamics.

- **Photon Correlation Measurements**: The improved control of atomic density and laser stability achieved in this work will enable precise measurements of the second-order correlation function $g^{(2)}(0)$. This will serve as a benchmark for single-photon emission and provide a deeper understanding of photon blockade phenomena, enabling investigations of both quantum light sources and quantum nonlinearities [34, 48].

- **Two-Channel Rydberg Configuration**: Building on previous architectures, a reimplementation of a two-channel system in which two non-interacting Rydberg states can be made to interact via **microwave or THz dressing fields**. This would allow tunable interactions between spatially separated polaritons and forms the basis for implementing photon–photon gates and interaction based protocols, thus advancing towards more complex QIPs [110, 142, 143].

- **Hong–Ou–Mandel Interference with Rydberg Photons**: A long-term ambition is to realise a Hong-Ou-Mandel (HOM) experiment [144] using two independently stored and retrieved Rydberg polaritons. By synchronising

storage times, the HOM dip would provide a test of photon indistinguishability, coherence, and interaction effects at the single excitation level.

7.4 Final Remarks

The experimental system presented in this thesis demonstrates the ability to coherently control, manipulate, and read out single Rydberg excitations in a cold atomic ensemble. The temperature based compensation field optimisation method, the state-selective qutrit retrieval scheme, and the photon counting diagnostics collectively establish a robust framework for advanced quantum optics experiments.

The results presented here represent a step towards realising multilevel QIP in neutral atom systems. The successful demonstration of a collectively encoded Rydberg qutrit has shown that Rydberg states can be coherently controlled within a three level Hilbert space, shows a promising direction for more complex multilevel gate protocols. These qutrits offer a pathway to higher dimensional quantum systems, which could be useful for scaling up quantum information tasks beyond the binary qubit.

Future work will build on these capabilities to engineer interactions between independent Rydberg excitations, implement gate protocols in higher dimensional state spaces, and probe the quantum statistics of light at the single photon level. The combination of cold atom coherence, strong Rydberg interactions, and high efficiency detection positions this platform to contribute significantly to the development of hybrid photonic–atomic quantum information technologies.

Though technical challenges remain, the work presented here provides a solid foundation and give reason to be optimistic. The system is now well positioned to explore quantum optics effects, investigate photon–photon interactions, and continue evolving into a precise, flexible tool for quantum optics experiments.

Bibliography

[1] Yuechun Jiao, Nicholas L. R. Spong, Oliver D. W. Hughes, Chloe So, Teodora Ilieva, Kevin J. Weatherill, and Charles S. Adams. Single-photon stored-light Ramsey interferometry using Rydberg polaritons. *Opt. Lett.*, 45(20):5888–5891, Oct 2020. doi: 10.1364/OL.405143. URL https://opg.optica.org/ol/abstract.cfm?URI=ol-45-20-5888.

[2] Nicholas L. R. Spong, Yuechun Jiao, Oliver D. W. Hughes, Kevin J. Weatherill, Igor Lesanovsky, and Charles S. Adams. Collectively Encoded Rydberg Qubit. *Phys. Rev. Lett.*, 127:063604, Aug 2021. doi: 10.1103/PhysRevLett.127.063604. URL https://link.aps.org/doi/10.1103/PhysRevLett.127.063604.

[3] Yuechun Jiao, Oliver D. W. Hughes, Max Z. Festenstein, Zhengyang Bai, Jianming Zhao, Weibin Li, Kevin J. Weatherill, and C. Stuart Adams. Single photonic qutrit in a collective Rydberg polariton, Sep 2025. URL https://link.aps.org/doi/10.1103/3xnw-cpj2.

[4] M. Planck. On the Law of Distribution of Energy in the Normal Spectrum. *Annalen der Physik*, 4:553–562, 1901. doi: 10.1002/andp.19013090310. URL https://doi.org/10.1002/andp.19013090310.

[5] A. Einstein. Über einen die Erzeugung und Verwandlung des Lichtes betreffenden heuristischen Gesichtspunkt. *Annalen der Physik*, 322(6):132–148, 1905. doi: https://doi.org/10.1002/andp.19053220607. URL https://onlinelibrary.wiley.com/doi/abs/10.1002/andp.19053220607.

[6] E. Schrödinger. An Undulatory Theory of the Mechanics of Atoms and Molecules. *Phys. Rev.*, 28:1049–1070, Dec 1926. doi: 10.1103/PhysRev.28.1049. URL https://link.aps.org/doi/10.1103/PhysRev.28.1049.

[7] N. Bohr. I. On the constitution of atoms and molecules. *The London, Edinburgh, and Dublin Philosophical Magazine and Journal of Science*, 26(151): 1–25, 1913. doi: 10.1080/14786441308634955. URL https://doi.org/10.1080/14786441308634955.

[8] W. Heisenberg. Über quantentheoretische Umdeutung kinematischer und mechanischer Beziehungen. *Zeitschrift für Physik*, 33:879–893, 1925. doi: 10.1007/BF01328377. URL https://doi.org/10.1007/BF01328377.

[9] P. A. M. Dirac. The quantum theory of the emission and absorption of radiation. *Proceedings of the Royal Society of London. Series A, Containing Papers of a Mathematical and Physical Character*, 114:243–265, 1927. doi: 10.1098/rspa.1927.0039. URL http://doi.org/10.1098/rspa.1927.0039.

[10] Serge Haroche. Nobel Lecture: Controlling photons in a box and exploring the quantum to classical boundary. *Reviews of Modern Physics*, 85(3):1083–1102, 2013. doi: 10.1103/RevModPhys.85.1083. URL https://doi.org/10.1103/RevModPhys.85.1083.

[11] Rodney Loudon. *The Quantum Theory of Light*. Oxford University Press, New York, 3rd edition, 2000. ISBN 9780198501772.

[12] Claude Cohen-Tannoudji. Laser cooling and trapping of neutral atoms: theory. *Physics Reports*, 219(3):153–164, 1992. ISSN 0370-1573. doi: https://doi.org/10.1016/0370-1573(92)90133-K. URL https://www.sciencedirect.com/science/article/pii/037015739290133K.

[13] A. L. Schawlow and C. H. Townes. Infrared and Optical Masers. *Phys. Rev.*, 112:1940–1949, Dec 1958. doi: 10.1103/PhysRev.112.1940. URL https://link.aps.org/doi/10.1103/PhysRev.112.1940.

[14] Charles H. Townes. Production of Coherent Radiation by Atoms and Molecules. *Science*, 149(3686):831–841, 1965. doi: 10.1126/science.149.3686.831. URL https://www.science.org/doi/abs/10.1126/science.149.3686.831.

[15] E. L. Raab, M. Prentiss, Alex Cable, Steven Chu, and D. E. Pritchard. Trapping of Neutral Sodium Atoms with Radiation Pressure. *Phys. Rev. Lett.*, 59:2631–2634, Dec 1987. doi: 10.1103/PhysRevLett.59.2631. URL https://link.aps.org/doi/10.1103/PhysRevLett.59.2631.

[16] William D. Phillips. Nobel Lecture: Laser cooling and trapping of neutral atoms. *Rev. Mod. Phys.*, 70:721–741, Jul 1998. doi: 10.1103/RevModPhys.70.721. URL https://link.aps.org/doi/10.1103/RevModPhys.70.721.

[17] J. Dalibard and C. Cohen-Tannoudji. Laser cooling below the Doppler limit by polarization gradients: simple theoretical models. *J. Opt. Soc. Am. B*, 6(11):2023–2045, Nov 1989. doi: 10.1364/JOSAB.6.002023. URL https://opg.optica.org/josab/abstract.cfm?URI=josab-6-11-2023.

[18] Paul D. Lett, Richard N. Watts, Christoph I. Westbrook, William D. Phillips, Phillip L. Gould, and Harold J. Metcalf. Observation of Atoms Laser Cooled below the Doppler Limit. *Phys. Rev. Lett.*, 61:169–172, Jul 1988. doi: 10.1103/PhysRevLett.61.169. URL https://link.aps.org/doi/10.1103/PhysRevLett.61.169.

[19] Wolfgang Ketterle. Experimental Studies of Bose–Einstein Condensation. *Physics Today*, 52(12):30–35, 12 1999. ISSN 0031-9228. doi: 10.1063/1.882898. URL https://doi.org/10.1063/1.882898.

[20] M. Saffman, T. G. Walker, and K. Mølmer. Quantum information with Rydberg atoms. *Rev. Mod. Phys.*, 82:2313–2363, Aug 2010. doi: 10.1103/RevModPhys.82.2313. URL https://link.aps.org/doi/10.1103/RevModPhys.82.2313.

[21] C. S. Adams, J. D. Pritchard, and J. P. Shaffer. Rydberg atom quantum technologies. *Journal of Physics B: Atomic, Molecular and Optical Physics*, 53(1):012002, 2020. doi: 10.1088/1361-6455/ab52ef. URL https://doi.org/10.1088/1361-6455/ab52ef.

[22] Michael Fleischhauer, Atac Imamoglu, and Jonathan P. Marangos. Electromagnetically induced transparency: Optics in coherent media. *Rev. Mod. Phys.*, 77:633–673, Jul 2005. doi: 10.1103/RevModPhys.77.633. URL https://link.aps.org/doi/10.1103/RevModPhys.77.633.

[23] M. Fleischhauer and M. D. Lukin. Dark-State Polaritons in Electromagnetically Induced Transparency. *Phys. Rev. Lett.*, 84:5094–5097, May 2000. doi: 10.1103/PhysRevLett.84.5094. URL https://link.aps.org/doi/10.1103/PhysRevLett.84.5094.

[24] M. D. Lukin, M. Fleischhauer, R. Cote, L. M. Duan, D. Jaksch, J. I. Cirac, and P. Zoller. Dipole Blockade and Quantum Information Processing in Mesoscopic Atomic Ensembles. *Phys. Rev. Lett.*, 87:037901, Jun 2001. doi: 10.1103/PhysRevLett.87.037901. URL https://link.aps.org/doi/10.1103/PhysRevLett.87.037901.

[25] Thomas F. Gallagher. *Rydberg Atoms*. Cambridge Monographs on Atomic, Molecular and Chemical Physics. Cambridge University Press, 1994.

[26] Daniel Comparat and Pierre Pillet. Dipole blockade in a cold Rydberg atomic sample. *J. Opt. Soc. Am. B*, 27(6):A208–A232, Jun 2010. doi: 10.1364/JOSAB.27.00A208. URL https://opg.optica.org/josab/abstract.cfm?URI=josab-27-6-A208.

[27] E. Urban, T. A. Johnson, T. Henage, L. Isenhower, D. D. Yavuz, T. G. Walker, and M. Saffman. Observation of Rydberg blockade between two atoms. *Nature Physics*, 5:110–114, 2009. doi: 10.1038/nphys1178. URL https://doi.org/10.1038/nphys1178.

[28] A. Gaëtan, Y. Miroshnychenko, T. Wilk, A. Chotia, M. Viteau, D. Comparat, P. Pillet, A. Browaeys, and P. Grangier. Observation of collective excitation of two individual atoms in the Rydberg blockade regime. *Nature Physics*, 5: 115–118, 2009. doi: 10.1038/nphys1183. URL `https://doi.org/10.1038/nphys1183`.

[29] L. Béguin, A. Vernier, R. Chicireanu, T. Lahaye, and A. Browaeys. Direct Measurement of the van der Waals Interaction between Two Rydberg Atoms. *Phys. Rev. Lett.*, 110:263201, Jun 2013. doi: 10.1103/PhysRevLett.110.263201. URL `https://link.aps.org/doi/10.1103/PhysRevLett.110.263201`.

[30] Y. O. Dudin and A. Kuzmich. Strongly interacting rydberg excitations of a cold atomic gas. *Science*, 336(6083):887–889, 2012. doi: 10.1126/science.1217901. URL `https://doi.org/10.1126/science.1217901`.

[31] A. K. Mohapatra, T. R. Jackson, and C. S. Adams. Coherent Optical Detection of Highly Excited Rydberg States Using Electromagnetically Induced Transparency. *Phys. Rev. Lett.*, 98:113003, Mar 2007. doi: 10.1103/PhysRevLett.98.113003. URL `https://link.aps.org/doi/10.1103/PhysRevLett.98.113003`.

[32] O. Firstenberg, C. S. Adams, and S. Hofferberth. Nonlinear quantum optics mediated by Rydberg interactions. *Journal of Physics B: Atomic, Molecular and Optical Physics*, 49(15):152003, 2016. doi: 10.1088/0953-4075/49/15/152003. URL `https://doi.org/10.1088/0953-4075/49/15/152003`.

[33] Alexey V. Gorshkov, Johannes Otterbach, Michael Fleischhauer, Thomas Pohl, and Mikhail D. Lukin. Photon-Photon Interactions via Rydberg Blockade. *Phys. Rev. Lett.*, 107:133602, Sep 2011. doi: 10.1103/PhysRevLett.107.133602. URL `https://link.aps.org/doi/10.1103/PhysRevLett.107.133602`.

[34] Thibault Peyronel, Ofer Firstenberg, Qi-Yu Liang, Sebastian Hofferberth, Alexey V. Gorshkov, Thomas Pohl, Mikhail D. Lukin, and Vladan Vuletić. Quantum nonlinear optics with single photons enabled by strongly interacting atoms. *Nature*, 488:57–60, 2012. doi: 10.1038/nature11361. URL `https://doi.org/10.1038/nature11361`.

[35] Michael A. Nielsen and Isaac L. Chuang. *Quantum Computation and Quantum Information: 10th Anniversary Edition*. Cambridge University Press, 2010.

[36] John Preskill. Quantum Computing in the NISQ era and beyond. *Quantum*, 2:79, August 2018. ISSN 2521-327X. doi: 10.22331/q-2018-08-06-79. URL `https://doi.org/10.22331/q-2018-08-06-79`.

[37] Benjamin P. Lanyon, Marco Barbieri, Marcelo P. Almeida, Thomas Jennewein, Timothy C. Ralph, Kevin J. Resch, Geoff J. Pryde, Jeremy L. O'Brien, Alexei Gilchrist, and Andrew G. White. Simplifying quantum logic using higher-dimensional Hilbert spaces. *Nature Physics*, 5:134–140, 2009. doi: 10.1038/nphys1150. URL `https://doi.org/10.1038/nphys1150`.

[38] Manuel Erhard, Mario Krenn, and Anton Zeilinger. Advances in high-dimensional quantum entanglement. *Nature Reviews Physics*, 2:365–381, 2020. doi: 10.1038/s42254-020-0193-5. URL `https://doi.org/10.1038/s42254-020-0193-5`.

[39] H. J. Kimble. The quantum internet. *Nature*, 453:1023–1030, 2008. doi: 10.1038/nature07127. URL `https://doi.org/10.1038/nature07127`.

[40] Andreas Reiserer and Gerhard Rempe. Cavity-based quantum networks with single atoms and optical photons. *Rev. Mod. Phys.*, 87:1379–1418, Dec 2015. doi: 10.1103/RevModPhys.87.1379. URL `https://link.aps.org/doi/10.1103/RevModPhys.87.1379`.

[41] Iris Cong, Harry Levine, Alexander Keesling, Dolev Bluvstein, Sheng-Tao Wang, and Mikhail D. Lukin. Hardware-Efficient, Fault-Tolerant Quantum Computation with Rydberg Atoms. *Phys. Rev. X*, 12:021049, Jun 2022. doi: 10.1103/PhysRevX.12.021049. URL `https://link.aps.org/doi/10.1103/PhysRevX.12.021049`.

[42] H. Gorniaczyk, C. Tresp, J. Schmidt, H. Fedder, and S. Hofferberth. Single-Photon Transistor Mediated by Interstate Rydberg Interactions. *Phys. Rev. Lett.*, 113:053601, Jul 2014. doi: 10.1103/PhysRevLett.113.053601. URL `https://link.aps.org/doi/10.1103/PhysRevLett.113.053601`.

[43] Daniel Tiarks, Steffen Schmidt-Eberle, Thomas Stolz, Gerhard Rempe, and Stephan Dürr. A photon–photon quantum gate based on Rydberg interactions. *Nature Physics*, 15:124–126, 2019. doi: 10.1038/s41567-018-0313-7. URL `https://doi.org/10.1038/s41567-018-0313-7`.

[44] Asmae Benhemou, Jiannis K. Pachos, and Dan E. Browne. Non-Abelian statistics with mixed-boundary punctures on the toric code. *Phys. Rev. A*, 105:042417, Apr 2022. doi: 10.1103/PhysRevA.105.042417. URL `https://link.aps.org/doi/10.1103/PhysRevA.105.042417`.

[45] Nicolas Gisin and Rob Thew. Quantum communication. *Nature Photonics*, 1:165–171, 2007. doi: 10.1038/nphoton.2007.22. URL `https://doi.org/10.1038/nphoton.2007.22`.

[46] Jeremy L. O'Brien. Optical Quantum Computing. *Science*, 318(5856):1567–1570, 2007. doi: 10.1126/science.1142892. URL `https://www.science.org/doi/abs/10.1126/science.1142892`.

[47] D. E. Chang, V. Vuletić, and M. D. Lukin. Quantum nonlinear optics — photon by photon. *Nature Photonics*, 8:685–694, 2014. doi: 10.1038/nphoton.2014.192. URL `https://doi.org/10.1038/nphoton.2014.192`.

[48] J. D. Pritchard, D. Maxwell, A. Gauguet, K. J. Weatherill, M. P. A. Jones, and C. S. Adams. Cooperative Atom-Light Interaction in a Blockaded Rydberg Ensemble. *Phys. Rev. Lett.*, 105:193603, Nov 2010. doi: 10.1103/PhysRevLett.105.193603. URL `https://link.aps.org/doi/10.1103/PhysRevLett.105.193603`.

[49] C. Murray and T. Pohl. Quantum and Nonlinear Optics in Strongly Interacting Atomic Ensembles. volume 65 of *Advances In Atomic, Molecular, and Optical Physics*, pages 321–372. Academic Press, 2016. doi: https://doi.org/10.1016/bs.aamop.2016.04.005. URL `https://www.sciencedirect.com/science/article/pii/S1049250X1630009X`.

[50] L. Li, Y. O. Dudin, and A. Kuzmich. Entanglement between light and an optical atomic excitation. *Nature*, 498:466–469, 2013. doi: 10.1038/nature12227. URL `https://doi.org/10.1038/nature12227`.

[51] Simon Baur, Daniel Tiarks, Gerhard Rempe, and Stephan Dürr. Single-Photon Switch Based on Rydberg Blockade. *Phys. Rev. Lett.*, 112:073901, Feb 2014. doi: 10.1103/PhysRevLett.112.073901. URL `https://link.aps.org/doi/10.1103/PhysRevLett.112.073901`.

[52] Andreas Reiserer and Gerhard Rempe. Cavity-based quantum networks with single atoms and optical photons. *Rev. Mod. Phys.*, 87:1379–1418, Dec 2015. doi: 10.1103/RevModPhys.87.1379. URL `https://link.aps.org/doi/10.1103/RevModPhys.87.1379`.

[53] D. Barredo, V. Lienhard, S. de Léséleuc, T. Lahaye, and A. Browaeys. Synthetic three-dimensional atomic structures assembled atom by atom. *Nature*, 561(7721):79–82, September 2018. doi: 10.1038/s41586-018-0450-2.

[54] Daniel A. Steck. Rubidium 87 D Line Data. `http://steck.us/alkalidata`, 2024. Revision 2.3.3, 28 May 2024.

[55] Harold J. Metcalf and Peter van der Straten. *Laser Cooling and Trapping*. Graduate Texts in Contemporary Physics. Springer, New York, NY, 1 edition, 1999. ISBN 978-0-387-98747-7. doi: 10.1007/978-1-4612-1470-0. URL https://doi.org/10.1007/978-1-4612-1470-0.

[56] Jun Ye, Steve Swartz, Peter Jungner, and John L. Hall. Hyperfine structure and absolute frequency of the 87Rb 5P3/2 state. *Opt. Lett.*, 21(16):1280–1282, Aug 1996. doi: 10.1364/OL.21.001280. URL https://opg.optica.org/ol/abstract.cfm?URI=ol-21-16-1280.

[57] C. Monroe, W. Swann, H. Robinson, and C. Wieman. Very cold trapped atoms in a vapor cell. *Phys. Rev. Lett.*, 65:1571–1574, Sep 1990. doi: 10.1103/PhysRevLett.65.1571. URL https://link.aps.org/doi/10.1103/PhysRevLett.65.1571.

[58] C. G. Townsend, N. H. Edwards, C. J. Cooper, K. P. Zetie, C. J. Foot, A. M. Steane, P. Szriftgiser, H. Perrin, and J. Dalibard. Phase-space density in the magneto-optical trap. *Phys. Rev. A*, 52:1423–1440, Aug 1995. doi: 10.1103/PhysRevA.52.1423. URL https://link.aps.org/doi/10.1103/PhysRevA.52.1423.

[59] Alan L. Migdall, John V. Prodan, William D. Phillips, Thomas H. Bergeman, and Harold J. Metcalf. First Observation of Magnetically Trapped Neutral Atoms. *Phys. Rev. Lett.*, 54:2596–2599, Jun 1985. doi: 10.1103/PhysRevLett.54.2596. URL https://link.aps.org/doi/10.1103/PhysRevLett.54.2596.

[60] L Allen and J H Eberly. *Optical resonance and two-level atoms*. John Wiley and Sons, Inc.,New York, 01 1975. URL https://www.osti.gov/biblio/7365050.

[61] Mark Fox. *Quantum Optics: An Introduction*. Oxford University Press, 04

2006. ISBN 9780198566724. doi: 10.1093/oso/9780198566724.003.0001. URL https://doi.org/10.1093/oso/9780198566724.003.0001.

[62] Göran Lindblad. On the Generators of Quantum Dynamical Semigroups. *Communications in Mathematical Physics*, 48:119–130, 1976. doi: 10.1007/BF01608499. URL https://doi.org/10.1007/BF01608499.

[63] Norman F. Ramsey. A Molecular Beam Resonance Method with Separated Oscillating Fields. *Phys. Rev.*, 78:695–699, Jun 1950. doi: 10.1103/PhysRev.78.695. URL https://link.aps.org/doi/10.1103/PhysRev.78.695.

[64] D. J. Wineland, J. J. Bollinger, W. M. Itano, and D. J. Heinzen. Squeezed atomic states and projection noise in spectroscopy. *Phys. Rev. A*, 50:67–88, Jul 1994. doi: 10.1103/PhysRevA.50.67. URL https://link.aps.org/doi/10.1103/PhysRevA.50.67.

[65] W. M. Itano, J. C. Bergquist, J. J. Bollinger, J. M. Gilligan, D. J. Heinzen, F. L. Moore, M. G. Raizen, and D. J. Wineland. Quantum projection noise: Population fluctuations in two-level systems. *Phys. Rev. A*, 47:3554–3570, May 1993. doi: 10.1103/PhysRevA.47.3554. URL https://link.aps.org/doi/10.1103/PhysRevA.47.3554.

[66] Jean Dalibard, Yvan Castin, and Klaus Mølmer. Wave-function approach to dissipative processes in quantum optics. *Phys. Rev. Lett.*, 68:580–583, Feb 1992. doi: 10.1103/PhysRevLett.68.580. URL https://link.aps.org/doi/10.1103/PhysRevLett.68.580.

[67] I. I. Beterov, I. I. Ryabtsev, D. B. Tretyakov, and V. M. Entin. Quasiclassical calculations of blackbody-radiation-induced depopulation rates and effective lifetimes of Rydberg nS, nP, and nD alkali-metal atoms with $n \leq 80$. *Phys. Rev. A*, 79:052504, May 2009. doi: 10.1103/PhysRevA.79.052504. URL https://link.aps.org/doi/10.1103/PhysRevA.79.052504.

[68] Heinz-Peter Breuer and Francesco Petruccione. *The theory of open quantum systems*. OUP Oxford, 2002.

[69] M. B. Plenio and P. L. Knight. The quantum-jump approach to dissipative dynamics in quantum optics. *Rev. Mod. Phys.*, 70:101–144, Jan 1998. doi: 10.1103/RevModPhys.70.101. URL `https://link.aps.org/doi/10.1103/RevModPhys.70.101`.

[70] S. E. Harris, J. E. Field, and A. Imamoğlu. Nonlinear optical processes using electromagnetically induced transparency. *Phys. Rev. Lett.*, 64:1107–1110, Mar 1990. doi: 10.1103/PhysRevLett.64.1107. URL `https://link.aps.org/doi/10.1103/PhysRevLett.64.1107`.

[71] K.-J. Boller, A. Imamoğlu, and S. E. Harris. Observation of electromagnetically induced transparency. *Phys. Rev. Lett.*, 66:2593–2596, May 1991. doi: 10.1103/PhysRevLett.66.2593. URL `https://link.aps.org/doi/10.1103/PhysRevLett.66.2593`.

[72] Julio Gea-Banacloche, Yong-qing Li, Shao-zheng Jin, and Min Xiao. Electromagnetically induced transparency in ladder-type inhomogeneously broadened media: Theory and experiment. *Phys. Rev. A*, 51:576–584, Jan 1995. doi: 10.1103/PhysRevA.51.576. URL `https://link.aps.org/doi/10.1103/PhysRevA.51.576`.

[73] S. E. Harris and Lene Vestergaard Hau. Nonlinear Optics at Low Light Levels. *Phys. Rev. Lett.*, 82:4611–4614, Jun 1999. doi: 10.1103/PhysRevLett.82.4611. URL `https://link.aps.org/doi/10.1103/PhysRevLett.82.4611`.

[74] Michael M. Kash, Vladimir A. Sautenkov, Alexander S. Zibrov, L. Hollberg, George R. Welch, Mikhail D. Lukin, Yuri Rostovtsev, Edward S. Fry, and Marlan O. Scully. Ultraslow Group Velocity and Enhanced Nonlinear Optical Effects in a Coherently Driven Hot Atomic Gas. *Phys. Rev. Lett.*, 82:5229–

5232, Jun 1999. doi: 10.1103/PhysRevLett.82.5229. URL `https://link.aps.org/doi/10.1103/PhysRevLett.82.5229`.

[75] D. Budker, D. F. Kimball, S. M. Rochester, and V. V. Yashchuk. Nonlinear Magneto-optics and Reduced Group Velocity of Light in Atomic Vapor with Slow Ground State Relaxation. *Phys. Rev. Lett.*, 83:1767–1770, Aug 1999. doi: 10.1103/PhysRevLett.83.1767. URL `https://link.aps.org/doi/10.1103/PhysRevLett.83.1767`.

[76] D. Maxwell, D. J. Szwer, D. Paredes-Barato, H. Busche, J. D. Pritchard, A. Gauguet, K. J. Weatherill, M. P. A. Jones, and C. S. Adams. Storage and Control of Optical Photons Using Rydberg Polaritons. *Phys. Rev. Lett.*, 110:103001, Mar 2013. doi: 10.1103/PhysRevLett.110.103001. URL `https://link.aps.org/doi/10.1103/PhysRevLett.110.103001`.

[77] Ofer Firstenberg, Thibault Peyronel, Qi-Yu Liang, Alexey V. Gorshkov, Mikhail D. Lukin, and Vladan Vuletić. Attractive photons in a quantum nonlinear medium. *Nature*, 502:71–75, 2013. doi: 10.1038/nature12512. URL `https://doi.org/10.1038/nature12512`.

[78] Nikola Šibalić, James D. Pritchard, Charles S. Adams, and Kevin J. Weatherill. ARC: An open-source library for calculating properties of alkali Rydberg atoms. *Computer Physics Communications*, 220:319–331, 2017. ISSN 0010-4655. doi: 10.1016/j.cpc.2017.06.015. URL `https://doi.org/10.1016/j.cpc.2017.06.015`.

[79] Kilian Singer, Jovica Stanojevic, Matthias Weidemüller, and Robin Côté. Long-range interactions between alkali Rydberg atom pairs correlated to the ns–ns, np–np and nd–nd asymptotes. *Journal of Physics B: Atomic, Molecular and Optical Physics*, 38(2):S295, jan 2005. doi: 10.1088/0953-4075/38/2/021. URL `https://dx.doi.org/10.1088/0953-4075/38/2/021`.

[80] Wenhui Li, I. Mourachko, M. W. Noel, and T. F. Gallagher. Millimeter-wave spectroscopy of cold Rb Rydberg atoms in a magneto-optical trap: Quantum defects of the ns, np, and nd series. *Phys. Rev. A*, 67:052502, May 2003. doi: 10.1103/PhysRevA.67.052502. URL `https://link.aps.org/doi/10.1103/PhysRevA.67.052502`.

[81] Thad G. Walker and M. Saffman. Consequences of Zeeman degeneracy for the van der Waals blockade between Rydberg atoms. *Phys. Rev. A*, 77: 032723, Mar 2008. doi: 10.1103/PhysRevA.77.032723. URL `https://link.aps.org/doi/10.1103/PhysRevA.77.032723`.

[82] M. S. O'Sullivan and B. P. Stoicheff. Scalar polarizabilities and avoided crossings of high Rydberg states in Rb. *Phys. Rev. A*, 31:2718–2720, Apr 1985. doi: 10.1103/PhysRevA.31.2718. URL `https://link.aps.org/doi/10.1103/PhysRevA.31.2718`.

[83] I. I. Ryabtsev, D. B. Tretyakov, I. I. Beterov, and V. M. Entin. Observation of the Stark-Tuned Förster Resonance between Two Rydberg Atoms. *Phys. Rev. Lett.*, 104:073003, Feb 2010. doi: 10.1103/PhysRevLett.104.073003. URL `https://link.aps.org/doi/10.1103/PhysRevLett.104.073003`.

[84] J. Nipper, J. B. Balewski, A. T. Krupp, B. Butscher, R. Löw, and T. Pfau. Highly Resolved Measurements of Stark-Tuned Förster Resonances between Rydberg Atoms. *Phys. Rev. Lett.*, 108:113001, Mar 2012. doi: 10.1103/PhysRevLett.108.113001. URL `https://link.aps.org/doi/10.1103/PhysRevLett.108.113001`.

[85] D. Tong, S. M. Farooqi, J. Stanojevic, S. Krishnan, Y. P. Zhang, R. Côté, E. E. Eyler, and P. L. Gould. Local Blockade of Rydberg Excitation in an Ultracold Gas. *Phys. Rev. Lett.*, 93:063001, Aug 2004. doi: 10.1103/PhysRevLett.93.063001. URL `https://link.aps.org/doi/10.1103/PhysRevLett.93.063001`.

[86] Sylvain Ravets, Henning Labuhn, Daniel Barredo, Lucas Béguin, Thierry Lahaye, and Antoine Browaeys. Coherent dipole–dipole coupling between two single Rydberg atoms at an electrically-tuned Förster resonance. *Nature Physics*, 10:914–917, 2014. doi: 10.1038/nphys3119. URL `https://doi.org/10.1038/nphys3119`.

[87] W. R. Anderson, J. R. Veale, and T. F. Gallagher. Resonant Dipole-Dipole Energy Transfer in a Nearly Frozen Rydberg Gas. *Phys. Rev. Lett.*, 80:249–252, Jan 1998. doi: 10.1103/PhysRevLett.80.249. URL `https://link.aps.org/doi/10.1103/PhysRevLett.80.249`.

[88] Sylvain de Léséleuc, Daniel Barredo, Vincent Lienhard, Antoine Browaeys, and Thierry Lahaye. Optical Control of the Resonant Dipole-Dipole Interaction between Rydberg Atoms. *Phys. Rev. Lett.*, 119:053202, Aug 2017. doi: 10.1103/PhysRevLett.119.053202. URL `https://link.aps.org/doi/10.1103/PhysRevLett.119.053202`.

[89] Rolf Heidemann, Ulrich Krohn, Vera Bendkowsky, Björn Butscher, Robert Löw, Luis Santos, and Tilman Pfau. Evidence for Coherent Collective Rydberg Excitation in the Strong Blockade Regime. *Phys. Rev. Lett.*, 99:163601, Oct 2007. doi: 10.1103/PhysRevLett.99.163601. URL `https://link.aps.org/doi/10.1103/PhysRevLett.99.163601`.

[90] T. M. Weber, M. Höning, T. Niederprüm, T. Manthey, O. Thomas, V. Guarrera, M. Fleischhauer, G. Barontini, and H. Ott. Mesoscopic Rydberg-blockaded ensembles in the superatom regime and beyond. *Nature Physics*, 11:157–161, 2015. doi: 10.1038/nphys3214.

[91] L. Isenhower, E. Urban, X. L. Zhang, A. T. Gill, T. Henage, T. A. Johnson, T. G. Walker, and M. Saffman. Demonstration of a Neutral Atom Controlled-NOT Quantum Gate. *Phys. Rev. Lett.*, 104:010503, Jan 2010. doi: 10.1103/PhysRevLett.104.010503. URL `https://link.aps.org/doi/10.1103/PhysRevLett.104.010503`.

[92] D. Jaksch, J. I. Cirac, P. Zoller, S. L. Rolston, R. Côté, and M. D. Lukin. Fast Quantum Gates for Neutral Atoms. *Phys. Rev. Lett.*, 85:2208–2211, Sep 2000. doi: 10.1103/PhysRevLett.85.2208. URL `https://link.aps.org/doi/10.1103/PhysRevLett.85.2208`.

[93] D. Paredes-Barato and C. S. Adams. All-Optical Quantum Information Processing Using Rydberg Gates. *Phys. Rev. Lett.*, 112:040501, Jan 2014. doi: 10.1103/PhysRevLett.112.040501. URL `https://link.aps.org/doi/10.1103/PhysRevLett.112.040501`.

[94] T. M. Graham, M. Kwon, B. Grinkemeyer, Z. Marra, X. Jiang, M. T. Lichtman, Y. Sun, M. Ebert, and M. Saffman. Rydberg-Mediated Entanglement in a Two-Dimensional Neutral Atom Qubit Array. *Phys. Rev. Lett.*, 123:230501, Dec 2019. doi: 10.1103/PhysRevLett.123.230501. URL `https://link.aps.org/doi/10.1103/PhysRevLett.123.230501`.

[95] Marlan O. Scully and M. Suhail Zubairy. *Quantum Optics*. Cambridge University Press, 1997.

[96] Claude N. Cohen-Tannoudji. Nobel Lecture: Manipulating atoms with photons. *Rev. Mod. Phys.*, 70:707–719, Jul 1998. doi: 10.1103/RevModPhys.70.707. URL `https://link.aps.org/doi/10.1103/RevModPhys.70.707`.

[97] P. J. Ungar, D. S. Weiss, E. Riis, and Steven Chu. Optical molasses and multilevel atoms: theory. *J. Opt. Soc. Am. B*, 6(11):2058–2071, Nov 1989. doi: 10.1364/JOSAB.6.002058. URL `https://opg.optica.org/josab/abstract.cfm?URI=josab-6-11-2058`.

[98] Mark Kasevich and Steven Chu. Laser cooling below a photon recoil with three-level atoms. *Phys. Rev. Lett.*, 69:1741–1744, Sep 1992. doi: 10.1103/PhysRevLett.69.1741. URL `https://link.aps.org/doi/10.1103/PhysRevLett.69.1741`.

[99] S. E. Hamann, D. L. Haycock, G. Klose, P. H. Pax, I. H. Deutsch, and P. S. Jessen. Resolved-Sideband Raman Cooling to the Ground State of an Optical Lattice. *Phys. Rev. Lett.*, 80:4149–4152, May 1998. doi: 10.1103/PhysRevLett.80.4149. URL `https://link.aps.org/doi/10.1103/PhysRevLett.80.4149`.

[100] Rudolf Grimm and Matthias Weidemüller. Optical Dipole Traps for Neutral Atoms. *Advances in Atomic Molecular and Optical Physics*, 42:95–170, January 2000. doi: 10.1016/S1049-250X(08)60186-X.

[101] J. D. Miller, R. A. Cline, and D. J. Heinzen. Far-off-resonance optical trapping of atoms. *Phys. Rev. A*, 47:R4567–R4570, Jun 1993. doi: 10.1103/PhysRevA.47.R4567. URL `https://link.aps.org/doi/10.1103/PhysRevA.47.R4567`.

[102] J. Mitroy, M. S. Safronova, and Charles W. Clark. Theory and applications of atomic and ionic polarizabilities. *Journal of Physics B: Atomic, Molecular and Optical Physics*, 43(20):202001, 2010. doi: 10.1088/0953-4075/43/20/202001. URL `https://doi.org/10.1088/0953-4075/43/20/202001`.

[103] Roy J. Glauber. The Quantum Theory of Optical Coherence. *Phys. Rev.*, 130:2529–2539, Jun 1963. doi: 10.1103/PhysRev.130.2529. URL `https://link.aps.org/doi/10.1103/PhysRev.130.2529`.

[104] H. J. Kimble, M. Dagenais, and L. Mandel. Photon Antibunching in Resonance Fluorescence. *Phys. Rev. Lett.*, 39:691–695, Sep 1977. doi: 10.1103/PhysRevLett.39.691. URL `https://link.aps.org/doi/10.1103/PhysRevLett.39.691`.

[105] R. Short and L. Mandel. Observation of Sub-Poissonian Photon Statistics. *Phys. Rev. Lett.*, 51:384–387, Aug 1983. doi: 10.1103/PhysRevLett.51.384. URL `https://link.aps.org/doi/10.1103/PhysRevLett.51.384`.

[106] R. Hanbury Brown and R. Q. Twiss. Correlation between Photons in Two Coherent Beams of Light. *Nature*, 177:27–29, 1956. doi: 10.1038/177027a0. URL https://doi.org/10.1038/177027a0.

[107] R. Hanbury Brown and R. Q. Twiss. A Test of a New Type of Stellar Interferometer on Sirius. *Nature*, 178:1046–1048, 1956. doi: 10.1038/1781046a0. URL https://doi.org/10.1038/1781046a0.

[108] Wolfgang Becker. *Advanced Time-Correlated Single Photon Counting Techniques*. Springer, 2005. ISBN 978-3-540-22308-0. doi: https://doi.org/10.1007/3-540-28882-1.

[109] Daniel Tiarks, Simon Baur, Katharina Schneider, Stephan Dürr, and Gerhard Rempe. Single-Photon Transistor Using a Förster Resonance. *Phys. Rev. Lett.*, 113:053602, Jul 2014. doi: 10.1103/PhysRevLett.113.053602. URL https://link.aps.org/doi/10.1103/PhysRevLett.113.053602.

[110] H. Busche, S. W. Ball, and P. Huillery. A high repetition rate experimental setup for quantum non-linear optics with cold Rydberg atoms. *European Physical Journal Special Topics*, 225(13-14):2839–2861, 2016. doi: 10.1140/epjst/e2015-50338-3. URL https://doi.org/10.1140/epjst/e2015-50338-3.

[111] Hannes Busche, Paul Huillery, Simon W. Ball, Teodora Ilieva, Matthew P. A. Jones, and Charles S. Adams. Contactless nonlinear optics mediated by long-range Rydberg interactions. *Nature Physics*, 13:655–658, 2017. doi: 10.1038/nphys4058. URL https://doi.org/10.1038/nphys4058.

[112] Hannes Busche. *Contactless quantum non-linear optics with cold Rydberg atoms*. PhD thesis, Durham University, 2017. Available at http://etheses.dur.ac.uk/12238/.

[113] Simon William Ball. *A coherent microwave interface for manipulation of single optical photons*. Phd thesis, Durham University, 2017. URL `http://etheses.dur.ac.uk/12385/`. Available at Durham E-Theses Online.

[114] J. H. Shirley. Modulation transfer processes in optical heterodyne saturation spectroscopy. *Optics Letters*, 7(11):537–539, 1982. doi: 10.1364/OL.7.000537.

[115] D. J. McCarron, S. A. King, and S. L. Cornish. Modulation transfer spectroscopy in atomic rubidium. *Measurement Science and Technology*, 19 (10):105601, 2008. doi: 10.1088/0957-0233/19/10/105601. URL `https://doi.org/10.1088/0957-0233/19/10/105601`.

[116] Chloe So, Nicholas L. R. Spong, Charles Möhl, Yuechun Jiao, Teodora Ilieva, and Charles S. Adams. Zeeman-tunable modulation transfer spectroscopy. *Opt. Lett.*, 44(21):5374–5377, Nov 2019. doi: 10.1364/OL.44.005374. URL `https://opg.optica.org/ol/abstract.cfm?URI=ol-44-21-5374`.

[117] R. W. P. Drever, J. L. Hall, F. V. Kowalski, J. Hough, G. M. Ford, A. J. Munley, and H. Ward. Laser phase and frequency stabilization using an optical resonator. *Applied Physics B*, 31:97–105, 1983. doi: 10.1007/BF00702605.

[118] Remy Legaie, Craig J. Picken, and Jonathan D. Pritchard. Sub-kilohertz excitation lasers for quantum information processing with Rydberg atoms. *J. Opt. Soc. Am. B*, 35(4):892–898, Apr 2018. doi: 10.1364/JOSAB.35.000892. URL `https://opg.optica.org/josab/abstract.cfm?URI=josab-35-4-892`.

[119] K. Dieckmann, R. J. C. Spreeuw, M. Weidemüller, and J. T. M. Walraven. Two-dimensional magneto-optical trap as a source of slow atoms. *Phys. Rev. A*, 58:3891–3895, Nov 1998. doi: 10.1103/PhysRevA.58.3891. URL `https://link.aps.org/doi/10.1103/PhysRevA.58.3891`.

[120] Jan Schoser, Alois Batär, Ralf Löw, Viktor Schweikhard, Axel Grabowski, and Martin Weidemüller. Intense source of cold rubidium atoms from a two-

dimensional magneto-optical trap. *Physical Review A*, 66(2):023410, 2002. doi: 10.1103/PhysRevA.66.023410.

[121] Nicholas Leonard Robert Spong. *Coherent Manipulation of Rydberg Polaritons*. Phd thesis, Durham University, 2022. Available at Durham E-Theses Online: `http://etheses.dur.ac.uk/14318/`.

[122] Timothy Peter Wiles. *Dynamics of bright solitary matter-waves*. Phd thesis, Durham University, 2013. Available at Durham E-Theses Online: `http://etheses.dur.ac.uk/7382/`.

[123] Yuchen Wang, Zixuan Hu, Barry C. Sanders, and Sabre Kais. Qudits and High-Dimensional Quantum Computing. *Frontiers in Physics*, Volume 8 - 2020, 2020. ISSN 2296-424X. doi: 10.3389/fphy.2020.589504. URL `https://www.frontiersin.org/journals/physics/articles/10.3389/fphy.2020.589504`.

[124] Jesper Mackeprang, Daniyal Bhatti, and Stefanie Barz. Non-adaptive measurement-based quantum computation on IBM Q. *Scientific Reports*, 13:15428, 2023. doi: 10.1038/s41598-023-41025-4. URL `https://doi.org/10.1038/s41598-023-41025-4`.

[125] Pranav Gokhale, Jonathan M. Baker, Casey Duckering, Natalie C. Brown, Kenneth R. Brown, and Frederic T. Chong. Asymptotic improvements to quantum circuits via qutrits. In *Proceedings of the 46th International Symposium on Computer Architecture*, ISCA '19, page 554–566, New York, NY, USA, 2019. Association for Computing Machinery. ISBN 9781450366694. doi: 10.1145/3307650.3322253. URL `https://doi.org/10.1145/3307650.3322253`.

[126] B. P. Lanyon, T. J. Weinhold, N. K. Langford, J. L. O'Brien, K. J. Resch, A. Gilchrist, and A. G. White. Manipulating Biphotonic Qutrits. *Physical Review Letters*, 100(6):060504, 2008.

[127] Yi-Han Luo, Han-Sen Zhong, Manuel Erhard, Xi-Lin Wang, Li-Chao Peng, Mario Krenn, Xiao Jiang, Li Li, Nai-Le Liu, Chao-Yang Lu, Anton Zeilinger, and Jian-Wei Pan. Quantum Teleportation in High Dimensions. *Phys. Rev. Lett.*, 123:070505, Aug 2019. doi: 10.1103/PhysRevLett.123.070505. URL https://link.aps.org/doi/10.1103/PhysRevLett.123.070505.

[128] Daniel Collins, Nicolas Gisin, Noah Linden, Serge Massar, and Sandu Popescu. Bell Inequalities for Arbitrarily High-Dimensional Systems. *Phys. Rev. Lett.*, 88:040404, Jan 2002. doi: 10.1103/PhysRevLett.88.040404. URL https://link.aps.org/doi/10.1103/PhysRevLett.88.040404.

[129] Max Z. Festenstein. An Intuitive Visualisation Method for Arbitrary Qutrit (Three Level) States, 2023. URL https://arxiv.org/abs/2304.01741.

[130] M. S. Blok, V. V. Ramasesh, T. Schuster, K. O'Brien, J. M. Kreikebaum, D. Dahlen, A. Morvan, B. Yoshida, N. Y. Yao, and I. Siddiqi. Quantum Information Scrambling on a Superconducting Qutrit Processor. *Phys. Rev. X*, 11:021010, Apr 2021. doi: 10.1103/PhysRevX.11.021010. URL https://link.aps.org/doi/10.1103/PhysRevX.11.021010.

[131] Markus Rambach, Mahdi Qaryan, Michael Kewming, Christopher Ferrie, Andrew G. White, and Jacquiline Romero. Robust and Efficient High-Dimensional Quantum State Tomography. *Phys. Rev. Lett.*, 126:100402, Mar 2021. doi: 10.1103/PhysRevLett.126.100402. URL https://link.aps.org/doi/10.1103/PhysRevLett.126.100402.

[132] K. J. Weatherill, J. D. Pritchard, P. F. Griffin, U. Dammalapati, C. S. Adams, and E. Riis. A versatile and reliably reusable ultrahigh vacuum viewport. *Review of Scientific Instruments*, 80(2):026105, 2009. doi: 10.1063/1.3075547.

[133] Kevin J. Weatherill. *A CO_2 laser lattice experiment for cold atoms.* Phd thesis, Durham University, 2007. Available at Durham E-Theses Online: http://etheses.dur.ac.uk/2310/.

[134] John F. O'Hanlon. *A User's Guide to Vacuum Technology*. Wiley, Hoboken, NJ, 3rd edition, 2003.

[135] B. P. Anderson and M. A. Kasevich. Loading a vapor-cell magneto-optic trap using light-induced atom desorption. *Phys. Rev. A*, 63:023404, Jan 2001. doi: 10.1103/PhysRevA.63.023404. URL https://link.aps.org/doi/10.1103/PhysRevA.63.023404.

[136] T. Karaulanov, M. T. Graf, D. English, S. M. Rochester, Y. J. Rosen, K. Tsigutkin, D. Budker, E. B. Alexandrov, M. V. Balabas, D. F. Jackson Kimball, F. A. Narducci, S. Pustelny, and V. V. Yashchuk. Controlling atomic vapor density in paraffin-coated cells using light-induced atomic desorption. *Phys. Rev. A*, 79:012902, Jan 2009. doi: 10.1103/PhysRevA.79.012902. URL https://link.aps.org/doi/10.1103/PhysRevA.79.012902.

[137] Eliran Talker, Pankaj Arora, Roy Zektzer, Yoel Sebbag, Mark Dikopltsev, and Uriel Levy. Light-Induced Atomic Desorption in Microfabricated Vapor Cells for Demonstrating Quantum Optical Applications. *Phys. Rev. Appl.*, 15: L051001, May 2021. doi: 10.1103/PhysRevApplied.15.L051001. URL https://link.aps.org/doi/10.1103/PhysRevApplied.15.L051001.

[138] Naota Sekiguchi, Takumi Sato, Kiyoshi Ishikawa, and Atsushi Hatakeyama. Spectroscopic study of a diffusion-bonded sapphire cell for hot metal vapors. *Appl. Opt.*, 57(1):52–56, Jan 2018. doi: 10.1364/AO.57.000052. URL https://opg.optica.org/ao/abstract.cfm?URI=ao-57-1-52.

[139] American Scientific Glassblowers Society. Optical Transmission of Glass. https://asgs-glass.org/optical-transmission/, 2020.

[140] Danielle Boddy. *First observations of Rydberg blockade in a frozen gas of divalent atoms*. Phd thesis, Durham University, 2014. Available at Durham E-Theses Online: http://etheses.dur.ac.uk/10740/.

[141] James Keaveney, Armen Sargsyan, Ulrich Krohn, Julia Gontcharov, Ifan G. Hughes, David Sarkisyan, and Charles S. Adams. Optical transmission through a dipolar layer, 2011. URL `https://arxiv.org/abs/1109.3669`.

[142] Jingshan Han, Thibault Vogt, Christian Gross, Dieter Jaksch, Martin Kiffner, and Wenhui Li. Coherent Microwave-to-Optical Conversion via Six-Wave Mixing in Rydberg Atoms. *Phys. Rev. Lett.*, 120:093201, Mar 2018. doi: 10.1103/PhysRevLett.120.093201. URL `https://link.aps.org/doi/10.1103/PhysRevLett.120.093201`.

[143] I. I. Beterov, D. B. Tretyakov, V. M. Entin, E. A. Yakshina, I. I. Ryabtsev, C. MacCormick, and S. Bergamini. Deterministic single-atom excitation via adiabatic passage and Rydberg blockade. *Phys. Rev. A*, 84:023413, Aug 2011. doi: 10.1103/PhysRevA.84.023413. URL `https://link.aps.org/doi/10.1103/PhysRevA.84.023413`.

[144] C. K. Hong, Z. Y. Ou, and L. Mandel. Measurement of subpicosecond time intervals between two photons by interference. *Phys. Rev. Lett.*, 59:2044–2046, 1987. doi: 10.1103/PhysRevLett.59.2044.

Colophon

This thesis is based on a template developed by Matthew Townson and Andrew Reeves. It was typeset with LaTeX 2_ε. It was created using the *memoir* package, maintained by Lars Madsen, with the *madsen* chapter style. The font used is Latin Modern, derived from fonts designed by Donald E. Kunth.